Dissertation

submitted to the

Combined Faculties for Natural Sciences and for

Mathematics

of the Ruperto-Carola University of Heidelberg, Germany

for the degree of

Doctor of the Natural Sciences

put forward by

M.Sc. Sunny Saurabh

born in Purnea, India

Oral examination: 03.07.2019

Collision studies with internally cold ion beams and merged electron beams in a cryogenic storage ring

Referees:

Prof. Dr. Andreas Wolf

Priv.-Doz. Dr. Robert Moshammer

Abstract

Collision studies with internally cold ion beams and merged electron beams in a cryogenic storage ring

The electrostatic cryogenic storage ring (CSR) with wall temperature below 10 K and ultralow pressure, mimics the conditions of the interstellar medium. Infrared active molecular ions can radiatively relax towards their ro-vibrational ground state while being stored in the CSR. In this work, an electron-ion collision experiment is performed under these conditions and the conditions of electron-ion collisions in the merged beams are modelled. For this purpose, the electron beam trajectory is calculated in a magnetic field analysis program. The effect of the overlap geometry, drift tube potential, space charge variations and thermal energy spread of the electron beam have been studied individually. The collision energy distributions in the combination of such experimental conditions are provided. Based on these energy distributions and a narrow-peak cross section, the measured collision rate coefficient is simulated at several detuning energies. A correction method is developed to account for collision energy broadening from the full overlap geometry and drift tube potential.

With these tools, dissociative recombination (DR) of HeH^+ ions is investigated in the CSR and absolute DR rate coefficients are obtained for ro-vibrationally cold ions. The time dependence of the DR rate showed fast changes in the rate coefficient at increasing storage time. This could be explained from the radiative cooling model of the HeH^+ ion. In addition, merged beams with an electron deceleration drift tube have been successfully used and the results compared to the operation without employing the drift tubes.

Zusammenfassung

Kollisionsexperimente von rotations- und vibrationsgekühlten Ionenstrahlen mit überlagerten Elektronenstrahlen in einem kryogenen Speicherring

Der elektrostatische cryogenic storage ring (CSR) stellt mit Wandtemperaturen von unter 10 K und extrem niedrigen Restgasdichten eine vergleichbare Umgebung zum interstellaren Medium dar. Infrarot-aktive Moleküle sind innerhalb dieses Speicher-rings in der Lage, sich in Richtung ihres Vibrations- und Rotationsgrundzustands abzukühlen. Diese Thesis befasst sich mit Kollisionen zwischen Elektronen und molekularen Ionen sowie der Simulation der Kollisionsbedingungen zur Auswertung experimenteller Ergebnisse. Zu diesem Zweck werden Elekronenstrahltrajektorien in verwendeten magnetischen Feldern simuliert. Weiterhin werden Einflüsse der Überlappgeometrie, des Driftröhrenpotentials, von Raumladungseffekten und der thermischen Energieverteilung des Elektronenstrahls betrachtet, um eine Verteilungsfunktion für Kollisionsenergien zu extrahieren. Durch Falten dieser Verteilungsfunktion mit schmalbandigen Resonanzen im Wirkungsquerschnitt werden gemessene Ratenkoeffizienten reproduziert. Schließlich wird eine Methodik entwickelt, um Kollisionenergieverteilungen für gegebene Überlapplängen und Driftröhrenpotentiale zu korrigieren.

Die zuvor beschriebene Methodik wird dazu verwendet, absolute Ratenkoeffizienten für Dissoziative Rekombination (DR) von HeH^+ Ionen im Rotations- und Vibrationsgrundzustand zu analysieren. Zeitabhängige Untersuchungen zeigen schnelle Änderungen des DR Ratenkoeffizients mit fortschreitender Speicherzeit auf. Mithilfe eines Modells zur radiativen Kühlung von HeH^+ im Strahlungsfeld des CSR lässt sich diese Zeitabhängigkeit als Übergang zwischen Rotationszuständen erklären. Darüber hinaus werden Ergebnisse für Ratenkoeffizienten für Experimente mit und ohne Nutzung von Driftröhrenpotentialen, die zur Abbremsung des Elekronenstrahls in der Wechselwirkungszone verwendet werden, verglichen.

Contents

Contents

x

1 Introduction

Ion chemistry in the astrophysical plasma environments are driven by gas-phase atomic and molecular reactions [1, 2]. In such astrophysical plasma, e.g., the interstellar medium (ISM), planetary atmospheres, the early universe, etc., molecules undergo photon induced or collision induced reactions [3]. In the ISM the particle density is in the order of $10 - 1000$ cm^{-3} and temperature in the range of $10 - 100$ K. Numerous molecules from the molecular H$_2$ to polyatomic molecules and, e.g., C$_{60}$ have been discovered from their spectroscopic signatures despite the extreme conditions [4, 5, 6]. The observed present molecular ion abundances in the ISM are an outcome of various formation and destruction processes within a very active chemical reaction network [1].

Low-energy collisions between molecular ions and electrons are one such important ion destruction channel in the astrophysical plasma environments. These barrier-less reactions lead to the electron capture into the ion and subsequent dissociation into neutral fragments. This reaction is called dissociative recombination (DR) and it is often accompanied by kinetic energy release (E_{KER}) into the products to account for energy conservation [7, 8]. The energetic neutral products can initiate further reactions with other ions in the ISM.

The HeH$^+$ ion has been predicted to be first molecule formed in the early universe [9, 10, 11, 12]. In the recombination era, expansion of Universe led to lower temperature and in consequence photoionization also reduced which in turn led to formation of neutral He. In next step HeH$^+$ formed from radiative association with still ionized H$^+$. The radiative cooling of infrared active HeH$^+$ also enhances the cooling in the recombination era. Cooling of this type can help in the gravitional collapse of gas clouds and consequently, in the formation of first stars [10, 3]. Recently the HeH$^+$ ion has been detected for the first time in planetery nebula NGC 7027 from the rotational state transitions $(0 \rightarrow 1)$ [13].

The astrochemical models based on a network of formation and destruction reactions require rate coefficients as input, at best from experimental studies conducted at astrophysically relevant conditions. Moreover, the complex pathways of the dis-

sociative recombination involving molecular Rydberg states make this process very interesting from the theoretical point of view. Experimental studies at well defined conditions are also needed to benchmark the corresponding quantum dynamics theory models.

In the ongoing quest of laboratory measurements, room temperature magnetic ion storage rings have been very successful in the area of DR measurements of light molecular ions stored at several MeV [14, 15, 16]. At several facilities world wide ion storage rings have been in operation for more than two decades [17, 18, 19]. Equipped with electron cooler, the velocity-matched electron and ion beams interactions lead to phase space cooling of the ions [20]. The phase space cooled ion and electron merged beams offers well-controlled collision conditions for DR experiments. In addition, the circulating ion beam's internal excitations (vibrational and rotational) thermalize to the ambient blackbody radiation field of 300 K. In spite of all advantages and successes of room temperature magnetic storage rings, the 300 K blackbody radiation field does not allow the stored ions with a dipole moment to deexcite to the lowest rotational levels which are relevant for cold interstellar plasmas. Furthermore, the storage of heavier ions is limited by the bending capability of the dipole magnets of the storage ring.

For this purpose, cryogenic electrostatic ion storage rings paved the way forward. In the cryogenic temperature of below 10 K, the ion collisions with rest gas particles are largely reduced which allows ion beam storage for long time needed for radiative rotational relaxation. This enables the measurement of ro-vibrationally cold molecules at new unexplored time scales. Also, electrostatic ion storage ring makes it possible to store heavy complex molecular species [21]. The storage ring device can also be used in laser-molecular ion interaction studies, cluster ion studies and ion-neutral atoms collisions, etc. [22, 23, 24, 25]. Thus, a new generation of storage rings have been built to study these classes of reactions [24, 25, 23]. Among these storage rings, the cryogenic storage ring (CSR) at the Max Planck Institute for Nuclear Physics in Heidelberg is the only electrostatic storage ring equipped with an electron cooler. The operational ion energy in the CSR is up to 300 keV and electron beam energy is in few eV range. In this work we investigate DR experiment under these conditions and in particular study the DR of HeH$^+$ ions.

The thesis is structured as follows. Chapter 2 gives a general introduction to the theory of electron-ion collisions with emphasis on the dissociative recombination (DR). DR fragmentation pathways in low and high collision energy regions for

HeH$^+$ are discussed in terms of the potential energy curves. In addition, the radiative cooling model of HeH$^+$ ions in a cryogenic environment is also described. In chapter 3, the experimental framework of the merged beams setup is laid out with the overview of the cryogenic storage ring (CSR) and the electron cooler. The merged beams kinematics and detection system for the fragmentation experiment is discussed. Furthermore, the rate coefficient of the merged beams experiment is introduced in a general scenario including the position dependent nature of the relative velocity in electron-ion collision. In chapter 4, a magnetic field analysis program is used to simulate the electron beam trajectory in the electron cooler and in the overlap region with ion beam. The role of the overlap geometry of electron-ion merged beams, space charge of the electron beam and drift tubes potential induced electron beam energy change are studied. Based on this, the electron-ion collision energy distribution is modelled and the influences of individual components are discussed. In Chapter 5 experimental studies with the HeH$^+$ ion and a measurement of the rotationally cold absolute DR rate coefficient are presented. The use of drift tubes in the interaction region and scaling of the results is also shown. Finally Chapter 6 gives a summary of the obtained results in electron-ion collision experiments with the more precise knownledge merged beams geometry of the electron cooler and it concludes with an outlook on possible future measurements and improvements.

2 Molecule and electron collision processes: Overview

Molecular ion and electron collisions occur in environments ranging from artificial plasma to the early universe. The dynamics of these collision processes are described in terms of potential energy surfaces (PES). In this chapter, we start with a brief description of PES. The general electron-ion fragmentation processes are briefly introduced. Later, a detailed discussion on the dissociative recombination (DR) mechanism is presented.

In the second part, the present experimental status and recent theoretical understanding of DR process of HeH^+ ions is presented. Also, a simple model of the rotational cooling of the infrared active HeH^+ ion in a 20 K radiation field environment is presented.

2.1 Potential energy surfaces

A molecular system is commonly described in terms of the Schrödinger equation [26]

$$\hat{H}\Psi = E\Psi \tag{2.1}$$

where $\hat{H}$ is the Hamiltonian of the molecule, $\hat{H} = \sum_{i=1}^{N_e} \hat{T}_{el}(\boldsymbol{r}_i) + \sum_{j=1}^{N_n} \hat{T}_n(\boldsymbol{R}_j) + V_c(\boldsymbol{r_i}, \boldsymbol{R_j})$. Here, $\vec{r}_i$ and $\vec{R}_j$ denote the coordinate vectors of the electrons (i = $1...N_e$) and nuclei (j=$1...N_n$) in the center-of-mass frame and $V_c(r_i, R_j)$ symbolically describes the potential due to all Coulomb interactions. Ψ is the total wavefunction and E is the total energy of the molecular system. However, solving for exact solution to this equation for the system is very complicated. To address this issue, there were many physically motivated approximations introduced.

Because of large mass difference between the electrons and nuclei, electrons react instantaneously to the motion of the nucleus. Due to very small nuclear motion $\hat{T}_n$ compared to $\hat{T}_{el}$, $\hat{T}_n(\boldsymbol{R}_j)$ introduced as perturbation terms to the approximate

of a rigid nuclear framework. The corresponding approximation is known as the adiabatic approximation [26]. The Hamiltonian of the system can be expressed as

$$\hat{H} = \hat{H}_0 + \hat{H}' \tag{2.2}$$

where $\hat{H}_0 = \sum_i \hat{T}_{el}(\boldsymbol{r}_i) + V_c(\boldsymbol{r_i}, \boldsymbol{R_j})$ is the unperturbed Hamiltonian and $\hat{H}' = \sum_j \hat{T}_n(\boldsymbol{R}_j)$. Also, we consider here only a diatomic molecule, $N_n = 2$, and introduce the relative coordinate $\boldsymbol{R} = \boldsymbol{R}_1 - \boldsymbol{R}_2$. The unperturbed Schrödinger equation then is,

$$\hat{H}_0 \phi^{el}(\boldsymbol{r}_i, R) = E^0(R)\phi^{el}(\boldsymbol{r}_i, R) \tag{2.3}$$

where ϕ^{el} is the electronic wavefunction for the rigid nuclear configuration. $\phi^{el}(\boldsymbol{r}_i, R)$ depends on electronic coordinates $\boldsymbol{r}_i$ and the internuclear distance R enters as parameter. Moreover, $E^0(R)$ is the eigenvalue for the rigid configuration. For each (fixed) nuclear configuration $\boldsymbol{R}$ this yields a stationary state of the molecule. Therefore, ϕ_{el} form a basis set and the total wavefunction Ψ can be described as,

$$\Psi(\boldsymbol{r}, R) = \sum_m \chi_m(R)\phi_m^{el}(\boldsymbol{r}, R) \tag{2.4}$$

where the factor $\chi_m(R)$ is the wavefunction representing the nuclear motion when the electronic system is in state m. Substituting Ψ in eqn. 2.1, multiplying with ϕ_n^{el*} and integrating over the electronic coordinates $\boldsymbol{r}_i$, yields

$$\int \left[\phi_n^{el*}(\boldsymbol{r}, R)(\hat{H} - E) \sum_m \chi_m(\boldsymbol{R})\phi_m^{el}(\boldsymbol{r}, R) \right] d\boldsymbol{r}_i = 0 \tag{2.5}$$

Using $\hat{H} = \hat{H}_0 + \hat{H}'$ and eqn. 2.3, the following solution is obtained.

$$\hat{H}_0 \phi^{el}(\boldsymbol{r}, R) = E^0(R)\phi^{el}(\boldsymbol{r}, R), \tag{2.6a}$$

$$\hat{H}' \chi_n(\boldsymbol{R}) + \sum_m (c_{nm}\chi_m(\boldsymbol{R})) = (E - E_n^0(R))\chi_n. \tag{2.6b}$$

Here eqn.2.6 is equivalent to the Schrödinger eqn.2.1 and, c_{nm}[1] is a coupling matrix. They describe how two different electronic states n and m are coupled through nuclear motion. If the coupling term is completely neglected, the outcome is the so-called Born-Oppenheimer approximation [27]. The nucleus with kinetic energy T_N moves within a potential of E_n. The total wavefunction Ψ of the molecule in

---

[1]taken from eqn. 2.11 [26]

an electronic state reduces to a single term as $\Psi_n(\boldsymbol{r}, R) = \phi_n^{el}(\boldsymbol{r}_i, R)\chi_n(\boldsymbol{R})$. This means wavefunction is factorized in electronic and nuclear counterparts ϕ_n^{el} and χ_n. The electronic eigenenergy with mutual Coulomb interaction of the nuclei, $E_n^0(R)$ is defined as the potential energy function acting on the nuclei. This is also called potential energy curve of the diatomic molecule. The nuclear wavefunction $\chi_n(\boldsymbol{R})$ satisfies the Schrödinger equation with $E_n^0(R)$ as potential in order to describe nuclear motion (rotation and vibration).

The minimum of the PEC is the geometrical equilibrium for the molecule and vibration of the molecule is defined as oscillations around the point of minimum. Also, a reaction of molecule can be illustrated as a pathway along the PEC. The fragmentation process of a molecular system can be described by an unbound PEC. These PECs are often only repulsive with an energetic minimum at infinite geometric separation of the fragments.

Again, considering eqn.2.6 can bring in some additional terms. The coupling matrix c_{nm} can be grouped into diagonal and non-diagonal terms. If diagonal terms are retained as c_{nn}, a new potential energy is defined as adiabatic approximation. The adiabatic approximation modifies the Born-Oppenheimer potential as $E_n^{'}(R) = E_n^0(R) + \langle n|\hat{T}_n(\boldsymbol{R})|n\rangle$, where $|n\rangle$ are the electronic states ($|n\rangle = \phi_n^{el}(\boldsymbol{r}_i, R)$). The adiabatic correction shows the role of nuclear mass and also, dictates the slight difference in potential energy of isotopes of the molecule.

The adiabatic approximation is an ideal approach for PEC corresponding electronic states well separated in energy. If this condition is violated for certain internuclear distance R, the curve crossing between two PECs of same symmetry is not allowed according to the non-crossing rule of Von-Neumann and Wigner [28]. In case two PE curves come closer to each other they bend away from each other. This exchanges the electron configuration and, hence, the asymptotic behaviour for $R \rightarrow \infty$. In addition, at avoided crossing there is a possibility for a radiationless transitions to other state which are known as non-adiabatic or *Landau-Zener* transitions.

During a fragmentation process, the velocity of nuclear motion can become comparable to other motions. And, hence the previously assumed mechanisms will not always sufficiently explain the dynamics. Therefore, a diabatic potential curve is often used to describe the fragmentation process. Here, curve crossings between two electronic states of the same symmetry are allowed. The diabatic approximation is useful for treating the nonadiabatic transitions between two electronic states [29]. In

this regime, it is easy to determine the candidate states for transitions, and coupling strength calculations between them are also possible .

2.2 Ion-electron collision processes

A collision between a molecular ion and an electron can trigger several kinds of reactive processes.Among different reactions, fragmentation is one of the most fundamental processes causing destruction of molecules in plasma environments. The fragmentation reaction between ion and electron leads to neutral or charged fragments depending on the collision energy of the incoming electron and type of PEC accessed in the collision. Also, the fragmention products can be in an excited state. Moreover, collisions can lead to autoionization into the molecular ion but in different excited or even de-excited states. A short overview of various dissociation mechanisms for a general diatomic molecular ion AB^+ is described here. These processes strongly depend on the collision energy of the elctron. In thermal plasmas, the energy is given by $k_B T \approx 10 - 1000$ K ($E_e \sim 0.001 - 0.1$ eV) and then is in the range of rotational and vibrational excitation energy. In hot plasmas or in colliding beams experiment, impact energies up to few tens of eV can be realized.

If the energy of electron is sufficient enough to promote the molecular ion AB^+ into its vibrational continuum, the system can dissociate via dissociative excitation (DE) with neutral and ionic fragments. It can occur directly or via an intermediate state AB^*. The charge state of the fragment depends on the internal configuration of the molecules.

$$AB^+ + e^-(E_e) \longrightarrow \begin{cases} A^+ + B + e^- \\ A + B^+ + e^- \end{cases} \tag{2.7}$$

Another important class of fragmentation is the resonant ion-pair formation (RIP). Here, an electron of intermediate energy regime (few eV) first gets captured into an intermediate state AB^{**}. Later, it stablizes through the formation of a charged ion pair.

$$AB^+ + e^-(E_e) \longrightarrow AB^* \longrightarrow \begin{cases} A^+ + B^- \\ A^- + B^+ \end{cases} \tag{2.8}$$

8
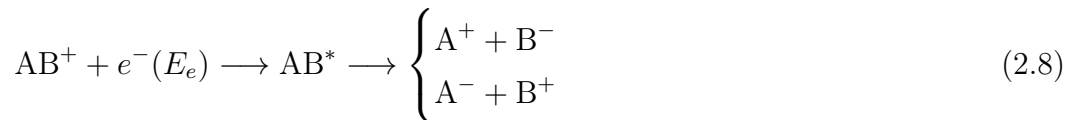
2.2.1 Dissociative recombination

An important class of fragmentation reactions where only neutral fragments are formed after a collision of a molecular ion with an electron is dissociative recombination (DR). DR is exothermic in nature; the excess internal energy is converted into kinetic energy of the fragmented nuclei. For a diatomic positively charged molecular ion AB^+ in a v, J vibrational and rotational quantum state colliding with an electron of energy E_e, DR process can be summarized as

$$AB^+(v, J) + e^-(E_e) \longrightarrow A(n) + B(n') + E_{KER} \tag{2.9}$$
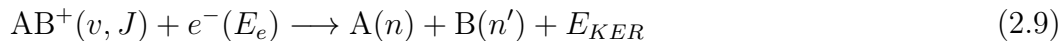
Here n, n' are atomic final-state quantum numbers of the fragments and E_{KER} is the kinetic energy release. E_{KER} are the characteristic of molecular structure and dynamic propagation into different pathways along PES. DR rate coefficient, E_{KER}, and branching ratio of different final channels can be studied as a function of well defined electron collision energy. Also, angular anisotropy of the reaction as a function of electron collision gives insight into the fragmentation direction [30]. In the low-collision energy region, initial internal state of the molecular ion plays a major role in the DR rate coefficient [31]. We will discuss for the case of HeH^+ theoretically in sec. 2.4 and experimentally in sec. 5.2. First we will discuss mechanisms for the DR reaction and consider potential energy curves in the diabatic representation.

(a) Direct DR at low energy

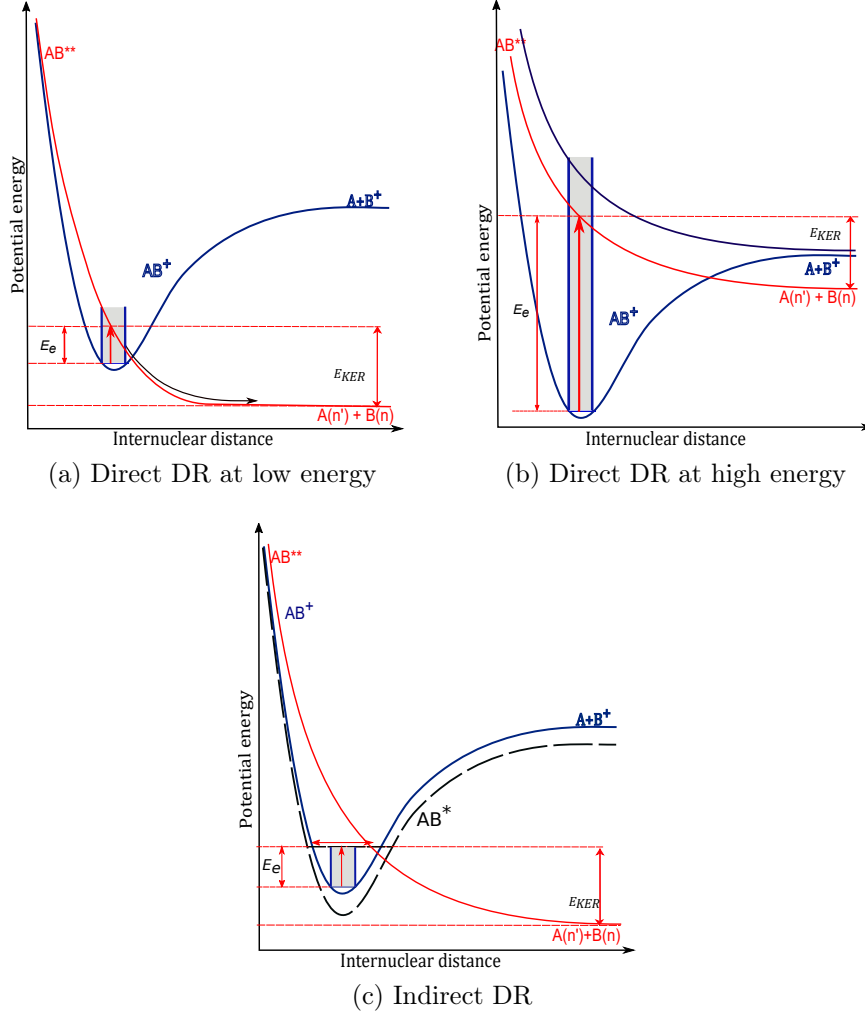(b) Direct DR at high energy

(c) Indirect DR

Figure 2.1: Sketch of the potential energy curves (PEC) for direct DR (a and b) and indirect DR (c) mechanism for a diatomic ion. Blue curve is PEC of the ground state of the molecular ion. Red is AB** dissociative state and black curve is the AB* Rydberg state. Electron with energy E_e is shown in red arrow and the E_{KER} is depicted by the red arrow. The shown PECs are defined in diabatic picture.

Direct DR

$$AB^{+}(v, J) + e^{-}(E_e) \longleftrightarrow AB^{**} \longrightarrow A(n) + B(n') + E_{KER} \tag{2.10}$$
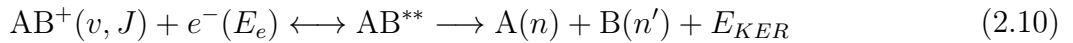
In direct DR, a repulsive neutral state is directly accessed in the Franck-Condon region of the molecular ion, as depicted in fig. 2.1[32]. After capture, there is a

finite probability of autoionization as AB** lies initially above the energy of the molecular ion. As the dissociation proceeds along the repulsive curve, it crosses the ion curve and becomes stable with respect to autoionization. The excess energy is imparted to the dissociating fragments. In direct DR, the electron gets captured via purely electronic transition with in the Franck-Condon region of the vibrational state of molecular ion into the steeply decreasing AB** state. Therefore, the cross-section in low-energy region vary as E^{-1} corresponding to the threshold level for an electron-ion collision (see fig. 2.1 (a)) . However, in the high-energy region (10-30 eV), excited state of cation support several dissociating neutral states still within the Franck-Condon zone and hence, the DR cross section will show a broad peak around E_0.

Indirect DR

The DR mechanism other than direct electronic coupling between states leading to strong cross-section at low-energy is the result of a new mechanism called indirect DR[33].

$$\text{AB}^+(v, J) + e^-(E_e) \longrightarrow \text{AB}^* \longrightarrow \text{AB}^{**} \longrightarrow \text{A}(n) + \text{B}(n') + E_{KER} \qquad (2.11)$$
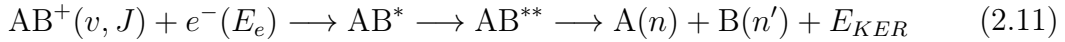
In the indirect DR process, an electron with kinetic energy E_e is resonantly captured into an intermediate state, the vibrationally excited Rydberg state AB*, as shown in the fig 2.1 (b). In terms of PEC, there are large number of neutral Rydberg series converging to the ionic ground state. All these states have vibrational levels converging to vibrational levels of the ionic ground state. Later, electron from the Rydberg state within the extent of the vibrational wavefunction crosses to the dissociative neutral state AB**. Also, the range is extended beyond the Franck-Condon zone of the vibrational ground state of the cation. Therefore, a resonance state act as the gateway to the fragmentation path inaccessible to direct DR [34]. Also, indirect DR is always a resonant process as electron with certain discrete energies only get captured into the vibrational Rydberg state. Therefore, indirect DR the cross-section feature sharp peaks in the cross section. Moreover, the shape of cross-section exhibits complictated spectral features in the continuum where resonances are less separated from each other than by their width [34].

The presented DR process is a short overview of the DR mechanism. A detailed review of the DR process can be found in [8, 7].

2.3 DR of the HeH$^+$ ion

HeH$^+$ is an important prototype molecule for the indirect DR mechanism in low-energy electron collision. The DR process is described as eqn. 2.12. Due to its simple structure and important role in early universe chemistry [10], HeH$^+$ has been studied extensively to predict its cross-section structure [35, 36]. Several experimental studies have been carried out in the past to benchmark the theoretical models [37, 38, 39]. As shown in fig. 2.2, the ground state of HeH$^+$ does not cross any doubly excited repulsive state. In the low-energy region, the fragmentation is dominated by the He + H($n = 2$) channel with $E_{KER} = 1.55$ eV for negligible small impact energy [36]. However, a new product channel opens at 333 meV collision energy leading to He + H ($n = 3$) and completely switches to this state at 577 meV [16]. The neutral fragment imaging was employed for product state distribution study as a function of energy. The E_{KER} of 1.55 eV confirmed He + H($n = 2$) at low energy and E_{KER} of 243 meV after 577 meV collision energy [16].

$$\text{HeH}^+(v, J) + e^-(E_e) \longrightarrow \text{He} + \text{H}(n) + E_{KER} \tag{2.12}$$
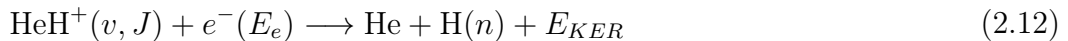
At low energy, the process is driven by the indirect recombination by which the HeH C$^2\Sigma^+$ state is reached. In high-energy region, as shown in fig. 2.2 various doubly excited dissociative Rydberg states HeH** are present within the Franck-Condon region. Therefore, direct DR occurs through electronic states. As several such dissociative states are available, the observed cross section is very broad. Furthermore, dissociative excitation (DE) channels open in the same energy region as shown in the previous measurement [37]. Therefore, DR and DE channels are in direct competition at energies above 1.8 eV.
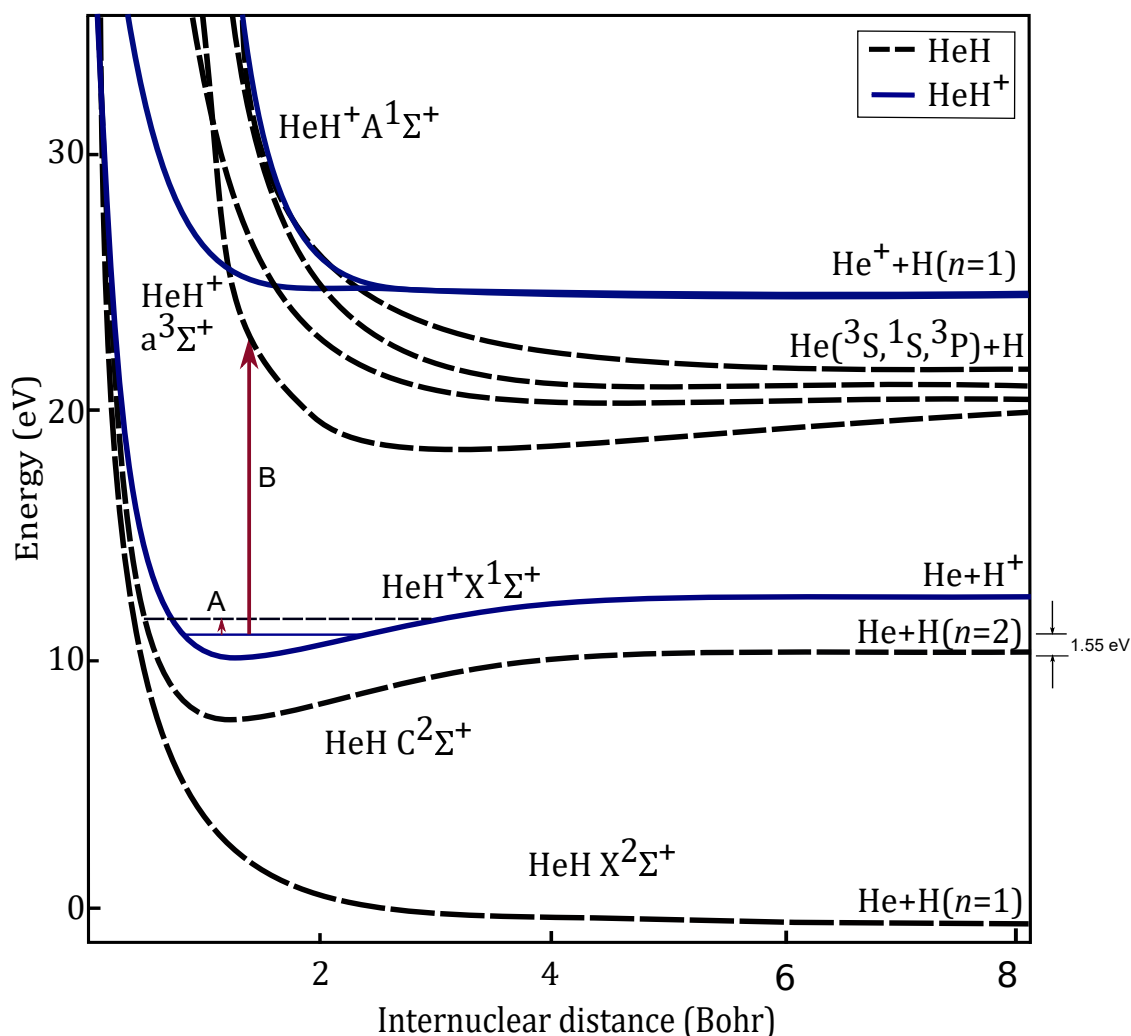
Figure 2.2: Relevant potential energy curves of HeH$^+$ (blue) ion and HeH (dashed black) for DR and DE are shown. The ground state of cation is X$^1\Sigma^+$. The ground state of neutral HeH X$^2\Sigma^+$ is repulsive and the excited Rydberg state C$^2\Sigma^+$ is bound and the primary dissociation route in low-energy DR (see red arrow A). A$^1\Sigma^+$ and a$^3\Sigma^+$ are the excited ionic states, steeply repulsive in the Franck-Condon zone. Also, the excited cation states support several Rydberg states. Red arrow B shows the access to PECs in the high energy range from vibrational gound state. The potential curves of various electronic states are adapted from Stromholm et al.[37].

Fig. 2.3 is the DR spectrum[2] studied in the merged beams setups at the CRYRING and TSR ion storage rings in a room temperature environment [37, 39]. Since HeH$^+$ is an infrared active molecule [40], it interacts with the radiation field at 300 K and the molecule relaxes within less than 0.1 s to the vibrational ground state. In steady state several rotational levels are populated in the vibrational ground state of HeH$^+$, as discussed below. Therefore, the observed spectrum is averaged over the several rotational states of the molecule. Moreover, the electron beam energy spread is in the order of 10 meV [37]. Under these conditions DR rate coefficients is strongest at low E, revealing strong indirect process. Moreover, peak at high energy is due to the direct DR. The detailed study on rotational cooling of HeH$^+$ and electron beam energy spread will be presented later in sec. 2.4 and sec. 3.3.2.
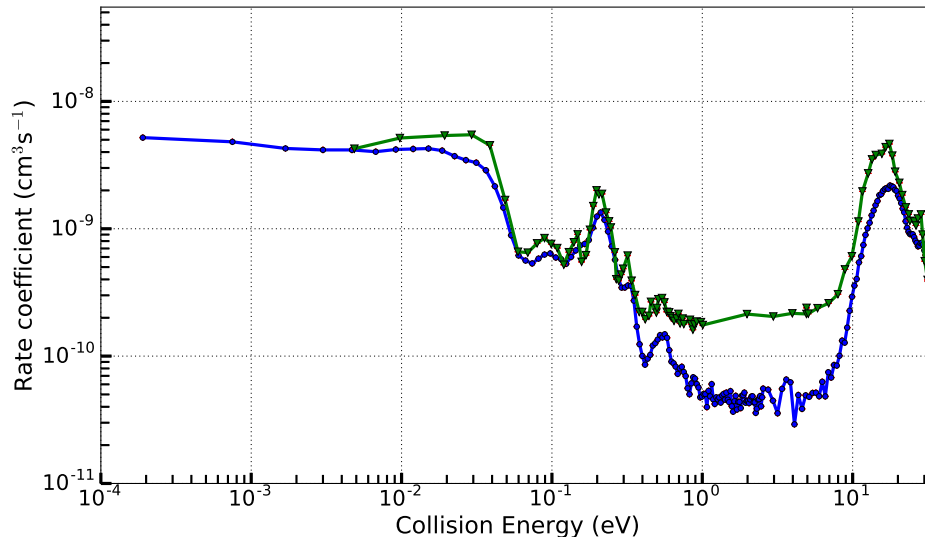

Figure 2.3: Experimental merged beams rate coefficient from CRYRING and TSR at room temperature. The TSR measurement is scaled to the CRYRING data at 0.2 eV.

In recent past, tremendous progress has been made theoretically to predict the DR spectrum of individual rotational levels in the vibrational ground state of HeH$^+$ ion [41]. Čurík et al. calculated DR spectra in the low-energy region upto 2.5 eV as the rate coefficient depends on the initial state of the molecule. On the experimen-

---

[2]DR spectrum is measured in terms of the rate coefficient which is $\alpha = \langle \sigma v \rangle$. where σ is DR cross section and $v = \sqrt{2E/m_{m_e}}$ is the collision velocity at energy E.
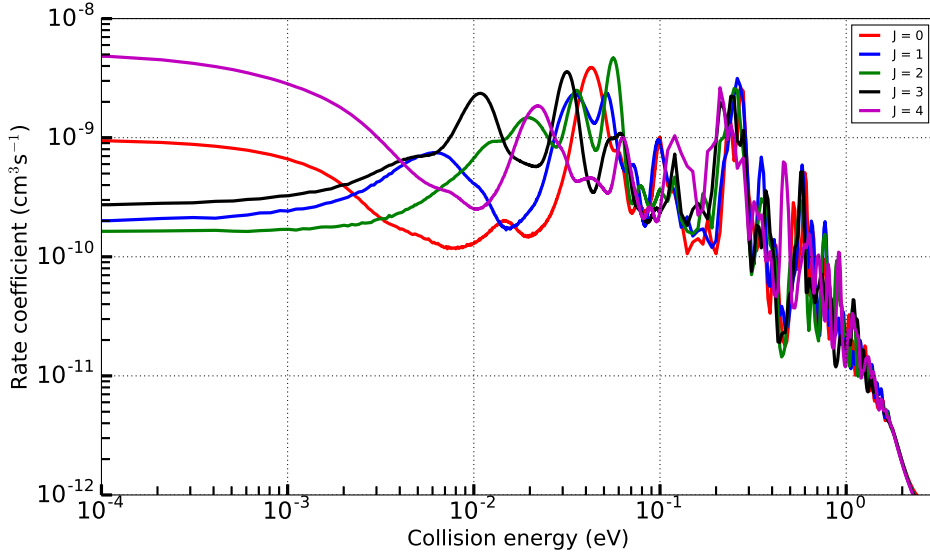
Figure 2.4: Computed DR rate coefficient is presented for $v = 0$ and $J = 0$ - 4 for HeH$^+$. The theoretical cross section is convoluted with the expected electron beam energy spread of $\triangle E_\parallel = 0.1$ meV and $\triangle E_\perp = 2$ meV.

tal side, the requirement of near single J state study is met by our cryogenic ion storage ring where molecular ion can be ro-vibrationally cooled [23]. In addition, photocathode generated electron beam energy spread is lowered by factor ~ 10 than the previous experiments. Here, the cross-section calculated from the theory is used and convolved with expected electron beam energy spread of the CSR electron cooler and overlap geometry of the merged beams set up in the CSR (see sec. 3.3.2). Fig. 2.4 shows there are several peaks in the rate coefficient even after electron beam energy spread. The features of the spectra especially $J = 0$ will be compared and discussed with the experimentally obtained spectra.

2.4 Rotational cooling of HeH$^+$ ions by the radiative emission

HeH$^+$ ions require an ion source with a high temperature plasma for their production. The temperature of the source plasma is typically ~ 3000 K leading to the population of vibrationally and rotationally excited states. Since the ion has a dipole moment, excited vibrational states emit radiations. Vibrational relaxations occur in

a time scale of several milliseconds. When experiments are performed with stored ions, it can be assumed that they are essentially in the vibrational ground state [39]. On the other hand, the radiation field in the environment of the ions is important regarding the rotational populations. The energy density can be written according to the Planck's radiation law for a particular frequency ν [42].

$$\rho(\nu) = \frac{8\pi hc\nu^3}{e^{h\nu/kT} - 1} \tag{2.13}$$

where c is the speed of light and k_B is the Boltzmann constant. Furthermore, the rotational energy of a linear diatomic molecule is given as,

$$E_J = BJ(J+1) \tag{2.14}$$

where J is rotational quantum number and B is the rotational constant of the molecule. The energy difference between two rotational levels increases linearly as $\triangle E_{J,J-1} = 2BJ$.
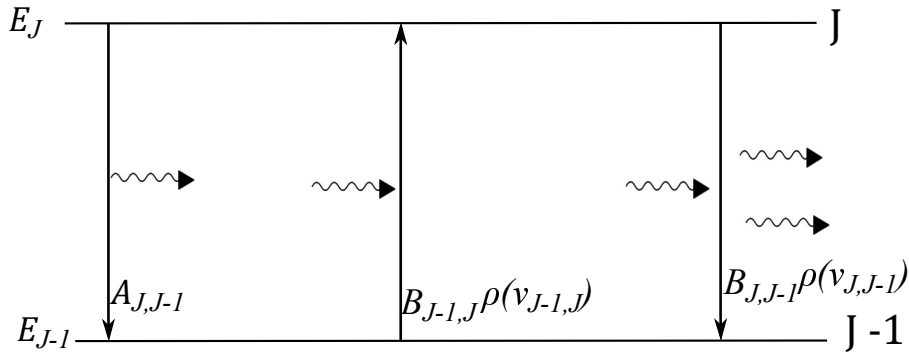

Figure 2.5: Interaction of radiation field of frequency $\nu_{J,J-1}$ interacts with rotational levels of molecule with population N_J in level J and N_{J-1} in level $J-1$. The radiation field of photon energy density $\rho(\nu_{J,J-1})$ drive transition between J and $J-1$. $B_{J-1,J}$ is the Eintein's coefficient of stimulated absorption, represents the coupling between two-state system and radiation field. Likewise, $B_{J,J-1}$ is the Eintein's coefficient of stimulted emission and $A_{J,J-1}$ is the spontaneous emisison (see text).

Fig. 2.5 shows of how the radiation field $\rho(\nu_{J,J-1})$ interacts with a two level system. The details of such interactions can be found in detail in Bernath [43]. In presence of a photon field the Einstein coefficients define the population ratio between the states as

$$\frac{N_J}{N_{J-1}} = \frac{B_{J-1,J}\rho(\nu_{J,J-1})}{A_{J,J-1} + B_{J,J-1}\rho(\nu_{J,J-1})} \tag{2.15}$$

where the statistical equilibrium also implies

$$\frac{N_J}{N_{J-1}} = \frac{g_J}{g_{J-1}} e^{-E_{J-1,J}/k_B T} \tag{2.16}$$

where $g_J = 2J + 1$ is the degeneracy of the energy level J.

Comparision of eqn. 2.16 and eqn. 2.15, the Einstein coefficients leads to the relations

$$\frac{B_{J-1,J}}{B_{J,J-1}} = \frac{g_J}{g_{J-1}} \quad \text{and} \quad \frac{A_{J,J-1}}{B_{J,J-1}} = 8\pi h \nu_{J,J-1}^3 \tag{2.17}$$

On the other hand, the Einstein coefficient A is given by

$$A_{J,J-1} = \frac{16\pi^3 \nu_{J,J-1}^3}{3\epsilon_0 h} \frac{J}{2J+1} \mu^2 \tag{2.18}$$

where μ is the dipole moment of the molecule.

The Einstein's coefficient A of spontaneous emission gives the probability of transition per unit time interval from $J \longrightarrow J - 1$. The inverse of spontaneous emission gives the lifetime of a system in an excited state with a single decay channel. The spontaneous emission is proportional to ν^3 (transition energy), for higher J-states decay rate is faster. The dipole moment remains approximately constant for lower rotational levels. For the present calculation, the spontaneous emission rate is taken from Engel et al.[40].

Based on the relations presented above, a rotational cooling model of HeH$^+$ ion is developed. In the model, the 10 lowest rotational states have been considered. A rotational state J only couples to $J - 1$ via photon emission and $J + 1$ via photon absorption according to the selection rule $\triangle J = \pm 1$. Also, there is no loss to the total population in the radiative transitions. Time evolution of the population in several rotational states is developed according to the following rate equation:

$$\frac{dp_J}{dt} = p_J[-A_{J,J-1} - \rho(\nu_{J,J-1})B_{J,J-1} - \rho(\nu_{J,J+1})B_{J,J+1}] \\ + p_{J+1}[A_{J+1,J} + \rho(\nu_{J+1,J})B_{J+1,J}] + p_{J-1}[\rho(\nu_{J-1,J})B_{J-1,J}] \tag{2.19}$$

A numerical simulation has been performed to solve the coupled differential equation upto 100 s.

In fig. 2.6 the molecules reach rotational equilibrium after ~ 10 s at 300 K with several rotational levels populated. However, at 20 K environment fig. 2.7 shows higher J-states continue to decay faster due to the narrow field. Hence, in a low temperature radiation field and with sufficient storage time, especially $J = 0$ population can be reached. Thie will be used in the experiments in this thesis.
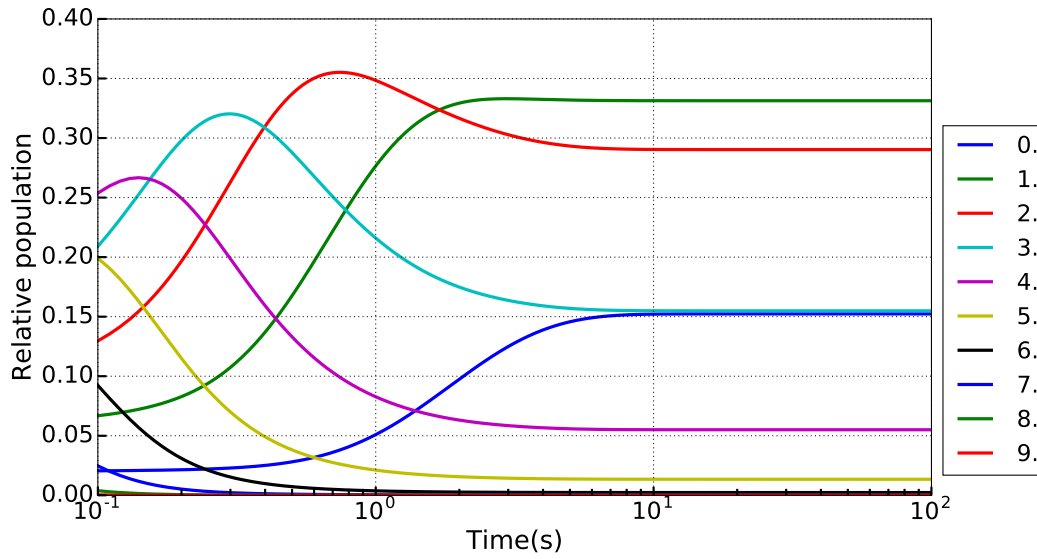
Figure 2.6: Radiative cooling of populations for 10 lowest rotational states. The initial temperature of the ion is 3000 K and equilibrates at 300 K in a thermal cavity (legends 0-10 are rotational states).
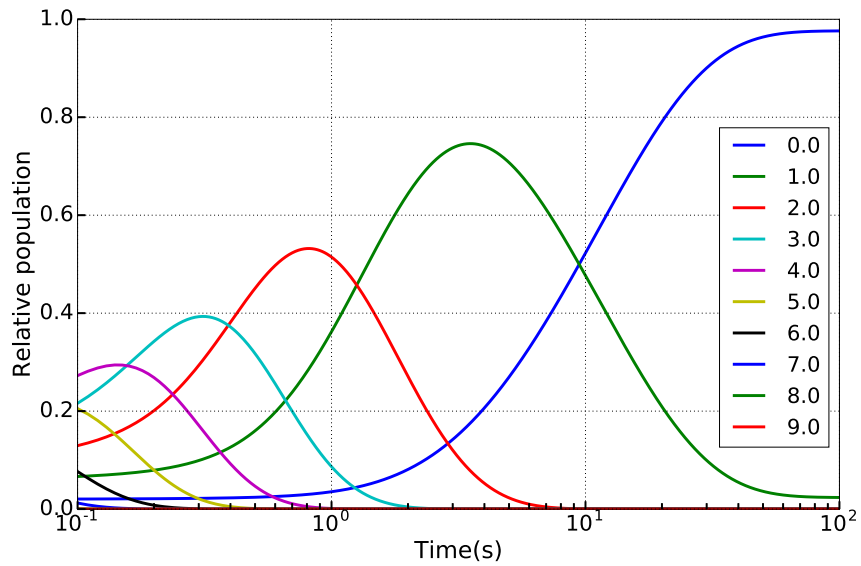

Figure 2.7: Radiative cooling of populations for 10 lowest rotational states. The initial temperature of the ion is 3000K and equilibrates at 20 K inside CSR (legends 0-10 are rotational states).

18

3 Fast-beam fragmentation studies

In this chapter, experimental details of the electron-ion fragmentation reaction discussed in the previous chapter is presented. It starts with a general overview of the newly comissioned electrostatic ion storage ring, CSR and its several experimental programs. The dynamics of collisions in merged electron and ion beams can be described considering individual beams of well-defined energy. On this basis, the principle of electron cooling and aspects of the electron beam energy spread are presented. Consequently, an ion storage ring in combination with an electron cooler offers internally as well as translationally cold stored ion beams.

The fragments detection scheme of collision experiments is also presented. In fast beam collision reactions, the fragments emerge in a narrow cone and fly ballistically in forward direction leaving the ion beam orbit. In many cases, this allows the detector to be sensitive over effectively 4π solid angle regarding the particle emission in the center-of-mass frame.

3.1 Cryogenic storage ring: overview

The Cryogenic Storage Ring (CSR) located at Max Planck Institute for Nuclear Physics in Heidelberg is a fully electrostatic storage ring. The energy of the stored ion can be varied from 20 to 300 keV per charge. Figure 3.1 shows the schematic overview of the CSR. The quadratic storage ring has a circumference of 35.12 m with four 2.6 m straight sections [23]. The ion optical elements are placed in the four symmetric rectangular corners 1-4, from the injection in counter clockwise direction. These are a combination of two electrostatic 6^0 cylindrical deflectors (3) and two 39^0 cylindrical deflectors (2). The first 6^0 deflector in corner 1 also serves the purpose of fast switching the ion beam. For focussing of the stored ion beam each corner is equipped with two quadrupole doublets.

The four straight sections of the CSR serve as the experimental platforms and for beam diagnostics. Section A of the CSR is dedicated for ion-neutral reactions. Neutral beam is produced by the photodetachment of anion (e.g. H^-, O^-, D^- and

C$^-$ etc.) in the injection beam line prior to the CSR and can be merged with already stored ions [44]. In addition, it consists of RF bunching system (5) and the beam viewer (6). In section B, an electron cooler for phase space cooling and merged electron-ion beams collision studies has been implemented. This section is also equipped merged and crossed laser-ion beams set up for photodetachment or photodissociation experiments. In the corner 3 after section B there are detectors to collect the neutral and charged reaction products. NICE, Neutral particle Imaging in Cryogenic Environment is the neutral particle detector positioned next to 39^0 deflector to collect nearly coincident atomic or molecular fragments in dissociation [45]. The COMPACT, COld Movable PArticle CounTer, is an MCP based counting detector for electron or photon induced charged or neutral products [46, 47]. It is movable across the beam vacuum chamber of the CSR. Both detectors will be discussed in detail in sec. 3.5. Section C is used for the beam diagnostics. It features a Schottky pick-up, a current pick-up for bunched ion beams and a beam viewer. In addition, it also consists of a vertical and a horizontal capacitive pick-up electrode pair [48]. And, in the fourth straight section (D) a reaction microscope to study the collisions of stored ions with an internal gas target will be implemented.

3.1.1 Ion beam lifetime

In order to achieve the ambient cryogenic temperature below 10 K inside the experimental chamber (EC) of the CSR, structure of the CSR mimics the design of a standard cryostat [49]. The EC of the CSR is maintained at ultra-high vacuum. For avoiding thermal coupling to the environment due to convection, it is enclosed in an isolation vacuum. Furthermore, the EC is covered with additional two layers of thermal shields at 40 K and 80 K, which act as infrared screens. Also, the 80 K shield is wrapped in multi-layer insulation to lower the 300 K black-body radiation onto the inner layers and, hence the experimental chambers.

Under cryogenic temperature, ultra-high vacuum in the order of 10^{-14} mbar (room temperature equivalent) has been observed and, lifetimes of stored ions up to $\sim$ 2500 s were achieved [23]. Hence, infrared active molecules can relax towards their ro-vibrational ground state. In previous experimental campaigns, photon-induced rotational-state resolved reactions have been performed on OH$^-$ and CH$^+$ molecular ions [50, 51]. The first studies of electron-induced reactions in the CSR are described in this thesis.
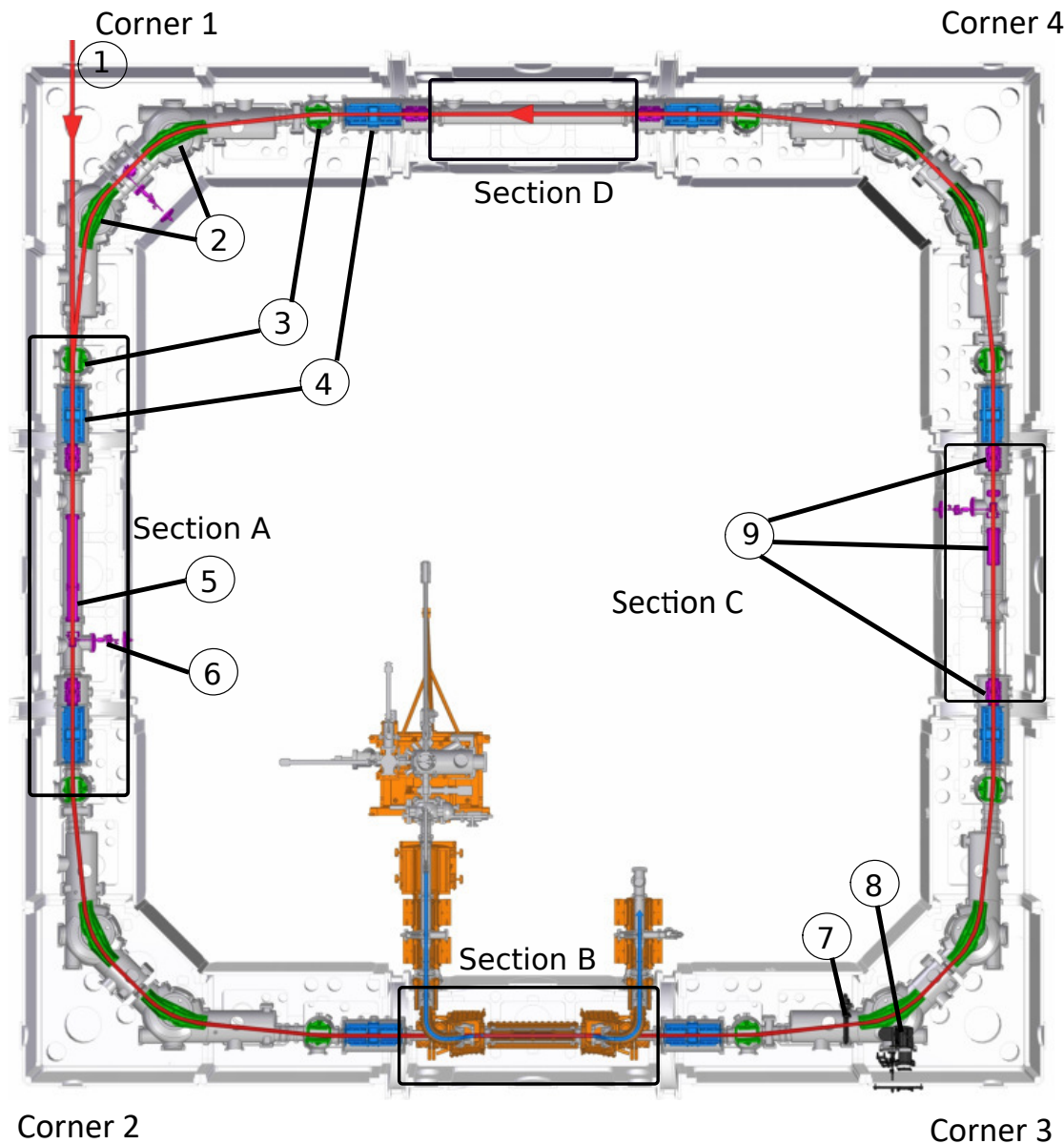
Figure 3.1: Schematic overview of the CSR. The ion is injected from corner 1, 39^0 deflectors (2) and 6^0 deflectors (3) confine ions in closed orbit of the CSR. Section A consists of ion-neutral merged beam set up and RF bunching system (5). In section B electron cooler is installed to study ion-electron collisions experiment with counting (7) and neutral particle detector (8). The CSR houses various tools for beam diagnostics in section (C) with current, Schottky, and position pick ups (9, counting counterclock wise). Three destructive beam-viewers are distributed to different locations in the beam line (6). Section D will be equipped with reaction microscope.

3.2 Principle of electron cooling

High resolution electron-ion collision experiments with merged beams require a well-defined ion beam of small diameter with low divergence and small momentum spread. However, according to Liouville's theorem the phase-space volume occupied by the position and momentum of an ensemble of stored ions remain unchanged in the absence of external forces. To overcome this limitation, there are a number of cooling techniques for ion beam manipulation available such as radiation damping or stochastic cooling [52]. Electron cooling has been very succsesful in efficient phase space cooling of the stored ions [20].

A cold, intense and continuously regenerated electron beam is merged with a hot stored ion beam. For an ion beam of mean energy E_i, the electron beam energy is adjusted to have the same mean velocity as the ion beam. Therefore, the velocity matched electron energy E_c needs to fulfill the condition

$$E_c = \frac{m_e}{m_i} E_i \tag{3.1}$$

where m_e and m_i are the mass of electron and ion, respectively. The ions undergo multiple Coulomb collisions and energy is transfered from hot ions to the cold electron beam. This means that the phase space occupied by particles becomes smaller and the ion beam can cool down nearly to the electron beam temperature T_e. The final ion beam temperature is limited by the intra-beam scattering of the ion beam and by rest gas collisions. The cooling time for an ion beam of mass m_i and charge state Z by an electron beam with density n_e and temperature T_e scales as [53]

$$\tau_{cool} \propto \frac{m_i}{Z^2} \frac{T_e^{3/2}}{n_e} \tag{3.2}$$

For heavier ions, cooling time τ_{cool} is greatly increased. To counterbalance this effect, the electron beam density must be as high as possible and beam temperature should be very low. For this purpose, adiabatically expanded GaAs based photocathode is used [54]. The typical beam temperature goes down to $\sim$ 1-2 meV range.

In case of molecular ions, electron-ion inelastic collisions can even lead to vibrational or rotational excitations and de-excitation.

3.3 Electron Cooler

3.3.1 Basic setup

In the CSR electron cooler, a low energy electron beam is produced in a GaAs photocathode, magnetically guided and merged with stored ion beam in the CSR orbit. The merged electron-ion beams collision can be studied from near 0 to several eV collision energy in the center-of-mass of an ion and an electron. The photocathode is operated in space charge limited mode, where electron density n_e is defined by the space charge of the electron beam and not by the emissivity of the cathode itself. The maximum current I_e depends only on the applied extraction voltage U_{ext} and follows the Child-Langmuir law [55].

$$I_e = p U_{ext}^{3/2} \tag{3.3}$$

where p is the perveance of the gun, which depends on the geometrical properties of the photocathode and is typically of the order of 1μA V$^{-3/2}$.

Fig. 3.2 shows the schematic set up of the electron cooler. The size of photocathode defines initial size of the electron beam. The effective emitting surface of photocathode is 3 mm defined by the Pierce electrode [48]. The magnetic expansion factor (see sec. 3.3.2) is defined as the ratio of magnetic field in two adjacent regions. In the room temperature region, first expansion is defined as $\alpha_1 = B_1/B_2$ and corresponding size of electron beam is $r_1 = \sqrt{\alpha_1} r_{cath}$. where r_{cath} is the radius of photocathode beam and $\alpha_1 = 10$. The room-temperature section is followed by the cryogenic section made up of high temperature superconducting coils (HTS). In the toroidal bend and merging region the B-field remains constant. The interaction section consists of a long solenoidal field of strength B_3 and, hence, the transition provides a second beam expansion of $\alpha_2 = B_2/B_3$. Therefore, final size of the electron beam in the interaction section is given as

$$r_{beam} = \sqrt{\alpha_1 \alpha_2} r_{cath} = \sqrt{20} \times 1.5 = 6.7 \ mm \tag{3.4}$$

Consequently, density of the expanded electron beam in the interaction region also decreases to $n_e^f = n_e/\alpha$.
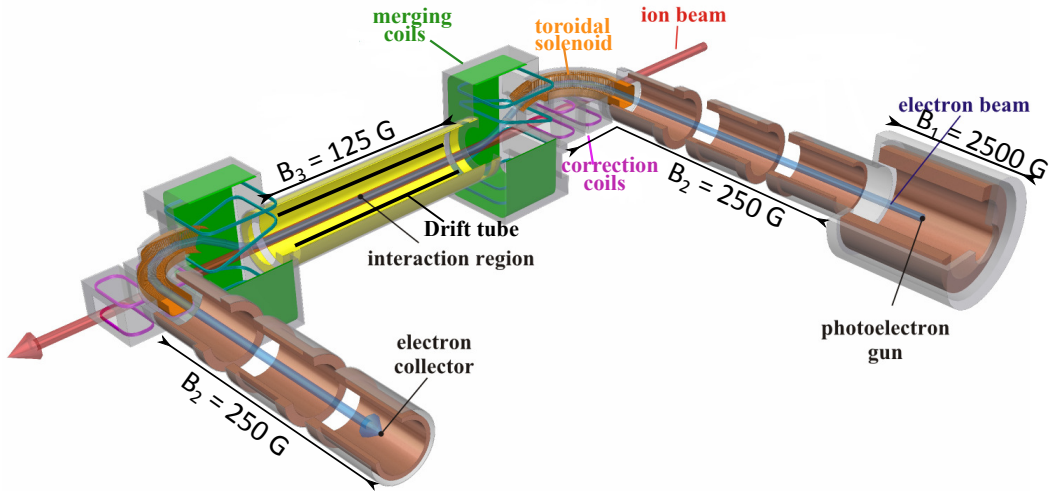
Figure 3.2: Schematic diagram of CSR electron cooler device. The electron beam (shown in blue) is produced at photocathode, inside the high magnetic field solenoid, $B_1 = 2500$ G. Subsequently, three room temperature solenoids of field strength $B_2 = 250$ G, guide and expand electron beam (see text). The toroidal coils bend the electron beam parallel to the ion beam (shown in red) and, merging coils with superposition B-field in longitudinal and vertically downward merges with ion beam. In the interaction region, electron and ion beams are merged and magnetic field is further decreased to $B_3 = 125$ G. (Image taken and modifield from Stephen Vogel [48].)

The interaction section consist of a series of drift tubes, which are used in case of the electron beam deceleration scheme discussed below (see sec. 4.4). In a similar fashion as described above, the electron beam is demerged and guided outside of the CSR cryogenic section. The beam is also compressed by factor 2 and guided to an analyzing main cup set up for electron current measurement. A detailed study on magnetic guiding field conditions and requirements will be presented in sec. 4.2.2.

3.3.2 Magnetised electron beam

The expansion of electron beam discussed in previous section is the manifestation of adiabatic transport of electron beam from high B-field to low B-field region [56]. The adiabatic method makes use of invariance criteria: (i) the product of squared electron beam radius and the magnetic field, $R^2B = $ const [53]. (ii) The ratio

of mean transverse energy to the magnetic field $\langle E_\perp \rangle / B$ = const [57]. Electrons are produced in the photocathode with an initial isotropic temperature T_{cath}. The adiabatic expansion leads to decrease in transverse temperature of the electron beam as given by the criterion (ii), yielding the final temperature here

$$k_B T_{\perp,f} = \frac{k_B T_{\perp,i}}{\alpha} = \frac{k_B T_{cath}}{\alpha}. \tag{3.5}$$

Here, k_B is the Boltzmann constant, and $T_{\perp,i}$ and $T_{\perp,f}$ are the initial and final transverse temperatures. For a photocathode, T_{cath} is $\sim$ 25 meV at room temperature and after expansion up to 1 meV can be achieved for $k_B T_{\perp f}$.

The longitudinal acceleration of electrons by U_{cath} results in a reduced longitudinal temperature in the co-moving frame. Kinematic transformation from lab frame to co-moving results in final longitudinal temperature. Since acceleration energy eU_{cath} is significantly larger than the $k_B T_{cath}$, the final longitudinal temperature is

$$k_B T_{\|,f} = \frac{(k_B T_{cath})^2}{2eU_{cath}}. \tag{3.6}$$

It is in the order of 25-100 μeV.

The relation presented above treats the electron beam as an ideal gas of non-interacting free partcles. However, Coulomb interaction among electrons leads to potential energy relaxation in the presence of magnetic field is called longitudinal-longitudinal relaxation (LLR) [58]. Therefore, density of the electron beam plays a major role and final expression for longitudinal temperature is given as

$$k_B T_{\|,f} \approx \frac{(k_B T_{cath})^2}{eU_{cath}} + C \frac{e^2}{4\pi\epsilon_0} n_e^{1/3} \tag{3.7}$$

where C is the dimensionless adiabaticity parameter of the acceleration process. It is $\sim$ 1.9 for fast acceleration [58].

The motion of electrons in presence of a magnetic field B is not free but describes a constrained trajectory around the magnetic field line with a revolution frequency given by the cyclotron frequency

$$\omega_c = \frac{eB}{m_e}. \tag{3.8}$$

Also, due to the large temperature difference between longitudinal and transverse directions, there is another relaxation process called transverse-longitudinal relaxation (TLR), which exchanges heat from the transverse to the longitudinal direction.

However, in a magnetic field TLR can be minimized. Therefore, a certain minimum magnetic field strength must be maintained throughout the electron cooler [59].

In a co-moving frame of reference, the electron velocity distribution is given by an anisotropic Maxwell-Boltzmann distribution,

$$f(\vec{v}_e) = \frac{m_e^{3/2}}{(2\pi k_B)^{3/2} T_{\parallel}^{1/2} T_{\perp}} \exp\left(-\frac{m_e v_{\parallel}^2}{2k_B T_{\parallel}} - \frac{m_e v_{\perp}^2}{2k_B T_{\perp}} \right),$$

(3.9)

where $\vec{v}_{\parallel}$, $\vec{v}_{\perp}$ are the longitudinal and transverse velocity component of the electron velocity $\vec{v}_e$ with respect to the electron beam axis. Due to large difference in $T_{\perp}$ and $T_{\parallel}$, it is also called a flattened electron velocity distribution.

3.4 Merged beam kinematics

A phase-space cooled ion beam has well-defined mean energy E_i. The electron beam energy E_e can be changed by the varying acceleration voltage at the photocathode (U_{cath} in fig. 3.4 shown below). Therefore, the kinematics of electron-ion collisions can be described with relatively simple relations. The relative velocity of electron and ion beam with mean energy $E_e = m_e v_e^2/2$ and $E_i = m_i v_i^2/2$, respectively is given as

$$|\vec{v}| = |\vec{v}_e - \vec{v}_i| = (v_e^2 + v_i^2 - 2v_e v_i \cos\theta)^{\frac{1}{2}}$$

(3.10)

where θ is the angle between electron and ion beams. In the non-relativistic regime, the relative energy in the cente-of-mass frame, E_r is given by

$$E_r = \frac{1}{2}\mu v^2 = \mu\left[\frac{E_e}{m_e} + \frac{E_i}{m_i} - 2\left(\frac{E_e E_i}{m_e m_i} \right)^{\frac{1}{2}} \cos\theta \right]$$

(3.11)

where μ is the reduced mass of the electron-ion system [60]. For $\theta = 0$ and using the relation between ion energy and cooling energy (see eqn. 3.1), a very important relation between the beams can be deduced as

$$E_d = \frac{1}{2}m_e v_d^2 = (\sqrt{E_e} - \sqrt{E_c})^2.$$

(3.12)

Here, E_d is the collision energy between the two beams, commonly denoted as the detuning energy. Fig. 3.3 shows the relation between the lab frame energy of electron beam E_e and the detuning energy [61]. The typical laboratory frame energies of

ion and electron beams at the CSR are about 100 keV and few eV, respectively. As an advantage, the merged beam technique shows the highest resolution at small relative energies. One interesting point is the near-symmteric nature of the detuning energy of faster and slower electrons with respect to ion beam. In a merged-beam experiment E_d is changed by controlling E_e, keeping E_i constant. The rate coefficient or cross section is then shown as a function of the collision energy E_d. The velocity
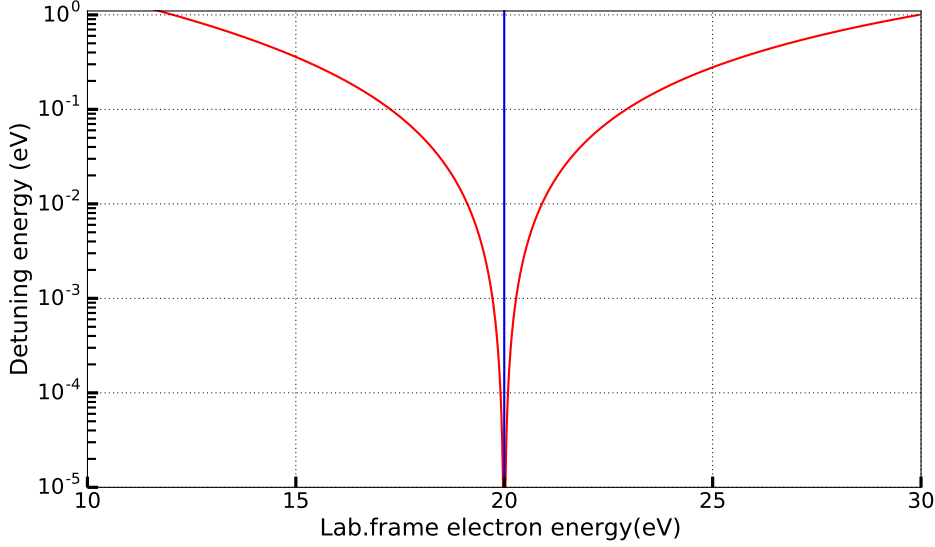

Figure 3.3: Electron-ion collision energy in the center-of-mass frame at 20 eV velocity matched energy (E_c). At small detuning energy high sensitivity can be observed.

distribution function at a given detuned speed v_d from ion's rest frame can be given as

$$f(\vec{v}, v_d; T_\perp, T_\parallel) = \frac{m_e^{3/2}}{(2\pi k_B)^{3/2} T_\parallel^{1/2} T_\perp} \exp\left(-\frac{m_e(v_\parallel - v_d)^2}{2k_B T_\parallel} - \frac{m_e v_\perp^2}{2k_B T_\perp}\right) \quad (3.13)$$

A more detailed investigation of the velocity distribution function in terms of this energy distribution function will be discussed in sec. 4.5.

3.5 Fragmentation scheme at CSR

3.5.1 Experimental arrangement
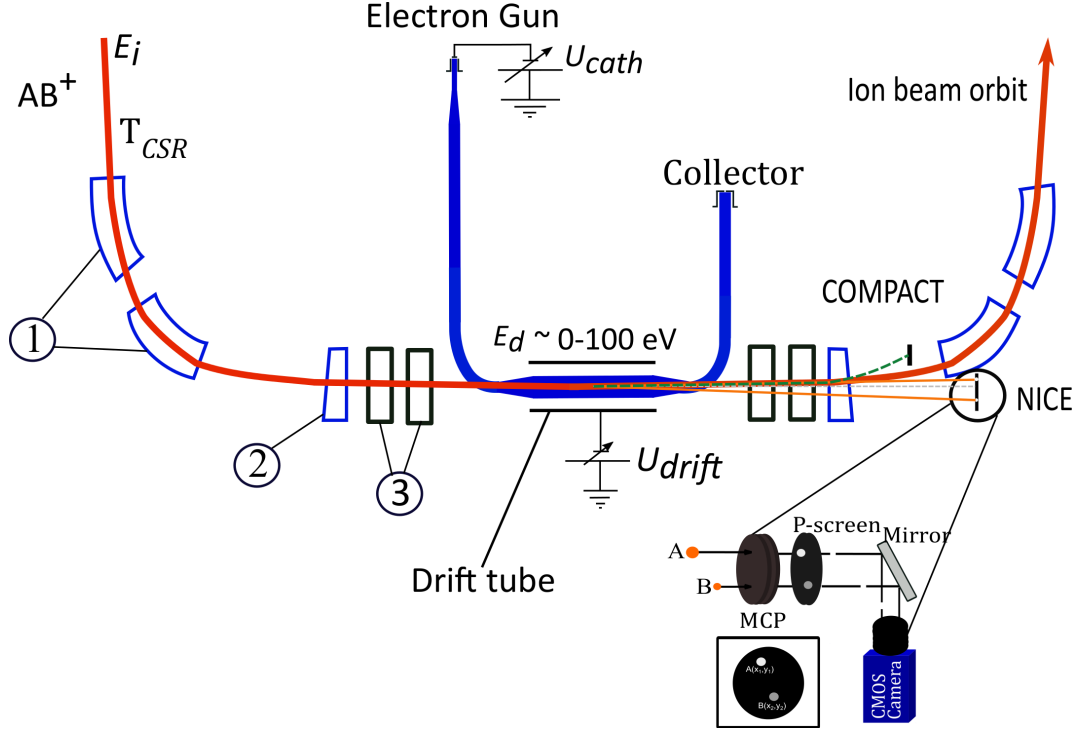
Figure 3.4: Schematic overview of fragmentation measurement in the CSR. Stored ion beam (shown in red) guided by 39° deflector (1), 6° deflector (2), and quadrupole doublet (3). Also, the ion's internal state is coupled to the temperature of the CSR, T_{CSR} by induced absorption and emission (see sec. 2.4). The electron beam (shown in blue) can be chosen to move faster or slower than ion beam by changing detuning energy, E_d either by changing cathode voltage (U_{cath}) or by voltage of drift tubes in the interaction region (U_{drift}). The neutral fragments from reaction with kinetic energy relase (E_{KER}) $\sim$ few eV always emerge in a cone and fly straight to the NICE detector. A zoomed in NICE detector shows an example case AB^+ molecular ion fragmented into A(mass m(A)) and B(mass m(B)). The orientation of fragments is defined with respect to the electron beam axis. On the phosphor screen of the detector, fragments create bright spots and the corresponding positions can be imaged with a CMOS camera. Moreover, in case of a charged fragment (shown in dotted green), a transverse movable fast counting detector (COMPACT) can be used to collect fragment at the deflected position with respect to the ion beam.

Figure 3.4 shows the scheme fragmentation measurements in electron-ion collisions. The electron cooled ion beam is shown in red and expanded electron beam merges from left to right over ~ 1 m. The detailed structure along the length of interaction is presented in sec.4.2.2. Over the interaction length, the electron collision energy can be tuned from meV to several eV (see eqn. 3.12). One of the very important class of fragmentation reactions is the dissociative recombination (DR) where molecular ions undergo dissociation and the reaction products are neutral fragments with excess energy E_{KER} is distributed among them according to the momentum conservation in their center-of-mass frame (see sec. 2.2.1).

To study DR, a neutral particle detector (NICE) has been implemented in the CSR [45]. The particle distance D on the detector plane is given by

$$D = \sqrt{\frac{E_{KER}}{E_i \mu_i}} L \sin\theta. \tag{3.14}$$

where L is the distance between the fragmentation point and detector plane. θ is the angle between molecular orientation and electron beam axis and μ_i is the reduced mass of the molecular ion. Thus, the maximum particle distance on the detector, D_{max} is proportional to $L\sqrt{E_{KER}/E_i}$. The 6^0 deflector seperates the neutral fragments from the stored ion beam and therefore, the closest position from the electron cooler is next to 39^0 deflector. This corresponds to a distance $L_0 = 3.807$ m from the center of the electron cooler.

NICE consist of two multi-channel plates (MCP) in chevron configuration and a phosphor screen serves as the anode [45]. Particle hitting the MCP create an avalanche of electrons which is further accelerated towards the phosphor screen biased at 10 kV. On the phosphor screen it creates a bright spot and their arrival time can be electronically extracted. The spots on the phosphor screen can also be recorded with a high speed CMOS camera outside the CSR cryostat via aluminium mirror situated behind phosphor screen. The active area of the MCP and phosphor screen is ~ 120 mm such that nearly coinicident fragments can be imaged. The distance between fragments on detector plane is proportional to $\sqrt{E_{KER}}$ and orientation of the molecule with respect to the beam axis. Therefore, from projected distance distribution on detector E_{KER} can be calculated which in turn can predict the fragmentation pathways.

The NICE detector can be operated from room temperature to the cryogenic temperature. However, at low temperature resistance of the MCP increases significantly

which in turn saturates the detection capabilities. To overcome this issue, a heating module has been implemented to locally heat the MCPs. MCPs are typically heated up to 40 K and stable and recovered count rate has been observed. In the present experiment HeH$^+$ count rate as function of detuning energy is studied to determine rate coefficient of the DR process. At the stored ion beam energy of $E_i = 250$ keV, the time of flight (TOF) is 1-1.5 μs over the interaction length. At $E_{KER} = 1.55$ eV (see sec. 2.3), both H and He fragments fit the detector with maximum transverse distance of 24 mm and 6 mm, respectively.

In addition, charged products of the fragmentation can also be collected downstream at 3.2 m from the center of electron-ion interaction section with a further detector denoted COMPACT (see fig. 3.4). The detector system consists of a convertor plate and MCP stack with anode to count the hits during fragmentation. The working principle is based on the production of secondary electrons when a particle hit the bent aluminium convertor plate. These secondary electrons are further accelerated towards a small MCP where the particle event can be detected with nearly 100 percent efficiency. The detector can also be moved across the beam line of the CSR via a translation stage and hence allows to detect fragments based on the charged to mass ratio [47, 46].

3.5.2 Rate coefficient determination

The rate of interaction in an electron-ion collision experiment within an interaction volume V can be determined with the spatial electron density $n_e(\vec{r})$, the spatial ion density $n_i(\vec{r})$, the relative velocity between electron and ion $\vec{v}$, and the cross section $\sigma(\vec{v})$, and also the velocity distribution $\hat{f}(\vec{v}, v_d; T_\perp, T_\parallel, X, U_{sc}, U_{dr})$ of the collision velocity $\vec{v}$ at a given detuning velocity. Then, the rate R is given by,

$$R(v_d) = \int_V \int_v n_e(\vec{r})n_i(\vec{r})\sigma(\vec{v})v\hat{f}(\vec{v}, v_d; T_\perp, T_\parallel, X, U_{sc}, U_{dr})d^3v d^3r \qquad (3.15)$$

where X, U_{sc} and U_{dr} in $\hat{f}(\vec{v})$ (in short) are the overlap geometry of the merged beam, the space charge potential of the electron beam, and drift tube potential, respectively. Details of these terms contributions are discussed in chapter 4.

In a magnetically guided electron beam, the spatial electron density $n_e(\vec{r})$ is uniform along the whole interaction length, and the ion beam after phase-space cooling is well confined within the electron beam. For cylindrically shaped electron and ion beams, the volume can be integrated in terms of transverse and axial part as $dr_\perp$

and dz, respectively. The electron density is simply used as n_e for the complete interaction region and, hence, n_e is taken out of the integral. The ion density in the interaction region is given by the following relation:

$$n_i(\vec{r}) = \lambda_{ion} f(\vec{r}_\perp) \quad \text{with } \lambda_{ion} = \frac{N_i}{C_0} \text{ and } \int_{-\infty}^{\infty} \int_{-\infty}^{\infty} f(\vec{r}_\perp) d^2 r_\perp = 1 \qquad (3.16)$$

where λ_{ion} is the linear ion density with N_i and C_0 are the number of stored ions and circumference of the CSR, respectively. $f(r_\perp)$ represents the transverse distribution of very narrow FWHM ion beam and due to confinement within the electron beam it is assumed to be normalized. Therefore, axial part still remains in the integral.

The velocity distribution function is a 3-dimensional function, where transverse components are due to the thermal energy spread of the electron beam (see sec. 3.3.2). The function $\hat{f}(\vec{v}, v_d; T_\perp, T_\parallel, X, U_{sc}, U_{dr})$ is defined here for a general scenario to motivate the realistic collision conditions in our merged beam set up. The electron beam approaches at a certain non-zero angle before it becomes parallel to the ion beam. In addition, if drift tube in the interaction region is used for electron beam energy deceleration purpose, an additional position dependent velocity comes into effect. To account for such a case, the electron beam kinetic energy is described by a position dependent function $E_{kin}(z)$.

Therefore, relative velocity $\vec{v}$ between electron and ion is qualitatively given by,

$$\vec{v} = \begin{pmatrix} 0 \\ 0 \\ v_d \end{pmatrix} + \vec{\delta}(v_{th}, X, U_{sc}, U_{dr}) \qquad (3.17)$$

where v_d is the experimentally controlled and scanned average collision velocity between beams and $\vec{\delta}$ is the additional contribution for a given collision event due to thermal energy spread v_{th}, X accounts for increase due to the angle between electron and ion and U_{dr} is due to the drift tube operation (if used). Thus, integration along z incorporates the position dependent nature of electron-ion collision velocity and after switching position of integrals in eqn. 3.15 rate is given as,

$$R(v_d) = \frac{N_i}{C_0} n_e \int_v \sigma(\vec{v}) v_e \Big(\int_{l_{int}} \hat{f}(\vec{v}, v_d; T_\perp, T_\parallel, X, U_{sc}, U_{dr}) dz \Big) d^3 v \qquad (3.18)$$

where l_{int} is the full interaction length of the electron-ion merged beam set up. The rate can also be written as

$$R(v_d) = \frac{N_i}{C_0} n_e l_{int} \alpha_{mb}(v_d) \qquad (3.19)$$

where $\alpha_{mb}(v_d)$ is the convolution of the product of $v\sigma(\vec{v})$ over the velocity distribution and averaged over the complete interaction length,

$$\alpha_{mb}(v_d) = \langle \sigma v \rangle = \int_v \sigma(\vec{v})v\left(\frac{1}{l_{int}}\int_{l_{int}} \hat{f}(\vec{v},v_d;T_\perp,T_\parallel,X,U_{sc},U_{dr})dz\right)d^3v \quad (3.20)$$

Since the molecules are randomly oriented, the directional nature in the cross section can be neglected and thus, $\sigma(\vec{v}) = \sigma(v)$. Also, the results are usually considered through an energy-dependent convolution function. For this purpose, rate is described as

$$R(E_d) = \frac{N_i}{C_0}n_e l_{int}\alpha_{mb}(E_d) \quad (3.21)$$

setting $v_d = \sqrt{2E_d/m_e}$ and

$$\alpha_{mb}(E_d) = \int \sigma(E)\sqrt{2E/m_e}f_{mb}(E,E_d;T_\perp,T_\parallel,X,U_{sc},U_{dr})dE \quad (3.22)$$

where the energy distribution function, f_{mb} is obtained by integrating $\hat{f}$ over the sphere in velocity space at $v = \sqrt{2E/m_e}$ and $(mv^2/2)$ lying in the range $E \pm \triangle E/2$.

$$f_{mb}(E,E_d;T_\perp,T_\parallel,X,U_{sc},U_{dr}) = \frac{1}{l_{int}\triangle E}\int_{E\pm\triangle E}\int_{l_{int}} \hat{f}(\vec{v},v_d;T_\perp,T_\parallel,X,U_{sc},U_{dr})dzd^3v$$

$$(3.23)$$

The energy dependent convolution function will be presented below.

For a narrow width rate coefficient is,

$$\sigma(E)\sqrt{2E/m_e} = \hat{\alpha}_0\delta(E - E_{res}) \quad (3.24)$$

where $\hat{\alpha}_0$ is the energy integral of the rate coefficient. The convolved rate coefficient in eqn. 3.21 will then follows from eqn. 3.22 as

$$\alpha_{mb}(E_d) = \hat{\alpha}_0 f_{mb}(E_{res},E_d;T_\perp,T_\parallel,X,U_{sc},U_{dr}) \quad (3.25)$$

As the resonance is sampled mainly by the nearly monoenergetic electrons in the straight part of the interaction region, $\alpha_{mb}(E_d)$ peaks near $E_d = E_{res}$ and decays to very small values outside the interval $E_{res} - \triangle E$, $E_{res} + \triangle E$.

However, the integral

$$\int_{E_{res}-\triangle E}^{E_{res}+\triangle E} \alpha_{mb}(E_d)dE_d = \hat{\alpha}_0 \int_{E_{res}-\triangle E}^{E_{res}+\triangle E} f_{mb}(E_{res},E_d;T_\perp,T_\parallel,X,U_{sc},U_{dr})dE_d \quad (3.26)$$

over the experimental peak will be less than $\hat{\alpha}_0$, as the complete l_{int} also includes the merging regions (see chapter 4).

However, an equivalent description to eqn. 3.21 is

$$R(E_d) = \frac{N_i}{C_0} n_e l_{eff} \alpha_m(E_d) \tag{3.27}$$

with $\alpha_m(E_d) = (l_{int}/l_{eff})\alpha_{mb}(E_d)$. When l_{eff} is chosen as

$$l_{eff} = l_{int} \int_{E_{res}-\triangle E}^{E_{res}+\triangle E} f_{mb}(E_{res}, E_d; T_\perp, T_\parallel, X, U_{sc}, U_{dr})dE_d \tag{3.28}$$

then the integrated measured rate coefficient $\alpha_m(E_d)$ in the range of $E_{res} \pm \triangle E$ represents the energy integrated rate coefficient $\hat{\alpha}_0$. Rate coeffcients $\alpha_m(E_d)$ will be largely independent of the measuring configuration if l_{eff} is properly chosen for each configuration and the considered energy range.

From measured rates $R(E_d)$ the rate coefficients are extracted using

$$\alpha_{mb} = \frac{R(E_d)}{n_e N_i l_{int}/C_0} \tag{3.29}$$

and

$$\alpha_m = \frac{R(E_d)}{n_e N_i l_{eff}/C_0} \tag{3.30}$$

For the present discussion, detector efficiency is assumed to be 1. In chapter 5, detector efficiency is considered for the case of DR.

Energy resolution

In a phase space cooled ion and electron beams collision, the energy resolution is mainly determined by the longitudinal and transverse temperatures of the electron beam for flattend energy distribution. The width (FWHM) of a very narrow resonance of negligible width is given by the following relation [62]:

$$\triangle E \approx \sqrt{(k_B T_\perp \ln 2)^2 + 16 k_B T_\parallel E_d \ln 2} \tag{3.31}$$

Fig. 3.5 shows the energy spread as a function of detuning energy. It can be clearly seen that in the energy range below $k_B T_\perp$, total width is limited by transverse energy spread of the beam. And, at higher E_d, width is dominated by the longitudinal
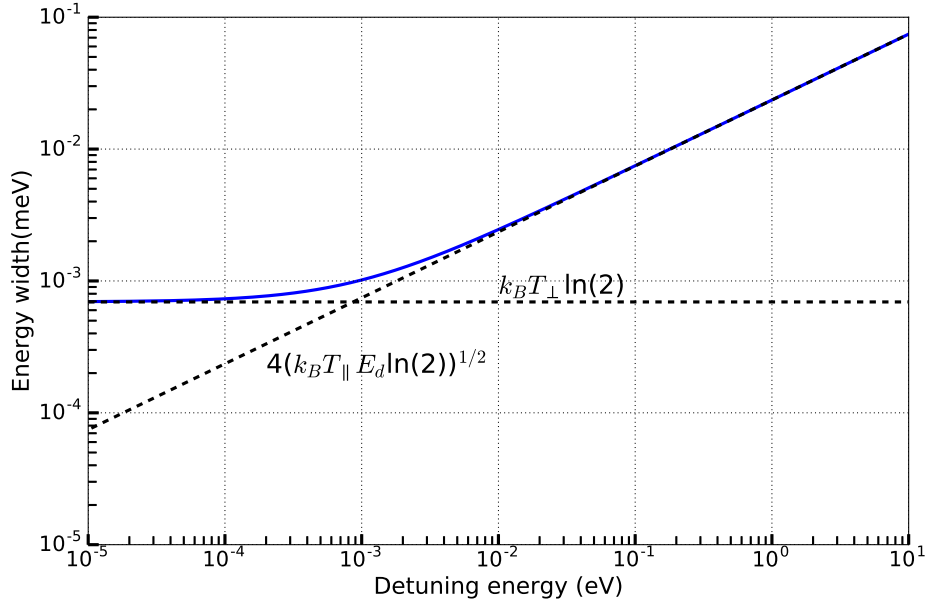
Figure 3.5: Expected energy spread in the merged electron-ion collision experiment as function of detuning energy. The electron beam thermal energy spread are $k_B T_\parallel = 50$ μeV and $k_B T_\perp = 1$ meV. The blue curve is the total FWHM and dotted lines show the individual contribution to the energy spread.

temperature. Also, the relative width $\triangle E / E_d$ reduces to a small value. Lastly, the energy where the contribution to the width due to the transverse temperature is equal to that of the longitudinal one is

$$E_{eqs} = \frac{\ln 2 (k_B T_\perp)^2}{16 k_B T_\parallel} \tag{3.32}$$

For the present case $E_{eqs} = 0.87$ meV. In sec. 4.6, model rate coefficient shape for a delta resonance will be discussed with realistic energy distribution.

3.6 Simulation software

In the next chapter, the electron cooler model is presented. Here we already introduce the used software and its basic working principle. The electron cooler has been simulated in the field analysis program TOSCA from Opera-3d [63]. In Tosca, elec-

tric or magnetic field of any given geometry is calculated on fine mesh in space by solving Maxwell's equation. In the electron cooler the magnetic fields from several coils were superimposed and scaled such that to obtain minimum transverse offset in position.

In addition, G4beamline a particle tracking software is also used escpecially in the case of the drift tube operations of the electron cooler model. It is a command based program based on *Geant*4 [64]. For this purpose, the magnetic and electric field tables of all magnetic coils and drift tube were imported from TOSCA electron cooler model. And, similar to TOSCA single electron can also be tracked in presence of electric and magnetic fields.

4 Modelling the conditions of electron collision measurements with low energy merged beams

In this chapter, we establish the characteristic properties of the electron beam trajectory in a field analysis program. The influence of the merging geometry in the electron-ion merged beams set up of the CSR is studied in detail. Later, the role of space charge of the electron beam under realistic experimental beamline geometry in the interaction section is calculated. At low cooling energy, the electron cooler can make use of drift tubes to decelerate electrons in the interaction region to reach velocity matched condition and overcome the space charge limit of the electron gun at a given electron energy.

Then, the results of the electron and ion beams collision energy distribution as function of geometry of the merged beams set up, space charge of the beam, and the drift tube is presented. The obtained energy distributions are also used to simulate model merged beams rate coefficients for typical cross section in recombination experiments.

4.1 Challenges and requirements

The CSR electron cooler is the first low energy electron beam device operated in a cryogenic electrostatic ion storage ring. In summer 2017 electron cooler has been successfully commisioned and operated to achieve the longitudinal phase space cooling of F^{6+} ions in the CSR [65, 66]. As discussed in sec. 3.2, to enable the electron beam to achieve phase space cooling of ions and later act as target for recombination experiments, certain conditions need to be fulfilled. In this section, we will explain the conditions and challenges.

The CSR electron cooler is designed to have beam energies ranging from 1eV to 1000 eV. The density of electrons in the beam is proportional to beam current and

it scales with three-halves power law of extraction voltage (see sec. 3.3). However, at low energy electron cooler should have sufficient density to phase space cool ions in time scales smaller than the ion-beam lifetime. This feasibility of low-energy beam with sufficient density has been explored and established in previous work by Shornikov et al. [59, 67]. The overall geometry is determined by a guiding magnetic field pointing in the electron beam direction and shown in fig. 4.1. The strength of the guiding magnetic field should be sufficient to suppress the blow up due to Coulomb repulsion of the electrons. And, a high magnetic field also reduces the TLR effect, which is favorable for faster cooling as discussed in sec. 3.3.2. Moreover, high magnetic field can affect the ion beam trajectory in the merging or demerging section as transverse component of B-field can deflect the ions. Shornikov has also shown that the strongest criterion on magnetic field strength is the fulfillment of adiabaticity criterion especially along the curved track of the toroidal coils [59]. The maximum field strength required is for 1 keV electron energy is 215 G. Therefore, the nominal B-field used in the toroidal coils for all calculation is 250 G.

The CSR electron cooler deviates from the conventional U-shaped or S-shaped design for the merging and demerging of ion and electron beams as in high energy electron cooler e.g. TSR ion storage ring. The low energy ion beam in the CSR electron cooler, e.g. 20 keV protons feel non-linear (position dependent) vertical deflection by horizontal component of the toroidal field if used for merging and it cannot be corrected with dipole compensation coils [68]. Fadil et al. [68] calculated and proposed the toroid free merging design and Shornikov developed it further to fit in the CSR cryostat [59].

4.2 Electron cooler model

Electron cooler design and simulation of the entire beamline was conceived and performed in previous works [59, 48]. The final beamline is the result of several iterations of mechanical compatibility of magnets and cryogenic requirements. The quality of electron beam was simulated for each iteration step. An ultra-high vacuum of the order of 10^{-11} mbar in the room temperature gun section is important for long operation of photoelectron gun. Here, a brief introduction of magnetic components and trajectory of electron will be discussed. The room temperature part, gun and collector sections have been simulated separately and adiabaticity condition of magnetic fields was fulfilled [48]. The presented electron cooler beamline for elec-
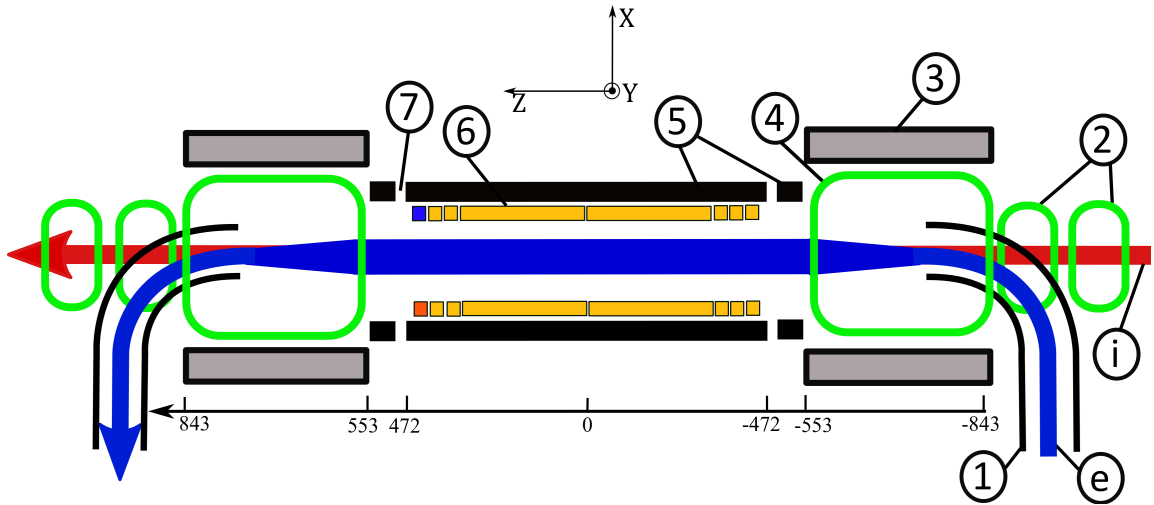
Figure 4.1: Top view of the magnetic elements and of the drift tubes in the cyrogenic part of the electron cooler. For a complete view of the electron cooler see fig. 3.2. The electron beam (e) enters from left in toroidal magnet (1) (linear+ 90º+30º). Compensator dipole coil (2) placed before and after merging and demerging section respectively. Box magnet (3) and merging vertical (MV) (4) dipole magnets (4 coils) forms merging section. Main solenoid and two short solenoids (5) creates longitudinal B-field in interaction section. Set of drift tubes (6) defines kinetic energy of electron beam in the interaction section if used. The position of coils along longitudinal axis of the electron beam is also shown.

tron tracking consist of merging, interaction and demerging sections. The cryogenic linear toroid is extended upto room temperature cathode position in order to mimic conditions of a realistic beamline and minimize fringe fields. In a similar manner, the collector side linear toroid is also extended up to the main cup position [48].

4.2.1 Magnetic field calculations

TOSCA is the electromagnetic field analysis program of OPERA-3D vector fields (see sec. 3.6) [63]. It has been used to model the magnetic and electric components of the electron cooler and to define the electron trajectory. The electric components are mainly drift tubes and shall be discussed later in this chapter. Fig. 4.1 shows the cryogenic magnetic elements and their corresponding positions along the longitudinal axis. The coordinate system for the TOSCA electron cooler model is same as the

CSR i.e. z is the longitudinal axis, x and y are transverse horizontal and vertical axes, respectively. Also, the coordinate system is left handed but in agreement with the convention of accelerator Physics for circular motion z is similar to s [69]. The electron starts 140 mm vertically above and guided perpendicular (along $+$ x-axis) to the ion beam orbit of the CSR. The 90^0 toroidal magnet(1) in the CSR cryostat bends the electron beam horizontally and making it parallel to the closed ion beam orbit. Next, 30^0 toroidal magnetic field bends the beam downward ($|B_y|$ $>$0). Following 30^0 toroid is the merging region where electron beam merges with ion beam. The superposition of longitudinal magnetic field produced from solenoidal box magnet(3) over 290 mm merging section and vertical downward field from a set of four race-track coils, the so-called merging vertical(4) (MV). The MV coils are placed symmetrically with respect to the ion beam and two inner coils are tilted by 17^0 clockwise, and counterclockwise with respect to ion beam, to allow ion beam vacuum flange pass through it (see fig. 3.2).

After merging region, electron beam remain merged with ion beam in the interaction region. It consists of 944 mm long main solenoid (MS), and two short solenoids of length 47 mm each, placed before and after main solenoid with a gap of 34 mm to allow a relatively long straight section with nearly uniform solenoid field (see fig. 4.1). The gaps between MS and short solenoids serve the purpose of positioning rotational feedthrough of wire scrapers. The position of gaps is particularly advantageous as electron and ion beams are already collinear in this region and hence, wire scrapers can be used to determine the beam overlap [70]. Followed by this, similar to merging region, a superposition magnetic field of racetrack coils and solenoidal box magnet moves the electron vertically upward and demerges. In addition, there are two pairs of compensator coils(2) to correct ion beam trajectory from the merging field. These coils are placed before merging and after demerging sections, respectively. The pair of outer coils deflects ion beam into same direction as the MV coils to create a position shift. The pair of inner coils bend ion into the opposite direction. These coils are not in the model for electron beam as shown here.

Fig 4.2 shows the simulated transverse magnetic fields along the longitudinal axis of the electron beam. B_x shown in red, starts to decrease in amplitude as electron beam bends in 90^0 toroid and subsequently becomes 0 when $\vec{B}$ points parallel to z. It remains negligible since electron moves in (y, z) plane. Similarly, B_y is magnetic field component in vertical direction (y). It modulus starts to increase after 90^0 toroid
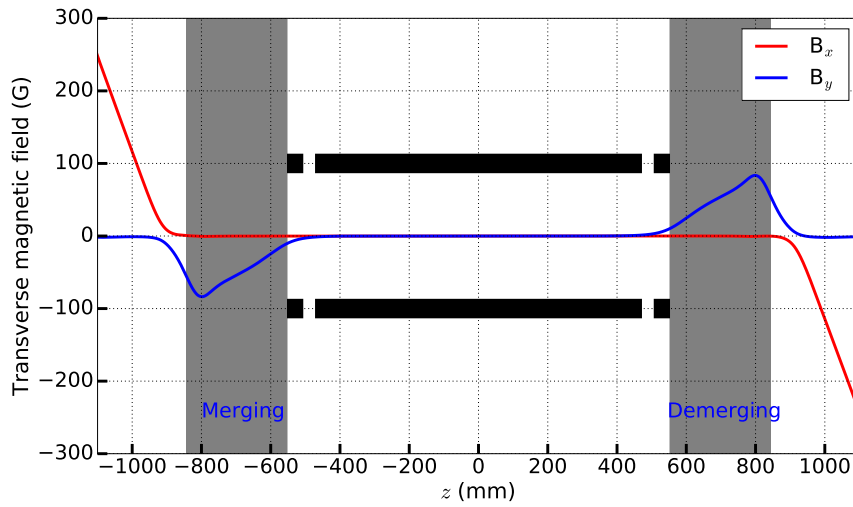
Figure 4.2: Illustration of simulated transverse magnetic field along x and y directions. The bold black lines represent the position of main solenoid and two short solenoids (see fig. 4.1). The grey shaded area correspond to merging and demerging regions.
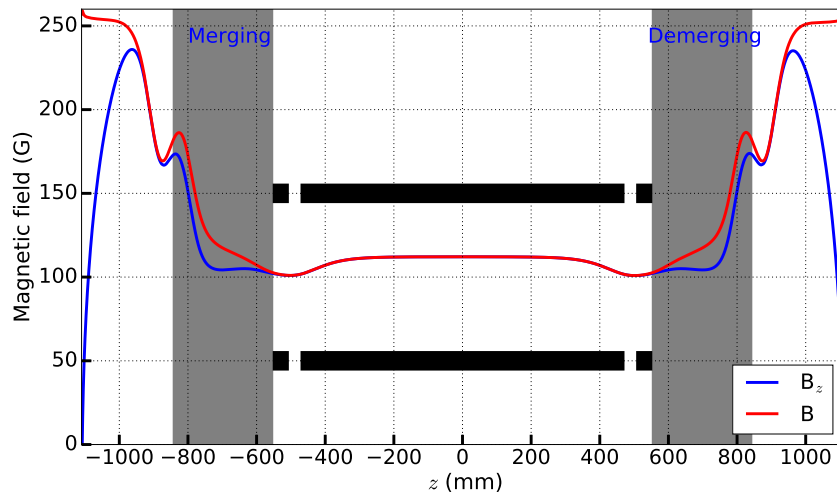

Figure 4.3: Illustration of simulated total and longitudinal magnetic field along z. The bold black lines represents the position of MS and two short solenoids. The grey shaded area correspond to merging and demerging regions.

due to merging verticals coils. The origin $z = 0$ is the center of main solenoid and the electron cooler. The transverse field componenets remain small in the interaction region, but it is taken into account in the calculations.

Fig. 4.3 shows the simulated total and longitudinal magnetic field along the electron beam axis. The initial B_z starts to increase in the 90^0 toroid. The adiabaticity criterion demands a strong magnetic field in the 90^0 degree toroid, but a smaller magnetic field can be chosen for the linear interaction region. The field in the interaction region is, hence reduced to ~ 110 G. In remaining part, longitudinal field strength is nearly uniform with small depression in the field strength due to the 34 mm gaps on both sides of main solenoid. The nearly uniform field strength defines a constant beam size of the electron beam after second magnetic expansion (α_2) (see sec. 3.3).

4.2.2 Electron trajectory and toroidal drifts
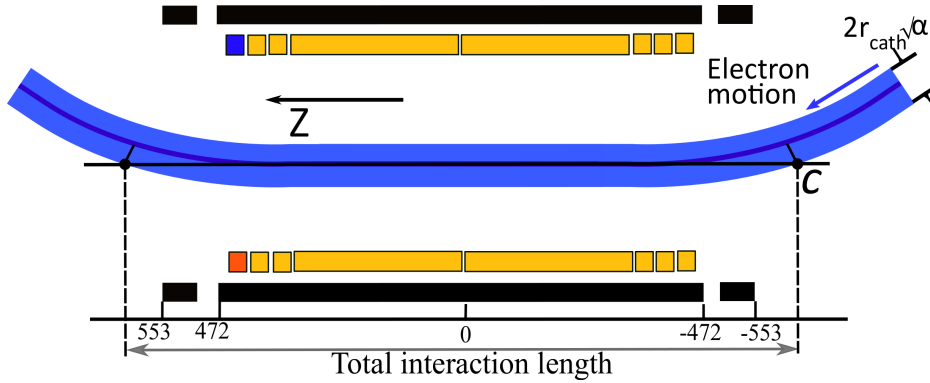
Figure 4.4: Illustration of merged electron-ion beams in the interaction section of the electron cooler. The phase space cooled ion beam (shown in black) and magnetically expanded electron beam (blue) overlap defines the total interaction length. The purple line is the center of the electron beam. The main solenoid and two short solenoids are also shown. The position of solenoids are also shown with respect to center of main solenoid.

The ion-electron beams interaction length depends on cross section of the electron beam. For a magnetic expansion α, the size of electron beam is the product of cathode size, r_{cath} and $\sqrt{\alpha}$ (see sec. 3.3). In principle, size of phase space cooled ion beam is very small compared to the electron beam and therefore can be approximated as

straight line. In this way, the point of intersection of ion and electron beams while merging and demerging can be defined and which in turn gives the total interaction length. Fig. 4.4 shows the merged electron-ion beams and total interaction length can be seen as the point of intersection C of the electron boundary with the ion beam assumed to be much smaller.

The interaction length and overlap between beams is optimum if ion beam lies at the center of the electron beam. In fragmentation experiments, the electron beam energy is changed over a certain range. Therefore, there should not be any offset in position of the electron beam as the ion beam position is fixed. However, in 90^0
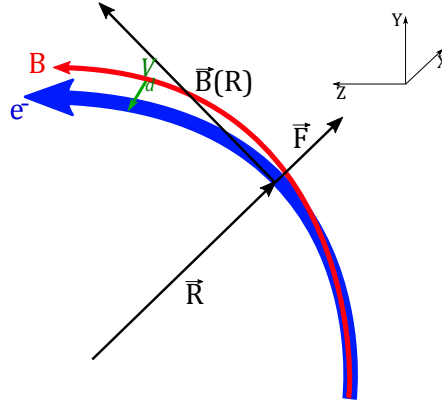
Figure 4.5: Drift of electron motion from the toroidal (x, z) plane. The red arc is the magnetic field along the toroid and blue is the downward shifted electron trajectory due the drift velocity, v_d (shown in green) along negative y.

toroid magnet (see fig. 4.1), the magnetic field $\vec{B}$ is oriented along the axis of toroid as shown in fig. 4.5. The electron while moving along axis experiences a centrifugal force, $\vec{F}$ in its rest frame as:

$$\vec{F} = \frac{m_e v_\parallel^2}{R} \frac{\vec{R}}{R} \tag{4.1}$$

where m_e is mass of electron and $v_\parallel$ is the electron velocity parallel to $\vec{B}(R)$. This force causes curvature drift or toroidal drift with velocity

$$\vec{v}_d = \frac{\vec{F} \times \vec{B}}{eB^2} \tag{4.2}$$

and then

$$\vec{v}_d = \frac{m_e v_\parallel^2}{e} \frac{\vec{R} \times \vec{B}}{R^2 B^2} \tag{4.3}$$

42

The direction of drift velocity, $\vec{v}_d$ is normal to the plane of toroid in negative y direction due to electron's charge. It is proportional to the energy of the electron beam and give rise to downward offset in the electron beam position in the interaction region which in turn can lead to complete loss of the overlap between the beams.

Table 4.1: Toroidal drift compensating magnetic field at different electron energy

Energy (eV)	$\mathbf{B}_\perp$ (G)
1	0.168
20	0.75
100	1.69
1000	5.33

To compensate this offset, 90^0 degree toroid in the electron cooler model is equipped with a pair of steerer coils one above and one below the plane of electron beam and it is always used for our electron trajectory calculations. The steerer coils produce a weak vertical B-field, $B_\perp = m_e v_\parallel / eR$ to compensate the offset. Table 4.1 shows the typical B-field needed to balance the offset. Therefore, the electron beam trajectory after toroidal drift compensation is identical for 1 - 1000 eV.

4.2.3 Trajectory results and beam overlap

To quantify above scenario, TOSCA electron cooler model was used to track the electron beam along the complete trajectory. For this purpose, a single electron is launched from center of photocathode with 1 eV kinetic energy in longitudinal direction and tracked at step length of 0.1 mm over the entire trajectory up to the collector side. Since electron follows the magnetic field lines of the center of solenoid, it does not feel any effect of magnetic expansion (factor $\sqrt{\alpha}$) and remains at the center of guiding field throughout (see purple line in fig. 4.4). For this central electron, the coordinates are $x_0(z)$ and $y_0(z)$ shown in fig.4.6.

The x_0 position is very small in the interaction region and can be neglected. Consequently, only $y_0(z)$ is used to describe electron's transverse position as function of longitudinal position z. From this, the coordinate z_c of the intersection point $\boldsymbol{C}$ can be determined (see fig. 4.4). Neglecting x_0, the condition for the cutting point C is eqn. 4.5 and the cutting point C lies at the z coordinate of eqn. 4.4.

$$z_c = z_0 + y_0(z_0)\frac{dy_0}{dz}\bigg|_{z_0} \tag{4.4}$$
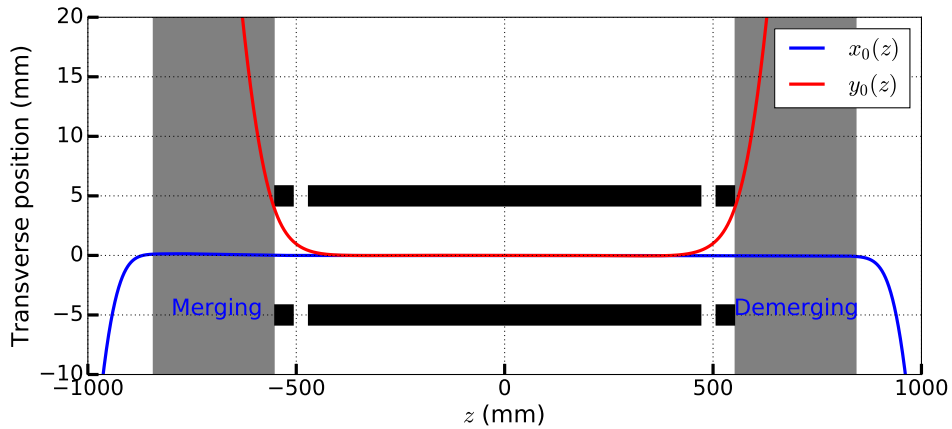
Figure 4.6: Illustration of electron's x_0 and y_0 positions in the interaction region. The x_0 remains very small after 90^0 toroid while y_0 remains finite in the interaction region. The bold black lines represent the position of MS and short solenoid. The grey shaded area correspond to merging and demerging regions.

$$y_0(z)\sqrt{1 + \left(\frac{dy_0}{dz}\bigg|_{z_0}\right)^2} - r_{beam} = 0 \tag{4.5}$$

The overall length of interaction is then $l_{int} = 2z_c$.

Fig. 4.7 shows the symmetric half of the electron trajectory in the interaction region. The black line at $y = 0$ is the ion beam in CSR orbit and blue curve is electron path $y_0(z)$. Up to ~ 400 mm electron-ion beams are collinear and remaining electron trajectory is bent. The overlap limit z_c and the coordinates of y_0, z_0 of the beam center at these points for the electron beam at different magnetic expansions are presented in the table 4.2.

Table 4.2: Electron beam overlap limits on different magnetic expansion factor.

α	y_0 (mm)	z_0 (mm)	z_c (mm)
10	4.71	560.24	560.78
20	6.63	574.2	575.24
30	8.08	582.8	584.24
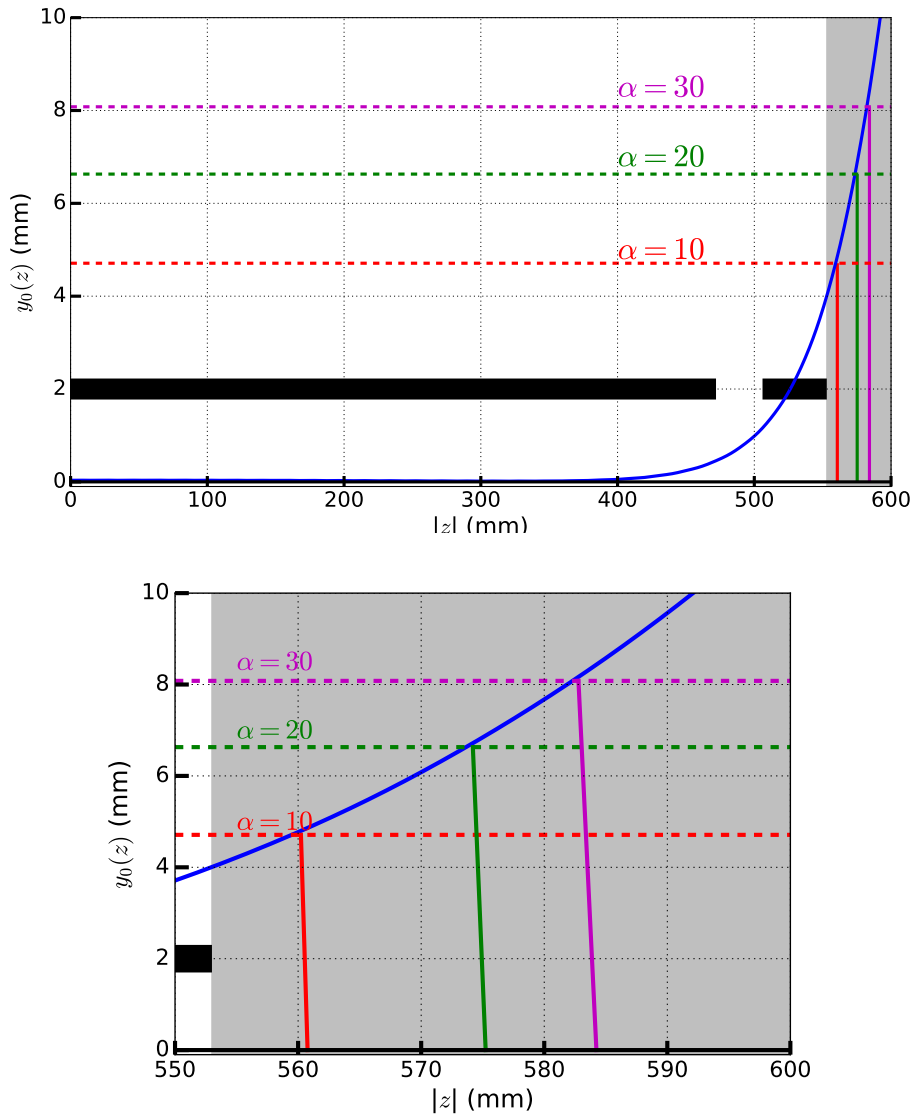
Figure 4.7: Illustration of electron trajectory in the interaction region (shown in blue). Red, green and magenta horizontal dashed lines correspond to $y_0(z_0)$ and cuts of these lines with $y = 0$ are overlap limits z_c for expansion factor $\alpha = 10$, 20 and 30, respectively. The second figure is the zoomed in part to shows the beam limits more clearly. The lengths of the coloured solid lines are the radius, r_{beam} at a given expansion α. The bold black lines indicate the main solenoid and the short solenoid. The grey shaded area correspond to merging region of fig. 4.2

4.2.4 Collision energy from overlap geometry

In sec. 4.2.3, we have seen that the trajectory of the electron beam is bend in the overlap geometry. For given geometry, the transverse angle is defined as:

$$\tan\theta = \frac{|\mathrm{B}_\perp|}{\mathrm{B}_\parallel} \quad \text{and} \quad \theta = \arctan\left(\frac{|\mathrm{B}_\perp|}{\mathrm{B}_\parallel}\right) \tag{4.6}$$

where $\mathrm{B}_\perp = \mathrm{B}_y$ is the transverse magnetic field component and $\mathrm{B}_\parallel = \mathrm{B}_z$ is longitudinal field (see sec. 4.2).
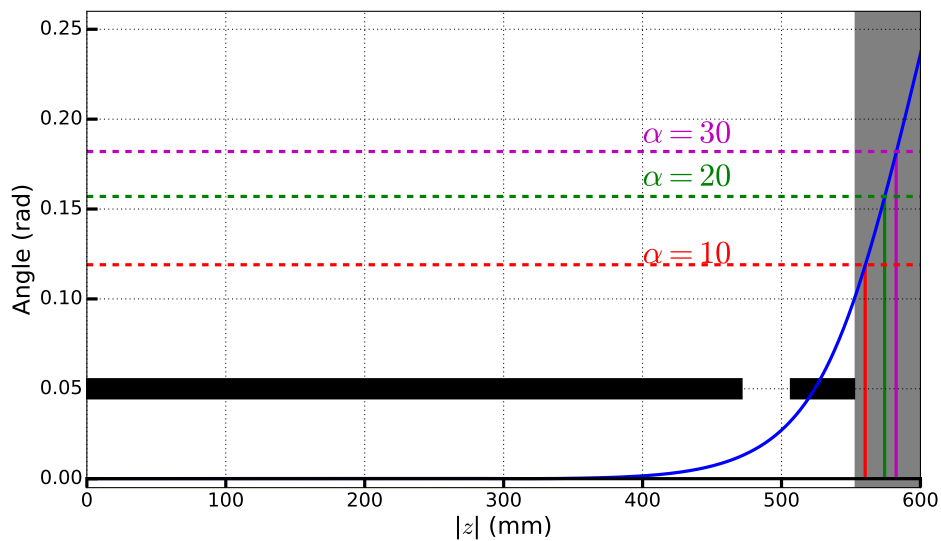
Figure 4.8: Illustration of transverse angle in the interaction region. Red, green and magenta lines show limit for expansion factor $\alpha = 10$, 20 and 30, respectively. The bold black lines represents the position of MS and short solenoid. The grey shaded area correspond to merging region.

In Fig. 4.8 transverse angle in the interaction region is shown. The limit on θ for a given α is defined based on respective $y_0(z_0)$ position. In the merging and demerging region transverse angle can rise up to 0.119, 0.157 and 0.182 radian for $\alpha = 10$, 20 and 30, respectively.

In addition, with known interaction length l_{int}, transverse angle of electron beam at a given magnetic expansion and straight ion beam, their collision energy in the center-of-mass frame can be calculated (see eqn. 3.11). It is the most important information of this merged beams set up, as it tells us position dependent collision
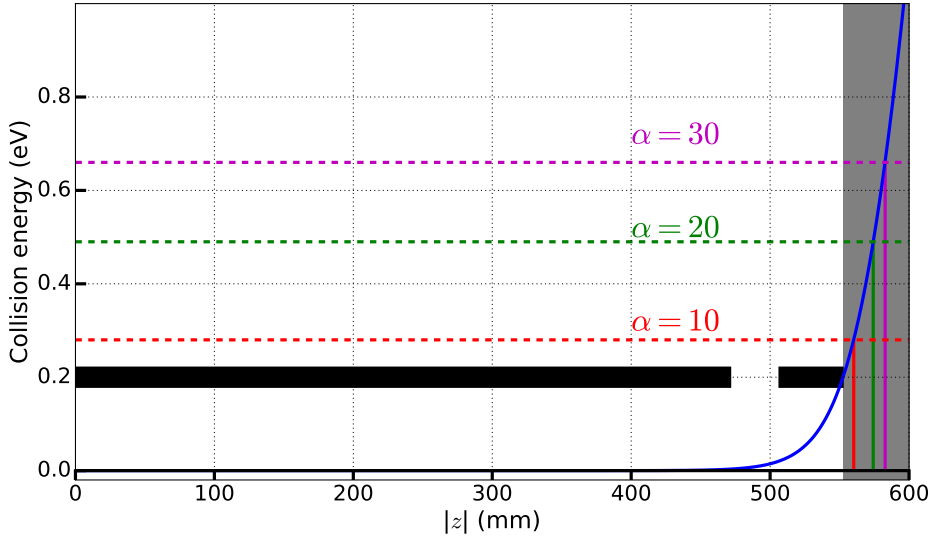
Figure 4.9: Collision energy as function of position in the interaction region. Red, green and grey lines show limits for expansion factor $\alpha = 10$, 20 and 30 respectively. The bold black lines represents the position of MS and short solenoid. The grey shaded area correspond to merging region.

energy for velocity matched beams. Fig. 4.9 shows collision energy from overlap geometry of the merged beams set up at an example velocity matched electron beam energy, $E_c = 20$ eV. The collision energy is nearly zero up to 500 mm but in the bending region, it can rise up to 0.67 eV, 0.47 eV and 0.26 eV for expansion factor 30, 20 and 10, respectively.

Table 4.3: Summary of the electron-ion trajectory of the merged beams set up at 20 eV velocity matched energy (E_c).

α	r_{beam} (mm)	$l_{int}/2$ (mm)	θ_{max} (Radian)	*Maximum energy* (eV)
10	4.74	560.78	0.119	0.26
20	6.70	575.24	0.157	0.47
30	8.21	584.24	0.182	0.67

Finally, we can summarise the obtained results of the merged beams set up at magnetic expansion, $\alpha = 10$, 20 and 30, respectively. Table 4.3 consist of interaction length, transverse angle and collision energy for a given expansion of electron beam.

4.3 Space charge of the electron beam

Up to now characteristic features of the electron beam has been described with a single electron. However, to define the contribution of interaction among electrons we have to include finite size of the beam, r_{beam} and its density n_e. The magnetically confined electron beam experiences the space charge potential U_{sc} due to Coulomb repulsion. As a consequence, electrons at the center of the beam get screened and do not experience the applied acceleration potential U_{cath}. The electron energy in the center of beam in such a case is given by,

$$E_e = -eU_{cath} - eU_{sc}(n_e) \tag{4.7}$$

Since the energy at center of the beam should match ion energy for efficient phase space cooling and therefore, space charge potential U_{sc} should be known at a given density. For a cylindrical electron beam of uniform density, n_e inside a grounded cylindrical tube, U_{sc} is given by the following relation:

$$U_{sc} = \begin{cases} \frac{n_e e r_{beam}^2}{4\epsilon_0}\left(1 + 2\ln\left(\frac{R_0}{r_{beam}}\right) - \left(\frac{r}{r_{beam}}\right)^2\right), & (r < r_{beam}); \\ \frac{n_e e r_{beam}^2}{4\epsilon_0}\left(2\ln\left(\frac{R_0}{r_{beam}}\right)\right), & (r > r_{beam}) \end{cases} \tag{4.8}$$

where r_{beam} is the radius of the electron beam, R_0 is the radius of electron cooler beam tube, and r is position in radial direction.

The potential at the center of the beam along z axis remains constant in a uniform cross section region of the beam tube. However, in the interaction section only drift tube electrodes have uniform cross section and adjacent regions have very non-uniform experimental chamber cross section. Fig. 4.10 shows the CAD model of the symmetric half of the interaction region. From the center of electron cooler, drift tube electrodes have uniform cross section of 100 mm and next region consist of the cable housing for electrodes and scraper has non-uniform cross sections. Also, a bellow decoupling merging and interaction section and only small section of beamline has constant 150 mm cross section. For a test case of $n_e = 6.65 \times 10^5$ cm^{-3} at R_0 of 50 mm and 75 mm, U_{sc} is 0.68 V and 0.78 V, respectively at the center for electron beam of magnetic expansion 20. However, it cannot describe the variation of U_{sc} along the electron beam axis in non-uniform cross section region.

To solve this problem, we used Poisson solver of the SIMION 8.1 ion optics package [71]. We selected half of the symmetric interaction region as it contains the relevent non-uniform cross section region and also computationaly suitable. The symmetric
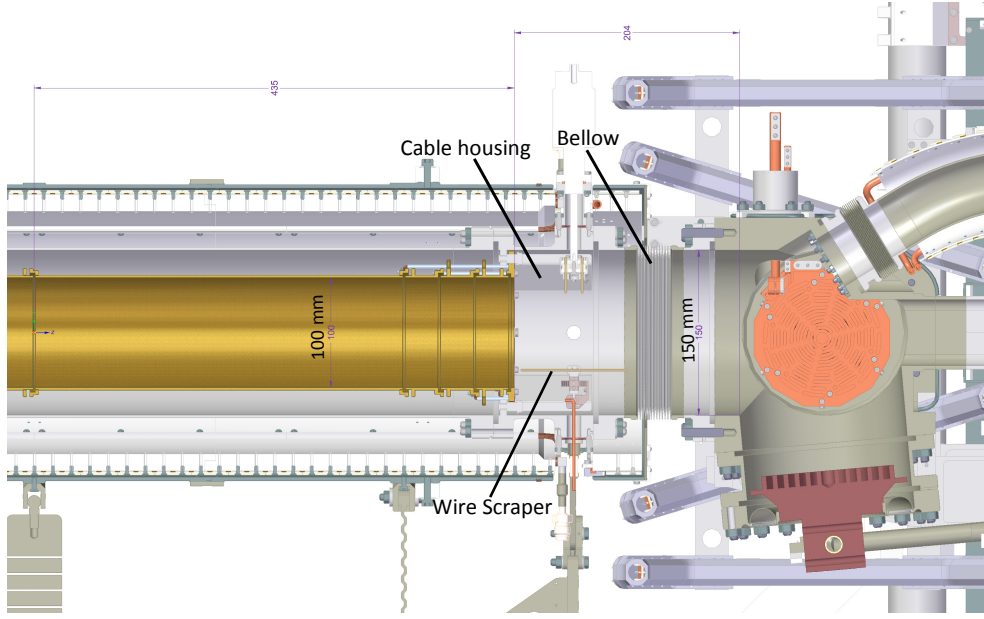
Figure 4.10: CAD model of the symmetric half of the interaction region.

half CAD model converted into a potential array with discretization of 0.2 mm. All drift tube electrodes were grounded to make a realistic simulation. A charge density array was also defined with same dimension and cylindrical charge density of radius 6.8 mm placed at the center of potential array. In the present space charge calculation model, electron density is treated in electrostatic manner and the U_{sc} is overestimated as 6.7 mm is the r_{beam} for expansion 20.

Fig. 4.11 shows the variation of U_{sc} along the longitudinal axis. The U_{sc} remains constant at ~ 0.68 V upto the end of drift tube region. Then there is small bump of lower slope suggesting a small increament in the cross section and later slope is steeper and reaching upto ~ 0.76 V. The potential drop near center of electron cooler is attributed to artificial effect and not considered in further analysis. In the experiment, the space charge potential is corrected with respect to the center of the interaction region. Hence, the space charge corrected electron energy at cooling is $E_c^{sc}(z) = E_c + e(U_{sc}^d - U_{sc})$. Here U_{sc}^d is the nominal space charge potential in drift tube region. The difference between U_{sc}^d and U_{sc} is up to $\sim - 0.08$ V and this suggests over certain part of interaction region the electron beam energy is lower up to 0.08 eV from cooling energy. The above result can be scaled for different densities as other beam and experimental parameters remain same.

Additionally, the electron beam potential along transverse direction in non-uniform
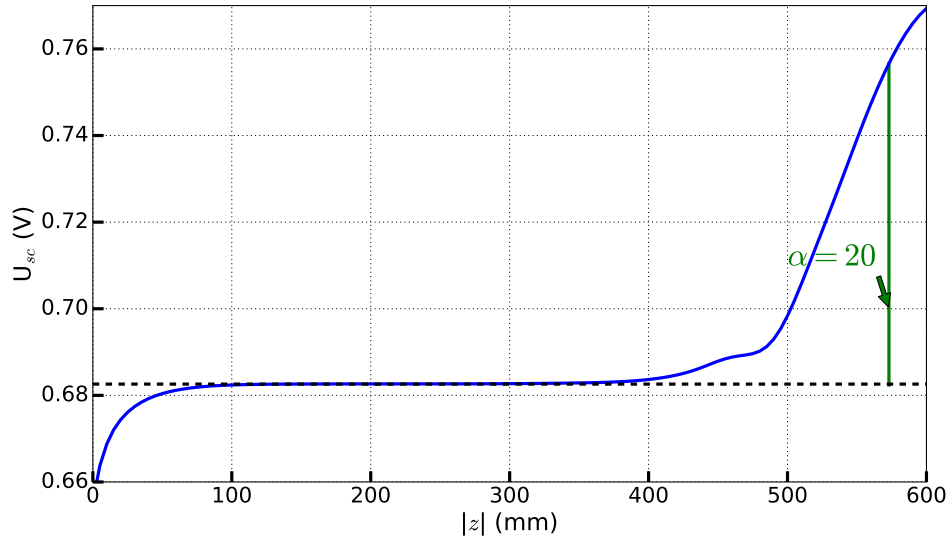
Figure 4.11: Space charge potential variation along longitudinal axis. The black dotted line shows the U_{sc} in drift tube region.

cross section of the experimental chamber is also investigated. Fig. 4.12 shows the longtitunal slice of potential array along two orthogonal planes. The red lines are the equipotential lines in the symmetric half of the interaction region and their corresponding values are shown. The equipotential lines of 0.16 V, 0.46 V and 0.58 V from the drift tube region diverge outward in merging region as the tube dimension increased. 0.72 V potential line near the center of beam originate only in merging region. In yz plane (A), presence of the wire scraper changes the equipotential lines for farther from the central axis and it does not remain symmetric anymore. However, in xz plane (B) the potential lines are nearly symmetric. For magnetic expansion of 30, asymmetry in potential along yz plane and xz plane can be larger. If electron beam is displaced from the central axis in the interaction region more asymmetricity in the potential can be anticipated.

The electron-ion collision energy in the interaction region is also investigated. Here, E_c^{sc} is used for the cooling energy. Fig. 4.13 shows the collision energy is very similar to the standard position dependent energy (see fig. 4.9). The difference between the two energies show the contribution from space charge variation (~ 0.08 V) is only up to - 1 meV (fig. 4.13(b)).
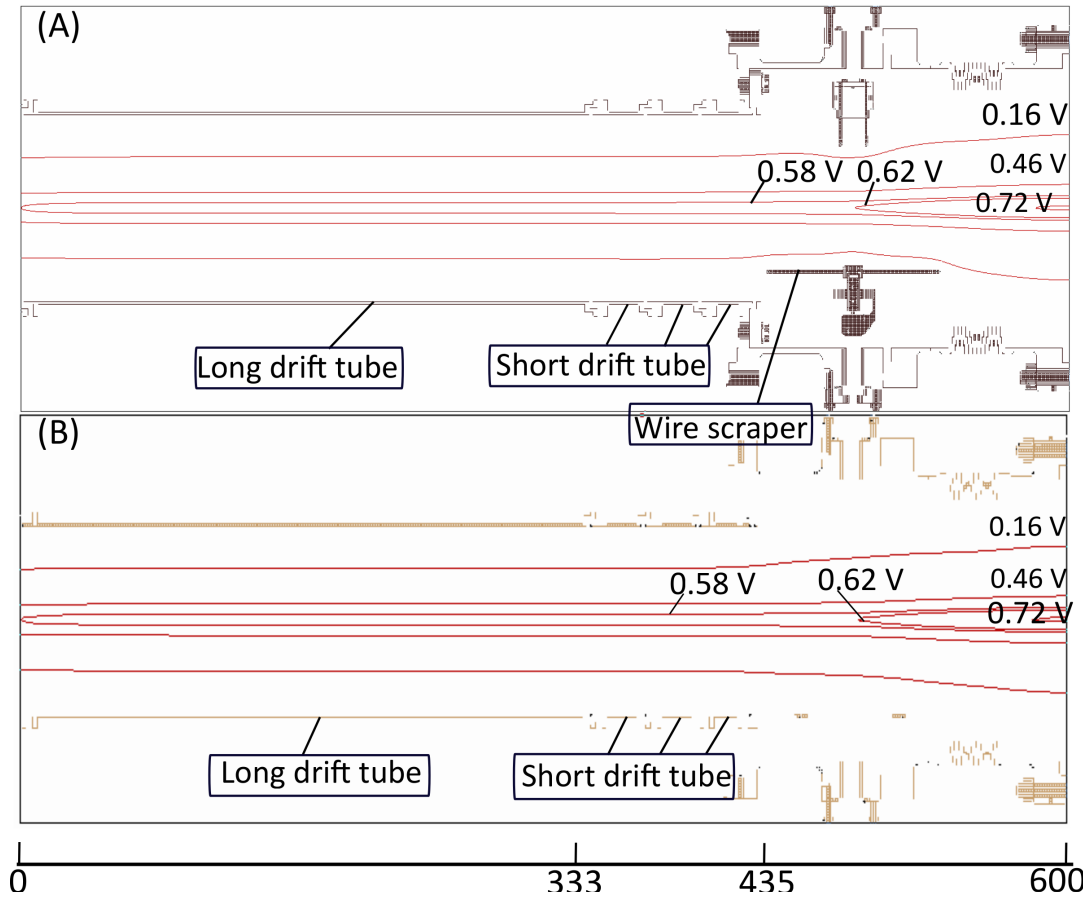
Figure 4.12: Potential array of the symmetric half of the interaction region. The position of drift tubes are shown with respect to the center of electron cooler. The long drift tube, short drift tubes and wire scraper are shown. (A) is the sliced potential array along yz plane. Presence of wire scraper deviates the equipotential line. (B) is the sliced potential array in xz plane.
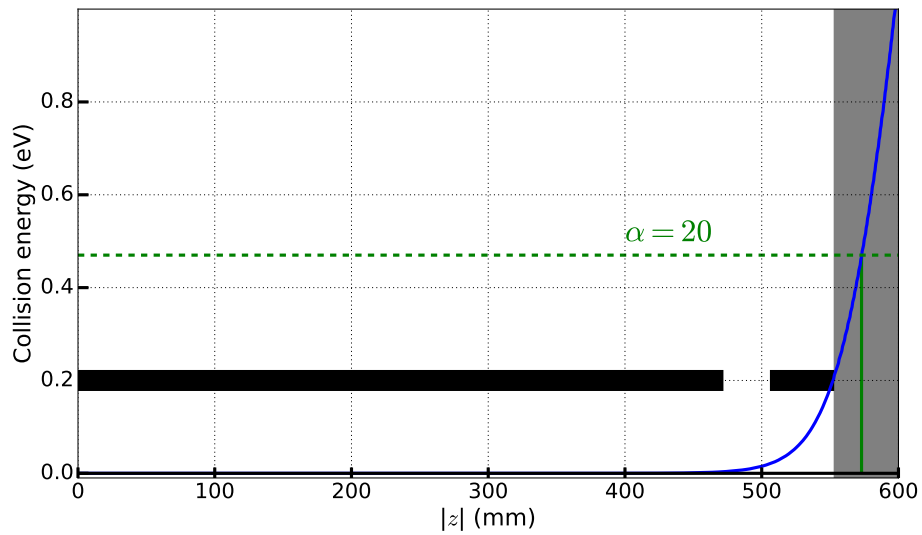
(a)
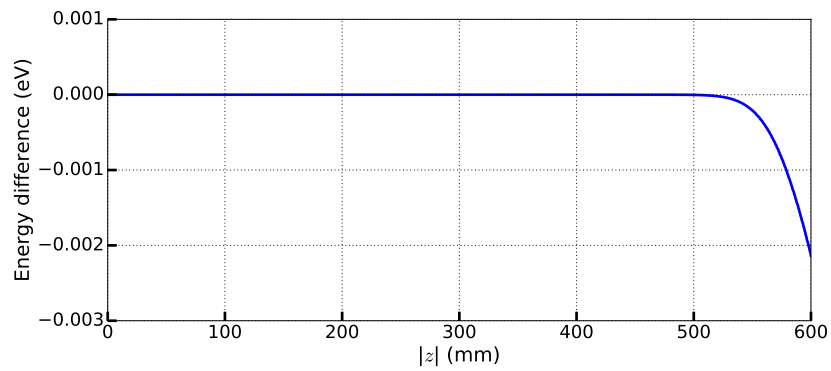
(b)

Figure 4.13: (a) Collision energy as function of position with variation due to space charge difference included. (b) Difference between energies of standard overlap geometry with the space charge variation included energy.

4.4 Drift tubes in the interaction region

For cooling of heavy and singly charged ions, electron energies of only a few eV are required. The maximum electron density at low energy is constrained by the electron gun perveance limit, since the extraction voltage cannot be higher than the acceleration potential of the cathode (see sec. 3.3). In addition, at low electron energies, space charge of the beam and contact potential difference between cathode (W_c) and drift tube (W_a) materials become comparable to the final electron energy.

In TSR storage ring electron target, high energy electron beam decelerated in the interaction section with the application of drift tube electrodes up to 1 eV [67]. This resulted in an electron beam of well defined energy and also enhancement in density by one order of magnitude even at 1 eV or lower was obtained. This beam deceleration technique was tested in [67] which paves the way to achieve similar scheme in CSR electron cooler for cooling and fragmentation experiments.
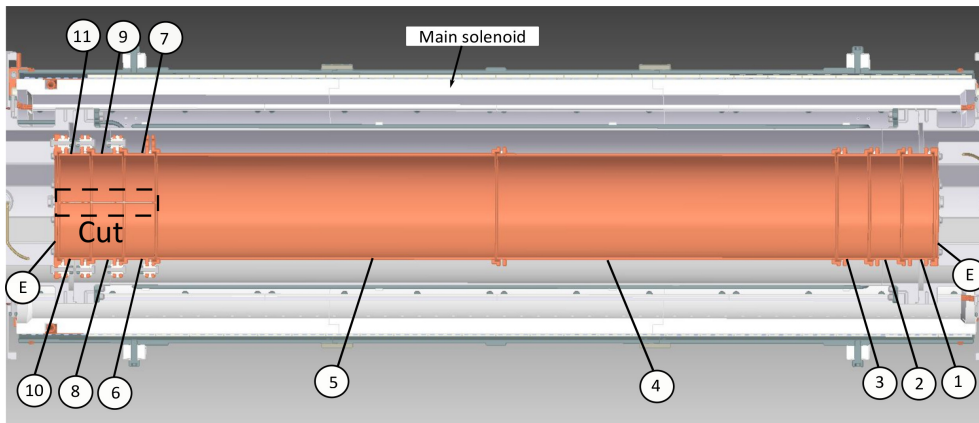
Figure 4.14: Mechanical design of the interaction region showing the Main Solenoid (MS) and drift tubes. From the right side electrode (E) is 3 mm long end cap, next is set of three 30 mm long electrodes (1-3) followed by two center electrodes (4-5) 333 mm long each. Finally, (6-11) electrodes are 30 mm long and also contains (E) 3 mm long end cap.

Fig. 4.14 shows the mechanical model of the interaction region of the electron cooler. It shows the main solenoid of length 944 mm with gold-coated copper drift tube electrodes. The total combined length of all drift tube electrode is 870 mm, technically designed as long as possible inside the uniform magnetic field of main

solenoid [48]. There is a gap of 2 mm between each electrodes to enable the possibility of applying different potentials and it also ensures the breakdown of voltage up to several keV. Moreover, (6-11) electrodes are similar to (1-3) but with cut along the vertical axis and can be used as clearing elctrodes. The space charge of the electron beam creates potential difference along the radial direction of the beam (see sec. 4.3). Rest gas present in the experimental beamline could get ionized due to electron impact ionization and therefore, could be trapped in the space charge potential of the electron beam. To mitigate this build up of trapped ions, equal and opposite potential (typically 1-2 V) can be applied on the clearing electrodes to spill out the trapped ions.
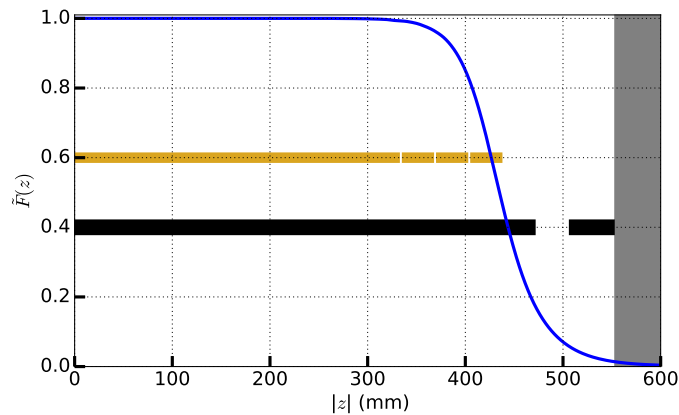
Figure 4.15: Illustration of normalized potential $\tilde{F}(z)$ in the interaction region. It is maximum in the center of the interaction region and vanish to zero outside. The bold black lines represent the position of main solenoid and short solenoid (see fig. 4.1). The golden yellow lines represent the position of drift tube electrodes and the grey shaded area correspond to merging region.

Based on change in electron beam energy from cathode region to the interaction region, a normalized potential is defined as,

$$\tilde{F}(z) = \frac{E_e(z) - E_{cath}}{eU_{drift}} \tag{4.9}$$

where $\tilde{F}(z)$ is the normalized potential and E_{cath}, $E_e(z)$ are electron energy in the cathode region and in the interaction region at point z, respectively. U_{drift} is the applied negative potential on the drift tube electrodes. G4beamline, a particle

tracking routine is employed to obtain this potential and effective kinetic energy of the electron beam as function of z (see sec. 3.6)[64]. Fig. 4.15 shows the normalized potential of drift tubes in the interaction region. For a test case, an electron starts at $E_{cath} = 25$ eV kinetic energy from cathode position and all drift tube electrodes (1-11) are set at $U_{drift} = -5$ V to have 20 eV velocity matched energy at the center of interaction region.

The electron energy at any position z in the interaction region is given by,

$$E_e(z) = E_{cath} + W_c + e\tilde{F}(z)U_{drift} - W_a - eU_{sc} \tag{4.10}$$

where W_c and W_a are the contact potential of the cathode and drift tube (anode), repsectively. These potentials are experimentally determined and therefore, neglected in this calculation. The electron while entering the interaction region sees a retarding potential of the drift tube which in turn decelarates the electron to 20 eV in the region of constant potential.
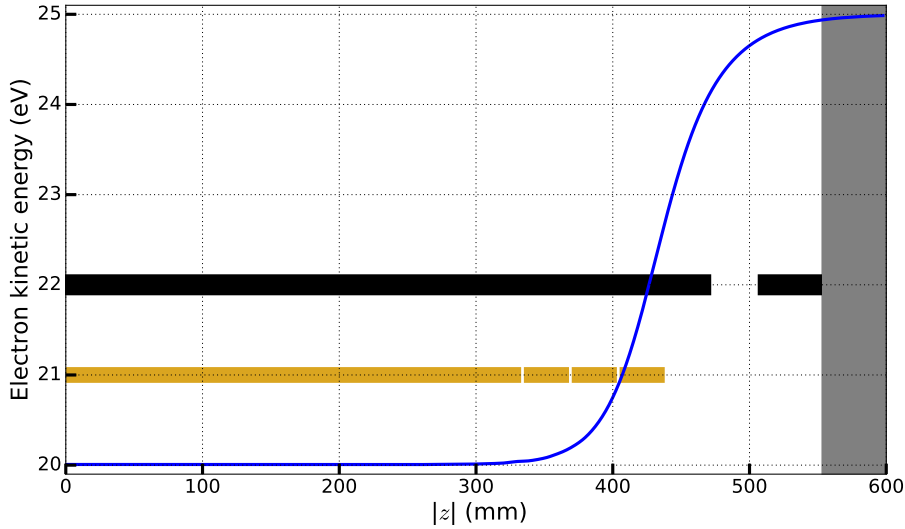
Figure 4.16: Effective kinetic energy of decelerated electron in the interaction section. The bold black lines represent the position of main solenoid and short solenoid (see fig. 4.1). The golden yellow lines represent the position of drift tube electrodes and the grey shaded area correspond to merging region.

Fig. 4.16 shows the effective kinetic energy of decelerated electron beam. The constant energy (20 eV) region is shortened in the interaction section. Also, there

is a steep rise in electron energy before and after (not shown here) drift tube region and therefore, contributes to the position dependent increasing electron energy in comparision to otherwise constant energy in standard operation with grounded drift tubes. Similarly, U_{drift} can be changed at a fix E_{cath} and energy scanning can be performed directly.
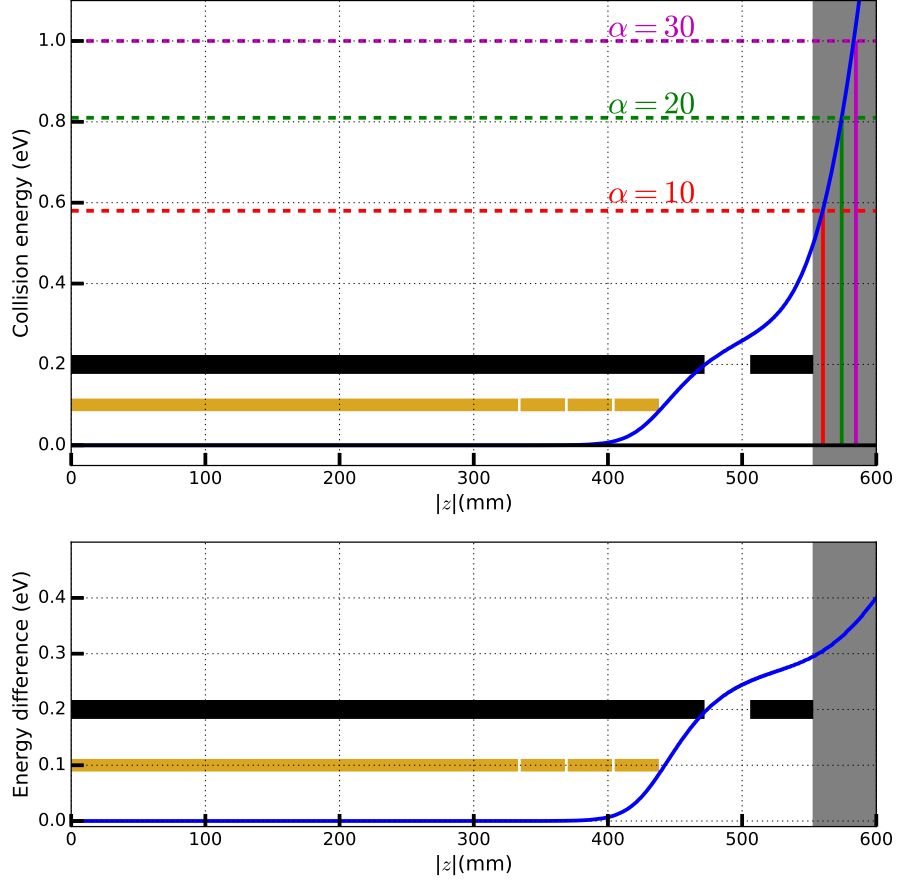
Figure 4.17: Upper: Electron-ion collision energy of the decelerated beam in the interaction section. Red, green and grey lines show limits for expansion factor $\alpha = 10$, 20 and 30 respectively. The bold black lines represents the position of MS and two short solenoids. The golden yellow lines represent the position of drift tube electrodes and the grey shaded area correspond to merging region. Lower: Collision energy difference of overlap geometry between drift tube operation and standard operation.

Since the trajectory of electron remains unchanged in deceleration process, transverse angle defined in sec. 4.2.2 and eqn. 3.11 is used to determine the collision

energy in the overlap region. Fig. 4.17 shows the electron-ion collision energy for decelerated beam. The zero-energy region is shortened to ~ 400 mm in comparision to ~ 500 mm in the standard operation (see fig. 4.9). As a consequence, collision energy rise up to 0.58 eV, 0.81 eV and 1 eV for expansion factor of 10, 20 and 30, respectively. The additional collision energy is from the steep rise in energy at the entrance and exit of the drift tube electrodes (see fig. 4.17(b)).

This should be general scheme to use drift tubes for cooling and electron-ion recombination experiments. However, since all drift tubes are physically seperated from one another, more exotic scenarios can be possible. For example, electrodes (1-4) can be placed at cooling energy and (5-11) can be applied potential to give a finite detuned energy (see fig. 4.14). In this way cooling and electron-ion collsions at chosen higher energy can be performed simultaneously. If only long central drift tubes (4-5) are to be used it makes the constant potential region smaller compared to when all the drift tube electrodes are used together.

4.5 Electron-ion collision energy distribution

In previous section, we have established one trajectory for the electron beam of energy up to 1 keV. The corresponding electron-ion collision energy from the overlap geometry in the center-of-mass frame leads to position dependent energy up to $\sim$ eV. The space charge correction for varying experimental beam tube dimension has been calculated at a fixed electron beam density. The collision energy difference with respect to the standard overlap geometry is very small (see fig. 4.13(b)). In drift tube operation, the new electron-ion collision energy at velocity matched condition further increase with respect to the standard position dependent collision energy (see sec. 4.4). In addition, finite energy spread of the electron beam originates from transverse and longitudinal temperature of the beam (see sec. 3.3.2). Electron and ion beams collision velocity distribution from thermal energy spread has already been discussed (see sec. 3.4).

In sec. 3.5.2, a general position dependent velocity distribution function and corresponding energy distribution has been introduced. In a previous work a numerical method has been developed to define the center-of-mass frame energy distribution function represented by $f_{mb}(E, E_d; T_\perp, T_\parallel, X)$ [72]. Here we will use the numerical method to define the energy distribution function for a more general case represented as $f_{mb}(E, E_d; T_\perp, T_\parallel, X, U_{sc}, U_{dr})$, where E is the center-of-mass electron-ion

energy, E_d is detuning energy, $T_\parallel$ and $T_\perp$ represents the effective energy spread of the beam along longitudinal and transverse directions, respectively. And, X represents the contribution from overlap geometry, space charge correction and drift tube operation if used are represented by U_{sc} and U_{dr}, respectively.

A Monte Carlo simulation is used to combine overlap geometry with the electron beam energy spread. To achieve low uncertainty of f_{mb}, Monte Carlo simulation requires large number of simulated electron-ion collision events. The method considers electron beam of cylindrical geometry and phase space cooled ion beam as straight line of negligible cross section as discussed in sec. 4.2.2. The electron and ion beams are assumed to have uniform density in order to have uniform probability distribution across the interaction region. The interaction length l_{int} consists of equidistant points, a collision event is randomly generated along the interaction region. The corresponding angle θ (see sec. 4.2.4) is the collision angle between electron and ion at that point. This means electron velocity vector is rotated by angle θ for that event.

For the present simulation, we have chosen temperature of the electron beam along longitudinal direction, $T_\parallel$ = 50 μeV$/k_B$ and along transverse direction, $T_\perp$ = 1 meV$/k_B$. The corresponding velocity spread can be given by Gaussian width centered at 0 and at longitudinal electron velocity, respectively as,

$$\sigma_\perp = \sqrt{\frac{k_B T_\perp}{m_e}} \quad \text{and} \quad \sigma_\parallel = \sqrt{\frac{k_B T_\parallel}{m_e}} \tag{4.11}$$

where k_B is Boltzmann constant and m_e is the mass of electron. For given collision event, transverse velocity components along x and y directions are separately randomly generated from the Gaussian distribution as $v_x^{(T_\perp)}$ and $v_y^{(T_\perp)}$, respectively. Similarly, longitudinal velocity spread is also randomly generated as $v_z^{(T_\parallel)}$. Finally, the longitudinal component of electron velocity at any detuning energy E_d (see eqn. 3.12) and phase space cooled nearly monoenergetic ion beam velocity are given by:

$$v_{e,\parallel} = v_i + v_d \quad \text{and} \quad \vec{v}_i = \begin{pmatrix} 0 \\ 0 \\ v_i \end{pmatrix} \tag{4.12}$$

In a more general case of drift tube operation and inclusion of space charge variation, as we have already seen that the electron energy is position dependent. The position dependent longitudinal electron velocity is defined as,

$$\bar{v}_e(z) = v_{e,\parallel} + \delta(z) - v_{sc}(z) \tag{4.13}$$

where $v_{e,\parallel}$ is the electron velocity in the center of interaction region. $\delta(z)$ and v_{sc} are the additional velocity in the beam direction in drift tube operation and due to space charge variation, respectively. The definition of respective velocity terms are,

$$\delta(z) = \sqrt{\frac{2}{m_e}\left(E_{cath} - (\sqrt{E_c} + \sqrt{E_d})^2 + e\tilde{F}(z)U_{drift}\right)} \tag{4.14}$$

A constant energy $E_e = (\sqrt{E_c} + \sqrt{E_d})^2$ is subtracted from $E_e(z)$ given in eqn. 4.10. The last term in eqn. 4.13 is

$$v_{sc}(z) = \sqrt{\frac{2}{m_e}\left(|e(U_{sc}^d - U_{sc})|\right)}. \tag{4.15}$$

Similarly, the energy E_e is subtracted from $E_e(z) = E_e + e(U_{sc}^d - U_{sc})$. where U_{sc}^d is the space in the drift tube region. The variation in U_{sc} decreases the velocity.

Based on above defined relations, final electron velocity for the given event including overlap geometry contribution for a general case is given as,

$$\vec{v}_e^X = \begin{pmatrix} 1 & 0 & 0 \\ 0 & \cos\theta & \sin\theta \\ 0 & -\sin\theta & \cos\theta \end{pmatrix} \begin{pmatrix} v_x^{(T_\perp)} \\ v_y^{(T_\perp)} \\ \bar{v}_e(z) + v_z^{(T_\parallel)} \end{pmatrix} = \begin{pmatrix} v_x^{(T_\perp)} \\ v_y^{(T_\perp)}\cos\theta + (\bar{v}_e(z) + v_z^{(T_\parallel)})\sin\theta \\ -v_y^{(T_\perp)}\sin\theta + (\bar{v}_e(z) + v_z^{(T_\parallel)})\cos\theta \end{pmatrix} \tag{4.16}$$

The first matrix in eqn. 4.16 is the rotation matrix in yz plane amounts to angle θ. The electron velocity can be separated into electron velocity along the trajectory and rotated thermal velocity component:

$$\vec{v}_e^X = \begin{pmatrix} 0 \\ \sin\theta \\ \cos\theta \end{pmatrix} \bar{v}_e(z) + \begin{pmatrix} v_x^{(T_\perp)} \\ v_y^{(T_\perp)}\cos\theta + v_z^{(T_\parallel)}\sin\theta \\ -v_y^{(T_\perp)}\sin\theta + v_z^{(T_\parallel)}\cos\theta \end{pmatrix} \tag{4.17}$$

The relative velocity of the electron and ion collision is,

$$\vec{v} = \vec{v}_e^X - \vec{v}_i = \begin{pmatrix} 0 \\ \sin\theta \\ \cos\theta \end{pmatrix} (v_i + v_d + \delta(z) - v_{sc}) + \begin{pmatrix} v_x^{(T_\perp)} \\ v_y^{(T_\perp)}\cos\theta + v_z^{(T_\parallel)}\sin\theta \\ -v_y^{(T_\perp)}\sin\theta + v_z^{(T_\parallel)}\cos\theta \end{pmatrix} - \begin{pmatrix} 0 \\ 0 \\ 1 \end{pmatrix} v_i \tag{4.18}$$

$$\vec{v} = \begin{pmatrix} 0 \\ 0 \\ 1 \end{pmatrix} v_d + \begin{pmatrix} 0 \\ \sin\theta \\ \cos\theta - 1 \end{pmatrix} (v_i + v_d) + \begin{pmatrix} 0 \\ \sin\theta \\ \cos\theta \end{pmatrix} (\delta(z) - v_{sc}) + \begin{pmatrix} v_x^{(T_\perp)} \\ v_y^{(T_\perp)}\cos\theta + v_z^{(T_\parallel)}\sin\theta \\ -v_y^{(T_\perp)}\sin\theta + v_z^{(T_\parallel)}\cos\theta \end{pmatrix}$$

$$(4.19)$$

The relative velocity is decomposed into several individual contributions. The first vector is the average collision velocity of the electron and ion beam, the second term is contribution from overlap geometry of the set up, third term is position dependent longitudinal velocity due to the drift tube operation (if used) and space charge variation and last term is the thermal velocity contribution for the given event. The electron-ion collsion energy is described in center-of-mass frame with $E = \frac{1}{2}\mu v^2$. Here $\mu = m_e m_i/(m_e + m_i)$ is the reduced mass of electron and ion. Since ion is much heavier than electron, $\mu = m_e$ and, hence, $E = \frac{1}{2}m_e v^2$.

Likewise, collision events are generated and E is calculated for each event. For all cases of f_{mb} simulation, we generated normalized distribution for 10^7 collision events at $E_c = 20$ eV for magnetic expansion $\alpha = 20$. In addition, unless stated it is assumed that the space charge potential is compensated with respect to the center of the interaction region to obtain velocity matched cooling energy. We use $log-log$ scale to plot energy distribution functions to show the features especially in the high energy region where collision events are few orders of magnitude less than the peak of the distribution.
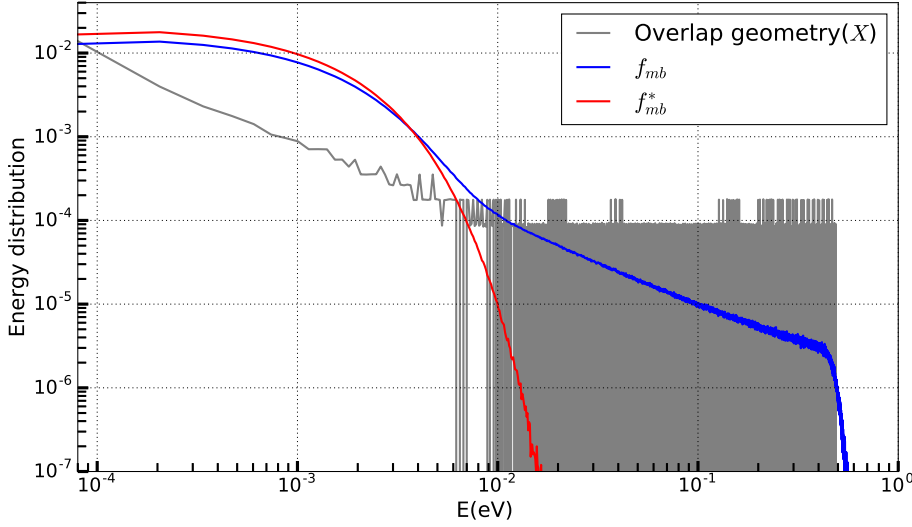
Figure 4.18: Comparision of simulated electron-ion collision energy distribution at $E_d = 0$ in the interaction region. Red distribution shows the effect of energy spread only due to the electron temperature. Grey curve represents the distribution of center-of-mass energy coming only from the overlap geometry. And the blue curve depicts the electron energy spread due to the combined effect of temperature and overlap geometry.

Fig. 4.18 shows the comparision of f_{mb} with thermal distribution, also denoted by f_{mb}^*, and the distribution only from overlap geometry of the beam at velocity matched condition($E_d = 0$). Red curve shows the flattend energy distribution due to asymmetric temperature of the electron beam and it is dominated by transverse beam temperature. To compare the enhancement in distribution energy from the overlap geometry is the grey curve and maximum energy in the distribution is ~ 0.5 eV same as overlap energy spread (see sec. 4.2.4). Blue curve is the final f_{mb} with overlap geometry X contributing to the tail in the high energy.

Energy distribution with space charge

Here we study the effect of position dependent longitudinal velocity v_{sc} due to the variation in space charge in addition to the overlap geometry (see eqn. 4.19) and denoting the corresponding energy distribution function as $f_{mb}(U_{sc})$. Fig. 4.19 shows the comparision between nominal f_{mb}, $f_{mb}(U_{sc})$ and f_{mb}^* distribution at $E_d = 3$ eV.

This distribution differs only in the high energy tail region which is more than 2 orders of magnitude lower than the peak of the $f_{mb}(U_{sc})$ distribution. In fact, it has also less energy spread than the nominal f_{mb}. In total, the accurate usage of space charge variation makes very small difference and hence, can be neglected in further calculations.
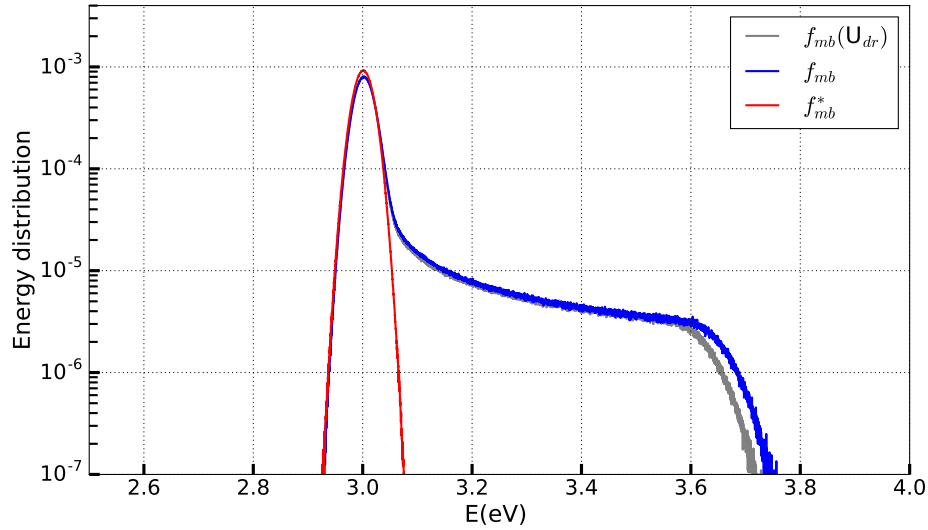
Figure 4.19: Collision energy distribution comparision at $E_d = 3$ eV with space charge $f_{mb}(U_{sc})$ and standard distribution f_{mb}. Grey curve is space charge included distribution and blue distribution is the nominal f_{mb}.

Energy distribution in drift tube

In the next step we include the position dependent longitudinal velocity $\delta(z)$ in the energy distribution simulation (see eqn. 4.19). Fig. 4.20 shows the drift tube mode collision energy distribution $f_{mb}(U_{dr})$ and nominal f_{mb} at velocity matched condition ($E_d = 0$). The distribution in low energy region is further lowered in amplitude and tail in the high energy is also increased in $f_{mb}(U_{dr})$. In drift tube operation 30 eV (E_{cath}) electron beam decelerated by -10 V to reach 20 eV velocity matched energy in the center of the interaction region.
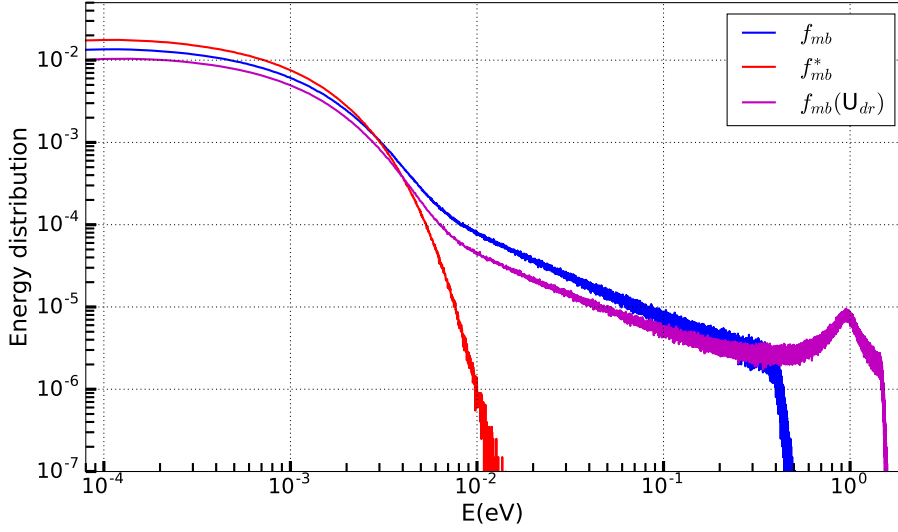
Figure 4.20: Electron-ion collision energy distribution at $E_d = 0$ in the standard mode (without drift tube) and with drift tube mode of operation. For drift tube mode collision energy distribution goes higher energy region due to shortening of the zero collision energy region (see sec. 4.4).

In addition, the energy distribution at $E_d = 1$ meV, 10 meV, 0.1 eV, 0.5 eV, 1 eV and 10 eV are compared for $f_{mb}(U_{dr})$ and corresponding nominal f_{mb} as shown in fig. 4.21. For each distribution, the energy spread in thermal distribution (f_{mb}^*) is also shown in red which shows that for increasing E_d it becomes more narrower in relative size. The fraction of distribution below E_d shows the contribution of $k_B T_\parallel$ and it decreases with increasing E_d. Furthermore, at a given detuning energy in all three distributions, the peak position remains close to E_d and the peak of the distribution is lowest in $f_{mb}(U_{dr})$ as anticipated than respective f_{mb} and f_{mb}^* (up to 0.5 eV). An inset showing the peak amplitude of the energy distribution function is also included. However, at $E_d = 1$ eV the $f_{mb}(U_{dr})$ distribution is nearly same to the f_{mb} and this due to the fact that E_e is 29.94 eV and E_{cath} is 30 eV (see eqn. 4.10) and therefore, $\delta(z)$ amplitude is rather small. At $E_d = 10$ eV thermal distribution and standard energy distributions are narrow. However, $f_{mb}(U_{dr})$ is distributed over nearly 1-10 eV and this stems from the fact that the role of drift tube is reversed. At $E_d = 10$ eV the constant energy in the center of interaction region is 58.28 eV which is higher than E_{cath} and it means we accelerate the electrons in the interaction region. Therefore, the $\delta(z)$ (see eqn. 4.14) is very high but with reversed sign.

The energy distribution near the peak is proportional to the straight part of the interaction region which has been introduced as l_{eff} in earlier sec. 3.5.2. However, the absolute value of l_{eff} cannot be determined based on this information.
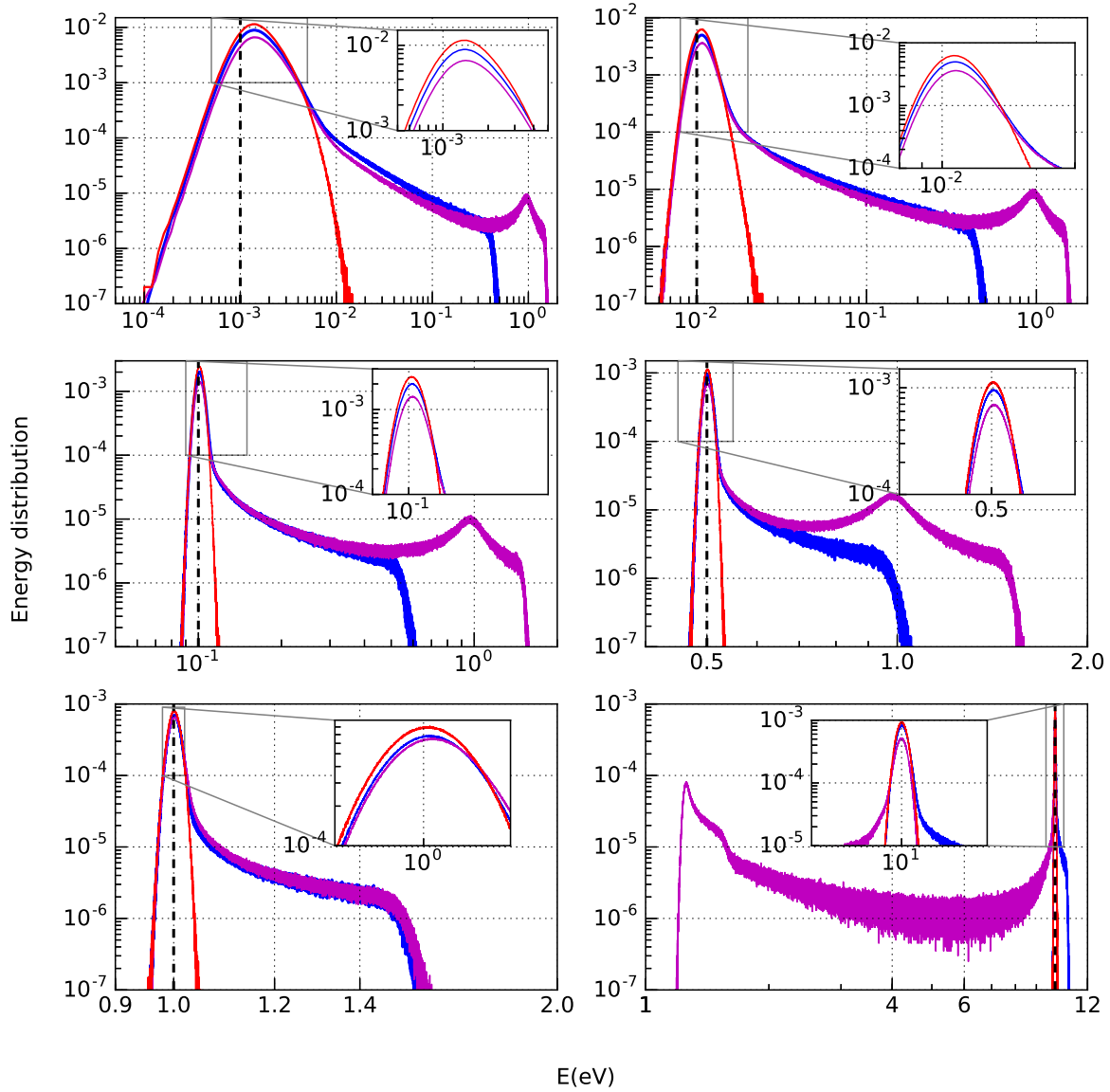
Figure 4.21: Electron-ion collision energy distribution at $E_d = 1$ meV, 10 meV, 100 meV, 0.5 eV, 1 eV, and 10 eV in the standard operation (shown in blue), drift tube operation (shown in magenta) and thermal distribution in red, respectively. In drift tube operation collision energy distribution extends up to energy region higher than standard operation due to additional position dependent velocity component (see eqn. 4.14). Also, $U_{cath} = 30$ V is used in drift tube operation.

4.6 Model merged beams rate coefficient

Electron-ion merged beams rate coefficient relation shown below has already been described in sec. 3.5.2 as the convolution of σv over the energy distribution function f_{mb}. In this section we will use the known energy distributions to simulate rate coefficients in separate cases of standard operation and drift tube operation. We will also discuss the energy range to obtain the l_{eff} and scaling factor (l_{int}/l_{eff}) also introduced earlier to scale the rate coefficient α_{mb}.

$$\alpha_{mb}(E_d) = \langle \sigma \sqrt{2E/m_e} \rangle = \int \sigma(E)\sqrt{2E/m_e}f_{mb}(E, E_d; T_\perp, T_\parallel, X)dE \qquad (4.20)$$

In low collision energy region, electron induced processes like indirect dissociative recombination or dielectronic recombination cross section consist of very sharp resonances. To understand the combined effect of thermal energy spread and overlap geometry, a delta-like cross section at 10 meV is convolved with energy distribution f_{mb}.
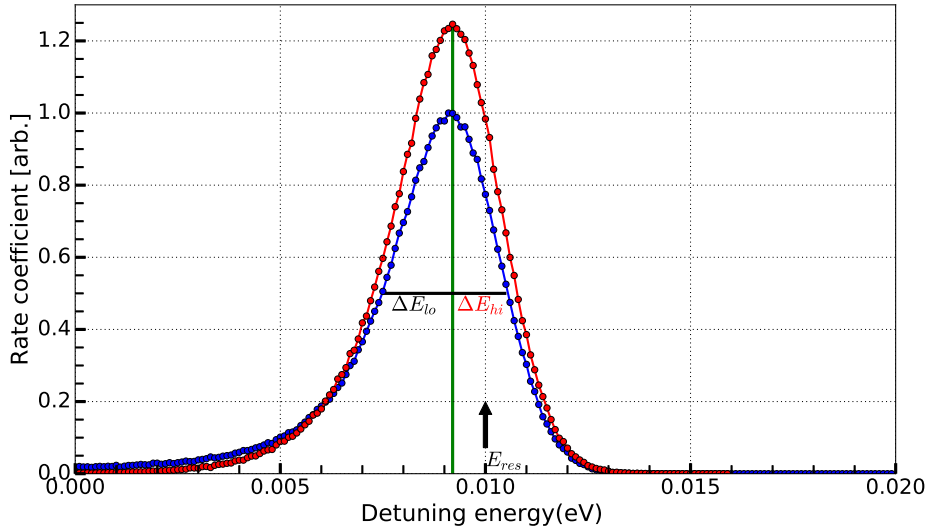
Figure 4.22: Illustration of convolved delta-like cross section with energy distribution f_{mb} (shown in blue) at $k_B T_\perp = 1$ meV and $k_B T_\parallel = 50$ μeV. The resonance position is at $E_{res} = 10$ meV. Also, the rate coefficient is obtained for the flattend distribution (shown in red). The low energetic broadening $(\triangle E_{lo})$ of the resonance is defined by $T_\perp$ and the high energetic $(\triangle E_{ho})$ by $T_\parallel$ (see fig. 3.5 and eqn. 3.31).

Fig. 4.22 illustrates the asymmetric lineshape of the rate coefficient of delta-like resonance. The FWHM of such lineshape for flattend distribution as a function of detuning energy has already been shown in fig. 3.31 and for comparision also simulated and shown in the fig. 4.22. The lineshape in case of standard operation is lowered in peak amplitude than thermal rate coefficient. The obtained FWHM for both curves are equal ~ 3 meV and slightly higher than 2.5 meV estimated from eqn. 3.31. The possible reason could be because the eqn. 3.31 is an approximated relation. Furthermore, the lineshape is similar to a Gaussian distribution at least within the half maximum and therefore, we will use the energy range of $\pm 3 \sigma$ for energy integration of rate coefficient.

In addition, we have also simulated rate coefficient of delta-like cross section at higher detuning energies, $E_d = 0.1$ eV, 0.5 eV, 1 eV, and 10 eV in standard and drift tube operation. The rate coefficient curves are normalized to the maximum of their respective standard operation rate coefficient. Fig. 4.23 shows the panel of overlaid curves. For increasing E_d the rate coefficient curves become more symmetric in shape. In the drift tube operation rate coefficient peak is also at same position but with lowered peak amplitude similar to the energy distribution functions (see fig. 4.21). It has been discussed earlier that the energy integration of α_{mb} is lower than the theoretical energy integrated rate coefficient $\hat{\alpha}_0$ (see eqn. 3.26) due to elevated energy in the full overlap region of length l_{int}, the effective straight region is shorter and denoted by l_{eff}. As rate coefficient peaks near the E_{res}, we will integrate f_{mb} over energy within $\pm 3\sigma$ of $E_d = E_{res}$ to obtain l_{eff} shown in eqn. 4.21. The 3 σ limits at $E_d = 10$ meV, 100 meV, 500 meV, 1 eV and 10 eV are 3.82 meV, 9.95 meV, 23 meV, 31.3 and 96 meV, respectively .

$$l_{eff}(E_{res}) = l_{int} \int_{E_{res}-3\sigma}^{E_{res}+3\sigma} f_{mb}(E_{res}, E_d; T_\perp, T_\parallel, X, U_{dr}) dE_d \qquad (4.21)$$

The integrated f_{mb} within $\pm 3\sigma$ in increasing order of E_d are 0.78, 0.85, 0.88, 0.89 and 0.92, respectively. In standard operation nearly 80-90 % of the collision events lies within $\pm 3\sigma$ of few meV in otherwise energy spread of $\sim$ eV. The effect of thermal energy decreases with increasing E_d. Likewise, integrated $f_{mb}(U_{dr})$ in increasing order of E_d are 0.58, 0.612, 0.65, 0.87 and 0.58, respectively. The fraction of collision events is proportional to the beam deceleration which is highest at 10 meV, very small at 1 eV and again high at 10 eV due to acceleration of the beam (see fig. 4.21). Based on the integrated energy distribution values, the obtained l_{eff} in standard and drift tube operation as function of E_d are shown in fig. 4.24. Fig.
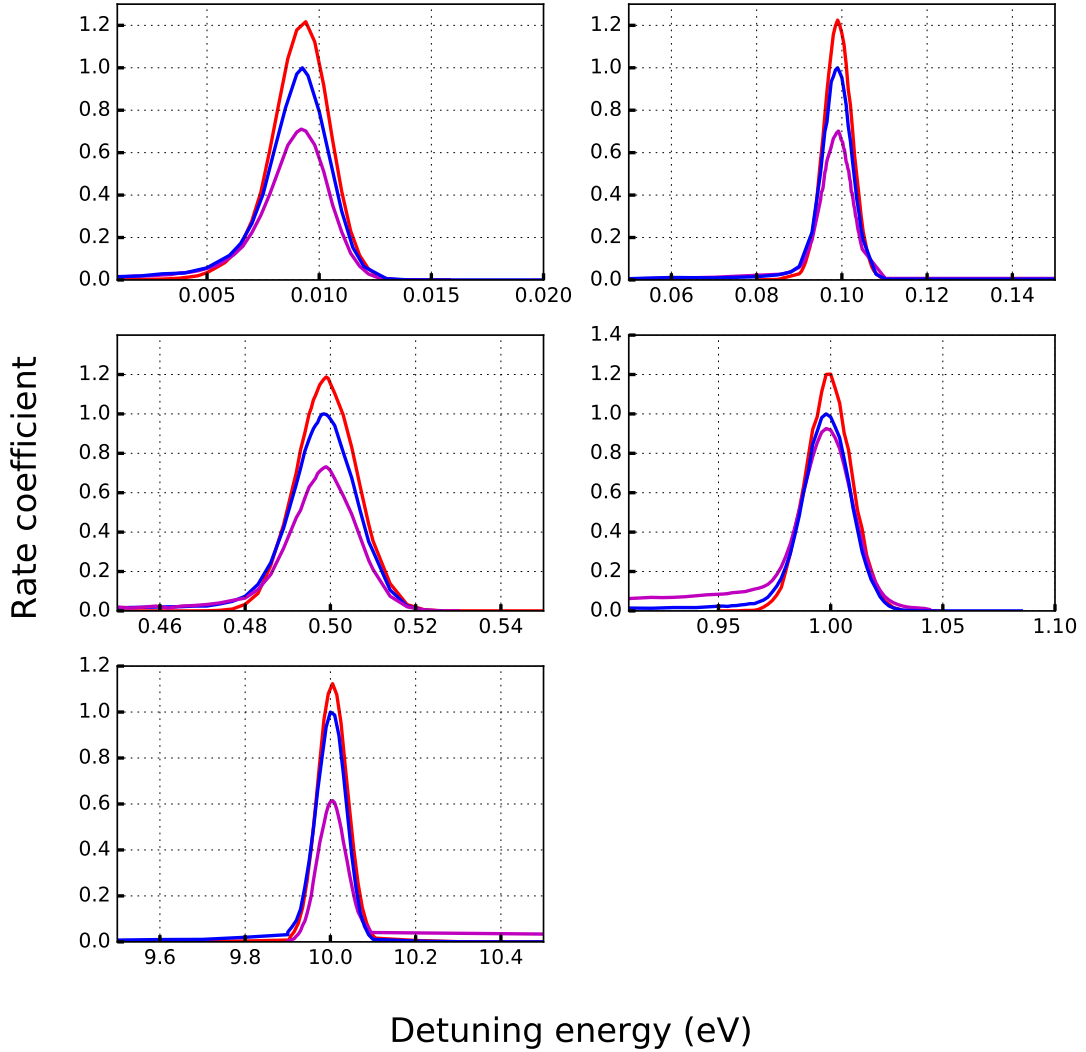
Figure 4.23: Comparision of rate coefficient of delta-like resonance at $E_d = 10$ meV, 100 meV, 0.5 eV, 1 eV, and 10 eV, respectively. The blue and red curves are the rate coefficient in standard operation and thermal distribution, respectively. Magenta curves are rate coefficient for drift tube operation with electron decelerated from 30 eV to 20 eV at cooling energy.

4.24 also shows the ratio of l_{int}/l_{eff}, the scaling factor for the rate coefficient α_{mb}. The scaled α_{mb} is α_m and its energy integration within $E_{res} \pm 3\sigma$ is equivalent to
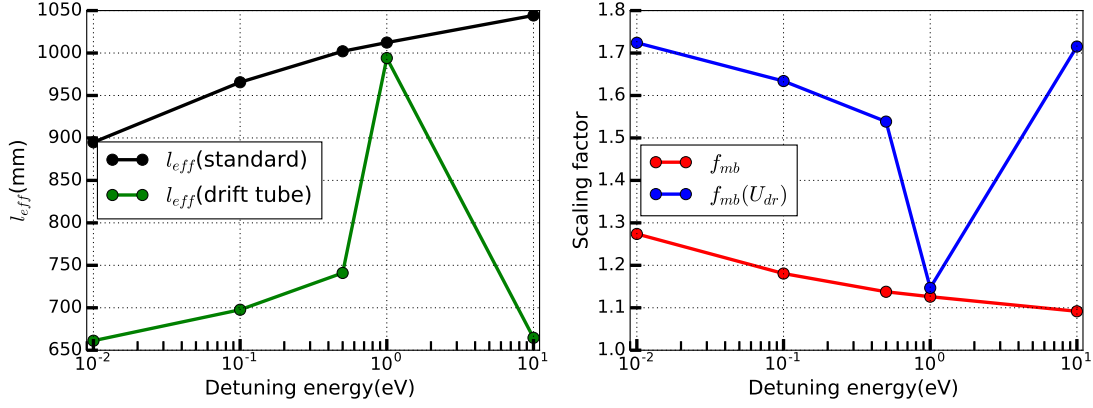
Figure 4.24: Illustration of the l_{eff} in the standard and drift tube operation obtained from energy integration in the $E_{res} \pm 3\ \sigma$ range for $l_{int} = 1150.5$ mm (see table. 4.3) . The scaling factor l_{int}/l_{eff} is used to scale simulated rate coefficient α_{mb}.

the theoretical energy integrated rate coefficient α_0. The scaled rate coefficient α_m is shown in fig. 4.25. The scaled standard and drift tube operation rate coefficients peak amplitude nearly matches with each other and also with the thermal rate coefficients.
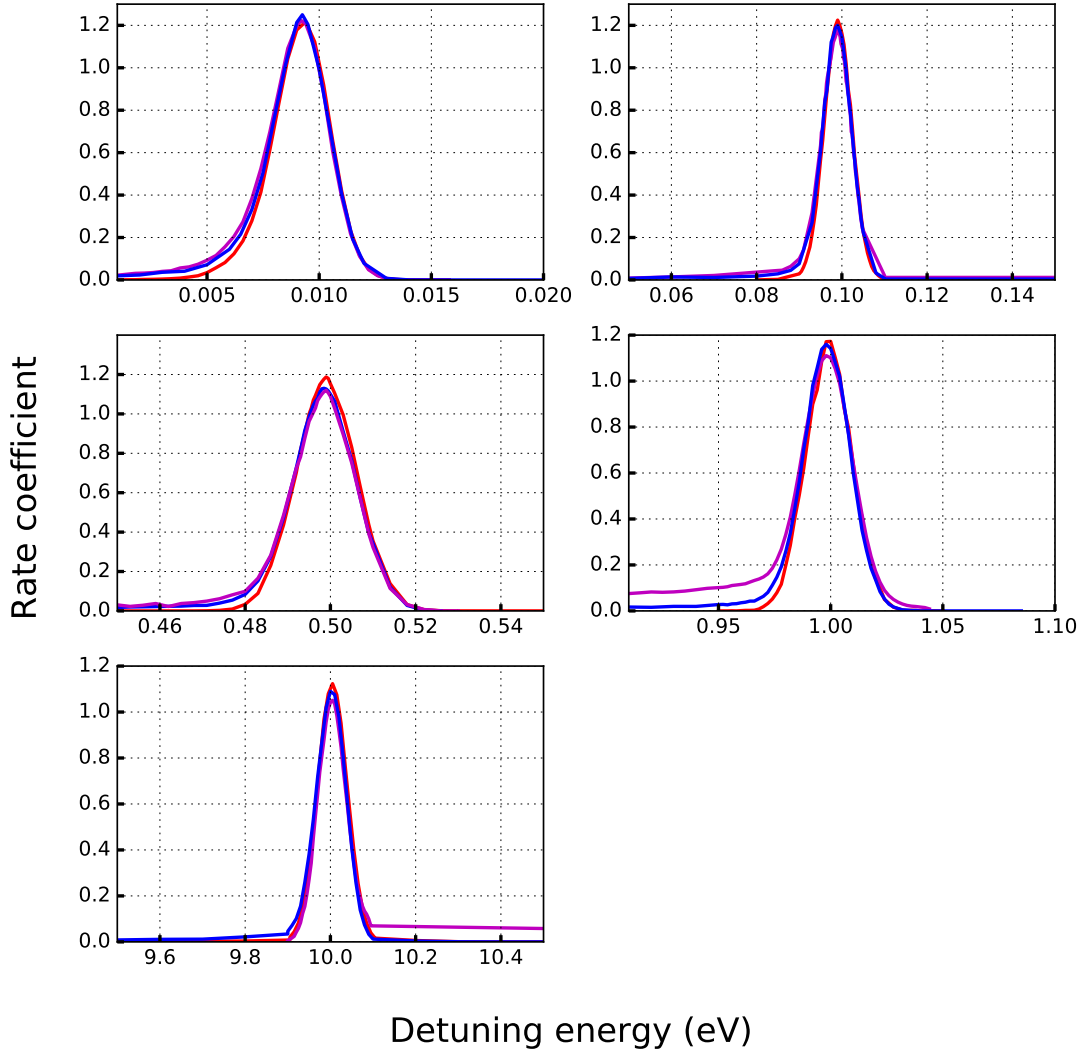
Figure 4.25: Illustration of scaled rate coefficient α_m of delta-like resonance at $E_d = 10$ meV, 100 meV, 500 meV, 1 eV and 10 eV, respectively. After scaling rate coefficients in standard and drift tube operations are nearly equal to the thermal rate coeffcients.

The above discussion facilitates an attractive method to eliminate the offset due to the overlap geometry or drift tube operation of the merged beams set up. Thus, the scaled rate coefficient α_m can be compared with other experiments. In addition,

experimental measurements can also be directly compared among the standard operation and drift tube operation. In the next chapter we will also use this method of scaling experimental rate coefficients of a cross section peak.
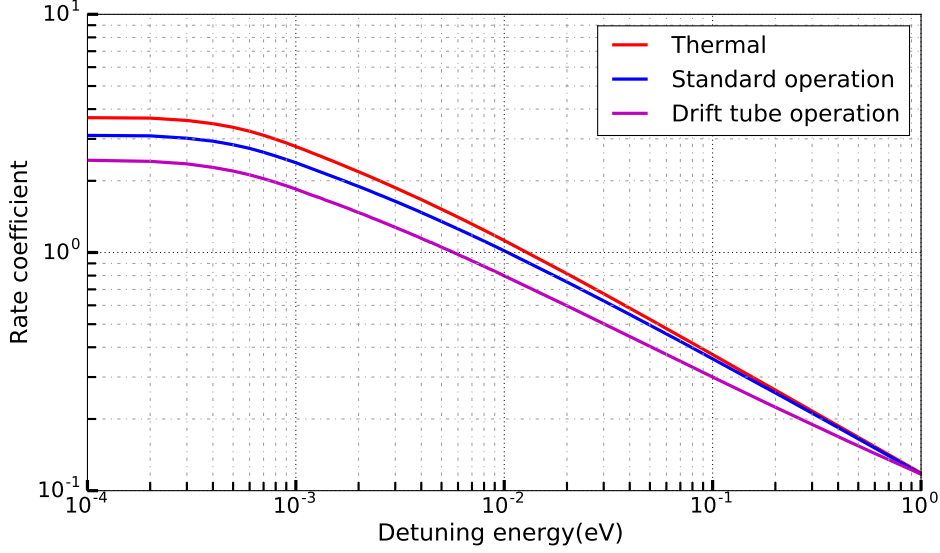
Figure 4.26: Illustration of rate coefficient of E^{-1} cross section in standard operation (shown in blue) and drift tube operation (shown in magenta) in the energy range of 0.1 meV to 1 eV at $k_B T_\perp = 1$ meV and $k_B T_\parallel = 50~\mu$eV. Also, the rate coefficient for the thermal distribution is plotted.

Furthermore, another most common type of cross section follows E^{-1} dependence on collision energy. The convolution of such cross section with energy distributions f_{mb}, $f_{mb}(U_{dr})$ and f_{mb}^* is illustrated in fig. 4.26. The thermal rate coefficient is highest in amplitude in low energy region than standard and drift tube operations. The finite energy spread from overlap geometry and drift tube potential lowers the rate coefficient at low energy.

5 Electron-ion collision studies

This chapter deals with the first dissociative recombination measurements on HeH^+ ions under cryogenic condition in the newly comissioned electron cooler. It starts with a general method to find the cooling energy (velocity matched energy) with the aid of diagnostic tools of the CSR. A measurement scheme is generated based on a sequence of short beam period at changing electron beam energy and the electron-induced signal is separated from the background signal. A relative merged beams rate coefficient is defined based on the electron induced signal and a proxy signal proportional to the number of ions.

The experiment is broadly divided into three parts. The first part deals with long storage time measurement giving the DR rate coefficient for a dominant population of the ro-vibrational ground state. Then measurement at short storage time to obtain time dependent rate coefficient. Finally, the usage of drift tubes in the interaction section to scan electron beam energy is realized for the first time at the CSR. The absolute rate coefficient is calculated and compared with previous room temperature measurement and recent theoretical results.

5.1 Introduction

The CSR and its various experimental platforms have been introduced earlier in sec. 3.1. Also, the fragmentation scheme of the electron-ion collision experiments has been described in sec.3.5. In the 2018 experimental campaign, we performed the first DR measurement at the CSR on the HeH^+ molecular ion. The HeH^+ ions were produced in a Penning ion source from a mixture of H_2 and He.

The detailed study of properties of the molecule has been already discussed in the sec.2.3. Briefly, HeH^+ ion is an infrared active molecule and therefore, rotationally relaxes in the CSR background temperature of less than 20 K of the experimental chambers (see sec.2.4). The produced HeH^+ ions are accelerated to 250 keV and stored in the CSR. The revolution frequency of the stored ions can be precisely determined with the aid of the current pick-up in the section C of the CSR (see
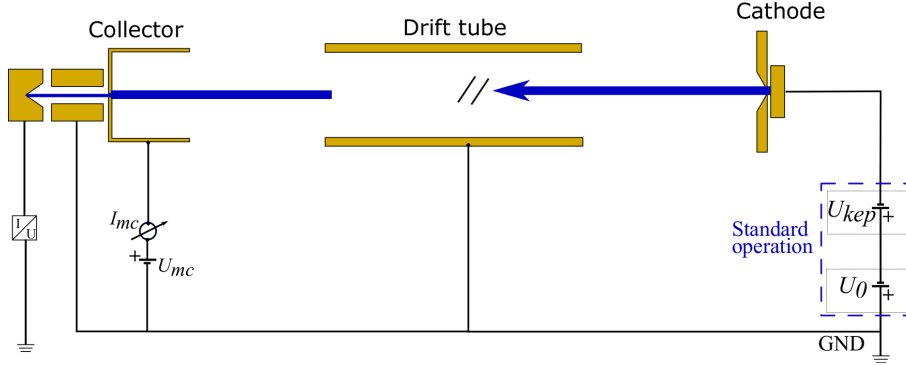
Figure 5.1: Electronic circuit used in the electron cooler for finding cooling energy and later use it as target for collision experiment. In standard operation (shown in blue), cathode is connected to U_0 static voltage and an USB-DAQ controlled fast switching power supply U_{kep}. The drift tubes are at ground in this configuration. The electron current I_e is measured in the main cup of the collector as I_{mc}. The details are discussed in the text.

fig. 3.1). From this, the velocity of ions is found by $v_i = f_0 C_0$, where $f_0 = 88.264$ kHz was the revolution frequency of the stored ion and $C_0 = 35.12(5)$ m is the CSR circumeference. The velocity matched electron beam energy can then be determined as $E_c = (1/2)m_e v_i^2 = 27.32(6)$ eV (see eqn.3.1).

In the present work, a method of electron beam acceleration and the related energy change of the beam is discussed briefly. As shown in fig. 5.1, the cathode is lifted to a negative potential with respect to ground with U_0 power supply (U_{kep} is set to 0 during electron cooling) and drift tubes in the interaction section are also grounded. The electron energy E_c at cooling is given by the cathode potential, $U_{cath} = -U_0$ after correcting for the difference in contact potential of the cathode (W_c) and drift tube electrodes (W_a) (see sec. 4.4). And, U_{sc} is the space charge potential (see sec. 4.3). In terms of these potentials the cooling energy E_c is obtained as

$$E_c = -eU_{cath} + W_c - W_a - eU_{sc} \tag{5.1}$$

5.2 Determination of the velocity matched energy

From eqn.5.1 it is seen that the cooling energy E_c, where ion and electron beams velocities are matched, is given by the directly controlled cathode potential plus

small corrections (W_c, W_a, U_{sc}). Also, the cooling energy is sensitive to the overlap between the electron and ion beams. There is a need to identify a tool box for achieving the cooling energy. For a given position of the ion beam, electron beam position and angle can be manipulated by the application of vertical and horizontal magnetic fields in the interaction region. The wire scraper is used to check the overlap between the beams. After finding a reasonable overlap, U_{cath} is scanned to fine adjust the cooling energy. Therefore, finding exact cooling energy is an iterative process. The RF bunching system used in conjunction with the current pick-up electrode gives a strong electrical signal at the onset of electron cooling that sensitively depends on the cooling energy E_c.
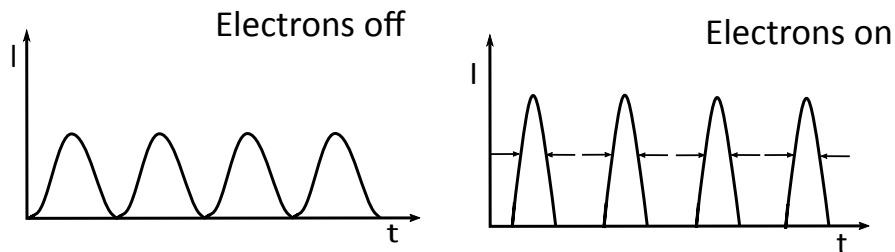
Figure 5.2: Illustration of intensity distribution of bunched ion beam on pick-up electrode in time domain for electron beam off (before cooling) and electron on, respectively.

A RF voltage signal with frequency $f_{RF} = 4f_o$ is applied to one of the drift tube electrodes of the RF bunching system in the CSR (see fig. 3.1) which in turn leads to the formation of a bunched ion beam. The bunched ion beam induces stronger signal on pick-up electrode in comparison to the non-structured ion beam [48]. In an uncooled bunched ion beam, ions are widely distributed over the four sections of the beam circumference created by f_{RF}. At a fixed point the longitudinal intensity distributions is $I(s,t) \approx I_0 \cos^2(\pi f_{RF}t - \phi_0(s))$. Here $\phi_0(s)$ is a reference phase point s with respect to the RF frequency. The non-zero longitudinal velocity spread in presence of electron beam experiences a cooling force that compresses the initial occupied intensity distributions. This leads to a narrower distribution than initial $\sim \cos^2 t$ distribution as shown in fig. 5.2. The observation of the signal shows emerging peaks in frequency domain at the higher order of the revolution frequency. Therefore, spectrum analyser in the *zero span mode* at $2f_{RF}$ was used to observe the longitudinal electron cooling.

The ion beam was in bunched configuration throughout the E_c search measure-

ment. However, electron beam was switched on after ~ 0.75 s to observe a clear signal. Fig. 5.3 shows the strongest signal at U_{cath} = - 30.65 V for electron current $I_e = 42.7\mu$A and magnetic expansion 20. The detailed study on electron cooling of HeH$^+$ ions and its characteristics, e.g. the cooling time (τ_{cool}), the size of cooled ion beam and comparision with theoretical predictions, will be presented another PhD work [66].

The electron density n_e and size of the beam r_{beam} in the interaction region are essential informations to calculate space charge U_{sc} of the beam and interaction length l_{int} (see sec. 4.2.2). At nominal magnetic expansion $\alpha = 20$ (see sec. 3.3), electron current I_e was continously measured in the main cup of the collector (shown as I_{mc} in fig. 5.1). The main cup of the collector also consists of a pin-hole to allow electron current (part of the beam) to be analysed. Based on steering the expanded beam in transverse horizontal and vertical directions over the main cup, a 2D current distribution was obtained as shown in fig. 5.4. The average height of the distribution after backgound correction is calculated. Then a cylinder volume of radius r_{cyl} is obtained after integrating the current distribution over each transverse points for the given average height. A magnetic field measurements and calculations revealed expansion factors of 8.9 and 21.5 in the collector and interaction region with respect
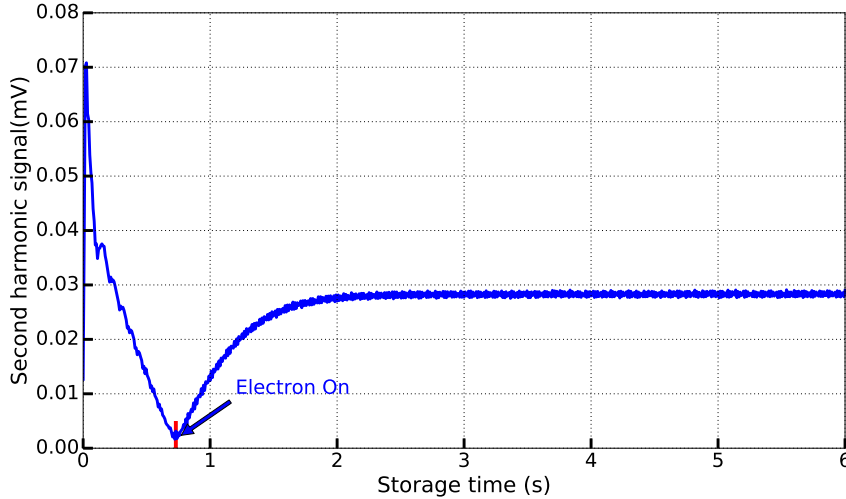
Figure 5.3: Second harmonic freqeuncy of RF signal as a function of storage time. When electron is on, signal can be seen rising due to the increase in bunch signal strength and it reaches equilibrum.

to gun side magnetic field. From this, the effective size of cathode is $r_{eff} = r_{cyl}/\sqrt{8.9}$ = 1.1(3) mm [66]. Also, the size of the electron beam in the interaction region is obtained as $r_{beam} = r_{eff}.\sqrt{21.5} = 5.1(14)$ mm.
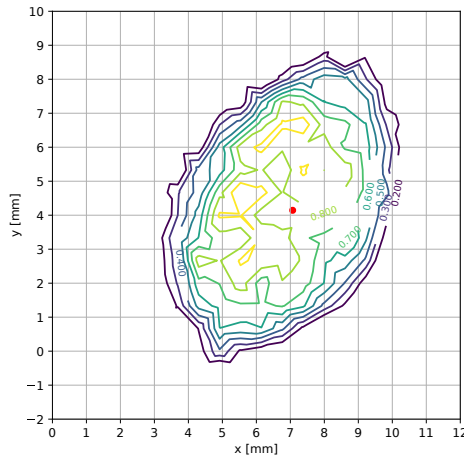
Figure 5.4: Illustration of a typical 2D electron current distribution at $I_e = 27$ μA. The red dot is the center of the distribution and average height is estimated from horizontal and vertical line current density through the center of the beam.

For U_{cath} = -30.65 V at $I_e = 42.7\mu$A, the space charge U_{sc} of the beam is 0.69 V and offset $W_c - W_a$ is -2.64 V. However, the collision experiments were perfomed at typical current, $I_e = 27$ μA with $U_{sp} = 0.43$ V. The space charge varies with changing electron energy for a fixed electron density. But the resulting error is very small if variation is neglected. Therefore, space charge variation is neglected in later sections.

Table 5.1: Table of experimental parameters for HeH$^+$ DR measurements with electron cooler.

E_i(keV)	E_c(eV)	I_e (μA)	$n_e(10^5)(cm^{-3})$	*Time* (s)	*Feature*
250	27.32	26(1)	6.4(4)	10.5-50	J-independent
250	27.32	52(1)	12.8(3)	0.1-45	J-dependent
125	13.67	18.4(1)	6.4(4)	10.5-50	Drift tube operation

The table 5.1 shows the typical experimental parameters at cooling energy for coasting ion beam during recombination measurement. The transverse and longitu-

dinal energy spread of photocathode is $k_B T_\perp = 1.65 \pm 0.35$ meV and $k_B T_\parallel = 100$ μeV and are assumed to be similar to a previous experiment [72]. Number of ions N_i was nearly 1×10^7 at the time of injection.

5.3 Electron cooler as target

In previous section, electron cooler as a tool for phase space cooling of bunched ion beam was presented. Here, we demonstrate the electron cooler device acting as target for HeH$^+$ ion-electron collision experiments. The detector signal at any given detuning energy E_d (see eqn. 3.12) is the sum of electron induced signal, residual gas induced, and the intrinsic dark count of the NICE detector. For N counts within time interval $\triangle t$, rate R is expressed as,

$$R(E_d) = \frac{N}{\triangle t} = \eta_e \alpha_{mb}(E_d, J) \frac{l_{int}}{C_0} N_i n_e(E_d) + \eta_p k_p \frac{l_p}{C_0} N_i n_p + R_{dark} \tag{5.2}$$

The first term is the electron induced term with $\alpha_{mb}(E_d, J)$ being the merged beams rate coefficient (see sec. 3.5.2) as function of detuning energy and internal state of the molecular ions. It has contribution from DR and DE signal and, it will be discussed later. $l_{int} N_i / C_0$ is the fraction of total number of ions in the interaction region of length l_{int} with C_0 being the total circumference of the CSR (see sec. 3.5.2). Moreover, n_e is the electron density and η_e is the collision event detection efficiency of the NICE.

The second term is due to inelastic collisions between residual gas and stored ions. In collision with residual gas, the ion can react through DE-type proces as

$$\text{HeH}^+ + R \longrightarrow \begin{cases} \text{He} + \text{H}^+ + R^{'} \\ \text{He}^+ + \text{H} + R^{'} \end{cases} \tag{5.3}$$

or by dissociative charge exchange (DCE).

$$\text{HeH}^+ + R \longrightarrow \text{He} + \text{H} + R^{'} \tag{5.4}$$

Previously measured cross section of DCE type reaction with H$_2$ molecules (main rest gas contribution at cryogenic temperature) after extrapolating up to 250 keV is $\sim$ one order of magnitude higher than DE-type [73]. Also, in our imaging measurement data $\sim$ 1.4 times more double neutral fragments than single neutral fragments have been observed and therefore, suggesting towards DCE type of mechanism [74].

In the second term of eqn. 5.2 the residual gas induced count rate is proportional to $(l_p/C_0)N_i$, fraction of ions in the interaction length l_p with n_p being the rest gas density. The interaction length l_p is different from l_{int} accounting for the fact that residual gas induced signal can occur roughly over the region between corner 2 and 3 (see fig.3.1). k_p is the rate coefficient for residual gas collisons induced signal and the corresponding count rate is defined as R_p. In addition, η_p is the residual gas event detection efficiency with single counting efficiency $p = 0.614 \pm 0.009$ [74]. Residual gas induced signal can be measured at electron beam off condition ($n_e = 0$) or with a suitable detuning energy at $n_e \neq 0$, where recombination is negligible.

We will use a measurement scheme to change the electron collision energy E_d and filter out the electron induced signal from the total count rate. Based on merged rate coefficient defined in eqn.3.29, the rate coefficient can also be defined with present relations in eqn. 5.2 as

$$\alpha_{mb}(E_d, J) = \frac{R(E_d) - R_p - R_{dark}}{C_i R_i n_e(E_d)}. \tag{5.5}$$

where R_p is the residual gas signal and R_i is the proxy signal for the number of stored ions N_i and C_i is the scaling factor l_{int}/C_0.

5.3.1 Measurement scheme for long storage time

To measure energy dependent rate coefficient α_{mb}, a well known method of energy wobble is used which has been succesfully employed in the previous DR investigations [14, 15, 72]. In this section, DR measurements of long storage time data of 10.5-50 s are presented. The injected ions are stored in the CSR without electron beam for the first 3 s. At the onset of 3 s, a sequence of *pre-cooling* steps of 100 ms time period starts and lasts up to 10.5 s.

To change the electron energy, a relatively fast and stable power supply U_{kep} is added to lift the voltage of cathode in addition to the U_0 power supply (see fig. 5.1). A USB-DAQ input, U_{ctrl} is used for fast switching with a range of $\pm$ 1. Here, U_{ctrl} = $\pm$ 1 correspond to U_{kep} voltage of $\pm$ 100V and negative input means acceleration to higher energy. Therefore, lab energy of electron beam is defined in the standard operation as $E_e = E_c - 10eV \times U_{ctrl}$.

The second part of the injection comprise of *cooling*, *measurement* and *reference* steps with a single cycle as shown in the fig. 5.5. Here, *cooling* step is 100 ms at $U_{ctrl} = 0$ to prepare ion beam in a well-defined state. In *measurement* step of 25
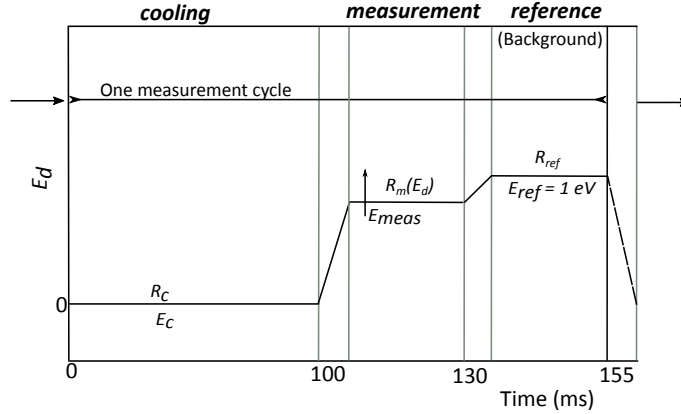
Figure 5.5: Measurement cycle for energy dependent rate measurments. The *cooling, measurement* and *reference* steps constitute one measurement cycle.

ms electron energy is changed to measure electron induced signal. And, last step is also 25 ms long *reference* always fixed at $U_{ctrl} = -1.147$ which is $E_d = 1.0$ eV, where electron induced signal is known to be very low [39]. Also, 5 ms is added in the begining of each energy step as a settling time for stable voltage condition. In the next measurement cycle electron energy is changed in *measurement* step with a small step in energy. In a typical complete energy scan there are 40-60 measurement cycles. In the end of the injection cycle ion and electron beams are off to measure R_{dark}. In one injection, typically 4-5 times such complete energy scan is possible and after completion of one injection it starts over.

Analysis

In the experimenal campaign, several meaurement runs of high resolution energy scans were performed. It was not possible to cover the complete energy ranging from sub-meV to 30 eV in one measurement run. Therefore, several piecewise runs of appropriate resolution were combined together. Each energy scan was analyzed independently. The count rate in each measurement step is defined as the ratio of number of events trigger to the integrated time in the step. The count rate in *cooling* step is defined as R_c. Similarly, the count rate in *measurement* step is R_m, similar to eqn 5.2 as residual gas induced background events also contributes. And, *reference* step count rate R_{ref} is similar to R_p due to very low cross section at $E_d = 1$ eV and therefore identical to electron beam off condition ($n_e = 0$). In addition, $R_{ref} - R_{dark}$ is also proportional to the number of stored ions and hence, can be used as proxy

signal for the number of ions.

The electron induced signal is obtained from $R_m - R_{ref}$. Based on above relations a relative merged beams rate coefficient can be defined as,

$$\alpha_{mb}^{rel}(E_d) = \frac{R_m(E_d) - R_{ref}(1 \text{ eV})}{R_{ref}(1 \text{ eV}) - R_{dark}} \tag{5.6}$$

The above defined relative rate coefficient can be scaled to the absolute rate coefficient measured at one energy for the complete energy spectrum.

Measurements were performed over several days, this could cause pressure fluctuations over different measurement runs which must be corrected. $R_c - R_{ref}$ is the background corrected electron signal measured at $E_d = 0$ and it should be nearly constant over different measurement for a fixed storage time. However, $R_{ref} - R_{dark}$ signal is susceptible to pressure change and therefore, we used their ratio shown below to correct for pressure fluctuations across different runs and the maximum correction factor was $\sim 18\%$ higher with respect to the stable measurement.

$$\alpha_{mb}(pressure) = \frac{R_c - R_{ref}}{R_{ref} - R_{dark}} \tag{5.7}$$

Amplitudes of combined runs visually confirmed to be matching after scaling. Moreover, the electron density decreases with increasing E_e and corresponding actual electron density can be calculated with the relation,

$$n_e(E_e) = n_e(E_c)\sqrt{\frac{E_c}{E_e}} \tag{5.8}$$

where E_e and E_c are the lab frame electron energies. Therefore, relative count rate α_{mb}^{rel} is scaled with factor $\sqrt{E_e/E_c}$ to maintain constant electron density condition across entire energy range. The count rate from several runs were combined to cover the whole energy range. A special variable binning was created to adapt the density of the measurement points to the observed structures in the spectrum and to a logarithmic energy scale. In this variable binning, histograms were filled with their corresponding weight. Weighted averaging was performed according to following formula:

$$\frac{\sum_i w_i x_i}{\sum_i w_i} \pm \left(\sum_i w_i\right)^{-\frac{1}{2}}, \quad w_i = \frac{1}{(\delta x_i)^2} \tag{5.9}$$

where x_i is relative rate $\alpha_{mb}^{rel}(E_d)$ and weighting factor w_i is the corresponding uncertainties.
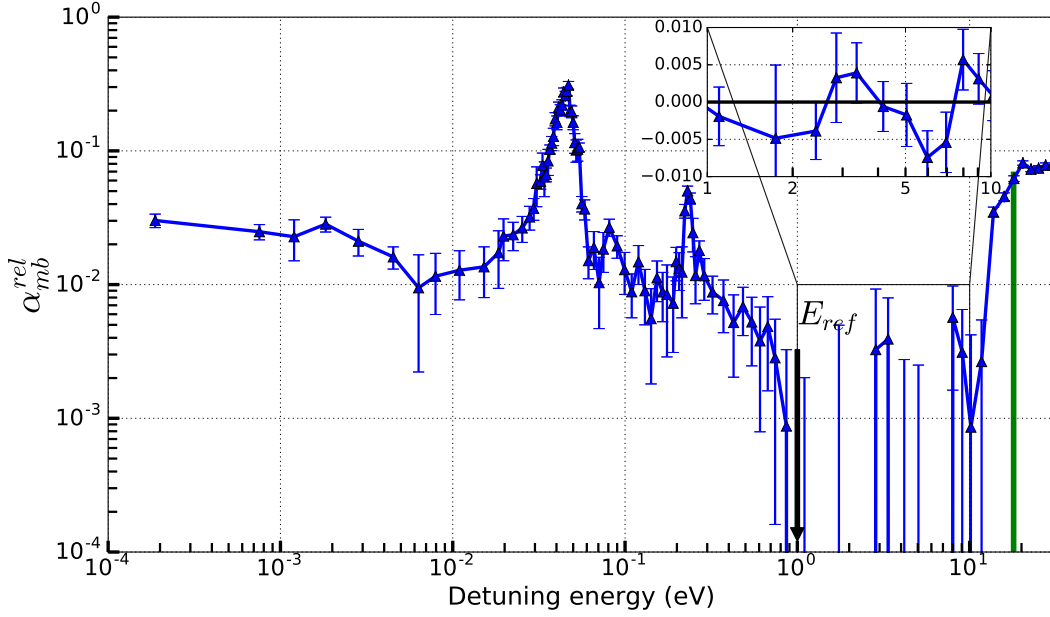
Figure 5.6: Relative merged beams rate coefficient at $E_i = 250$ keV and $I_e = 27$ μA for storage time of 10.5-50 s. Data points are normalized to the R_{ref} at $E_d = 1$ eV (shown with black arrow E_{ref}). Inset shows the some of the negative data points between 1-10 eV. The green vertical line corresponds to $E_d = 18$eV.

Fig. 5.6 shows the relative merged beams spectrum defined in eqn. 5.6 for storage time of 10.5-50 s. The spectrum shows several sharp structures and will be discussed later in absolute rate coefficient section. In 1-10 eV collision energy range some negative values are observed. This is due to small but non-zero cross section of the electron induced events at 1 eV. In sec. 5.4 we introduce a correction term to account for the electron induced signal at 1 eV.

5.3.2 Time dependent relative rate

In next measurement sequence, we performed a series of collision experiments to study the time evolution of the merged beams rate coefficient. In the storage time of 10.5-50 s, internal states of the molecule mainly, $J = 0$ and 1 with an average 86% relative population in $J = 0$ (see fig. 5.7). However, at short time interval $J = 1$ and higher J states are present in the system (see fig. 5.7). To measure the contribution of all internal states, storage time of 2 s up to 45 s have been used

without *pre-cooling* step. The measurement cycle consists of *cooling, measurement,* and *reference* steps similar to the previous measurement (see fig.5.5). However, they are shortend to 60 ms, 20 ms and 20 ms, respectively and electron energy in the *measurement* step remains same for a complete injection cycle and changes injection after injection. Also, this set of experiment was performed at high electron current, $I_e = 52\mu\text{A}$.
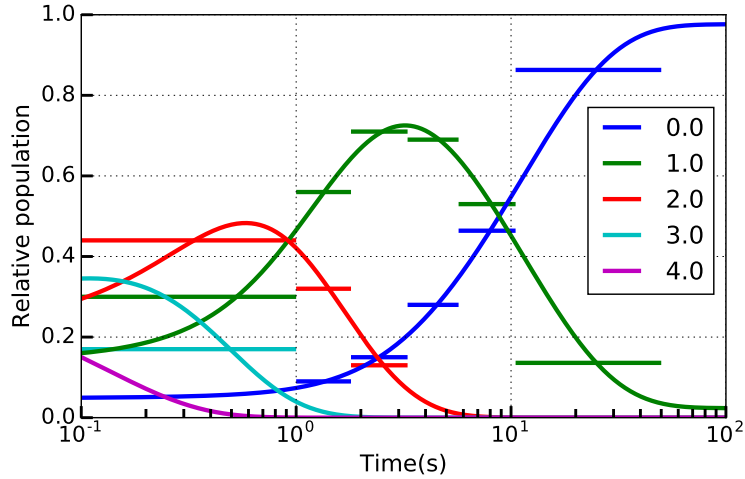
Figure 5.7: HeH$^+$ radiative cooling (see sec.2.4) with relevant J states (0-4 legends are J levels). Horizontal lines are time averaged relative rotational state population in time slices of 0.1-1 s, 1-1.8 s, 1.8-3.3 s, 3.3-5.7 s, 5.7- 10.5 s and 10.5-45 s, respectively.

The time slices of 0.1-1 s, 1-1.8 s, 1.8-3.3 s, 3.3-5.7 s, 5.7- 10.5 s and 10.5-45 s have been used to study the electron induced signal. The corresponding average relative population is shown with horizonatal lines in fig.5.7. The pressure fluctuation defined in eqn. 5.7 was again checked and found out to be nearly stable during the measurement. Therefore, individual measurement runs are not scaled. At short time slice, electron signal $R_m - R_{ref}$ should be corrected for the 20 ms delay between the two steps. The ion beam decays very fast in first few second and therefore *ref* signal should be scaled by a factor before subtraction. The scaling factor is 1.1 at 0.1 s and has been used, 1.0007 at 1 s which is small and we will neglect in further analysis. Furthermore, the relative rate coefficient defined in eqn. 5.6 is used to calculate the relative rate. Fig. 5.8 shows the relative rates in 6 time slices (see fig. 5.7). They are scaled by a common scaling factor of 0.53 obtained from comparing

the present measurement in the time slice of 10.5-45 s to the previous 10.5-50 s measurement accounting for 12.8×10^5 cm^{-3} and 6.4×10^5 cm^{-3} electron density. Each time sliced relative rate is overlaid with time independent relative rate to show the comparision of time evolution.
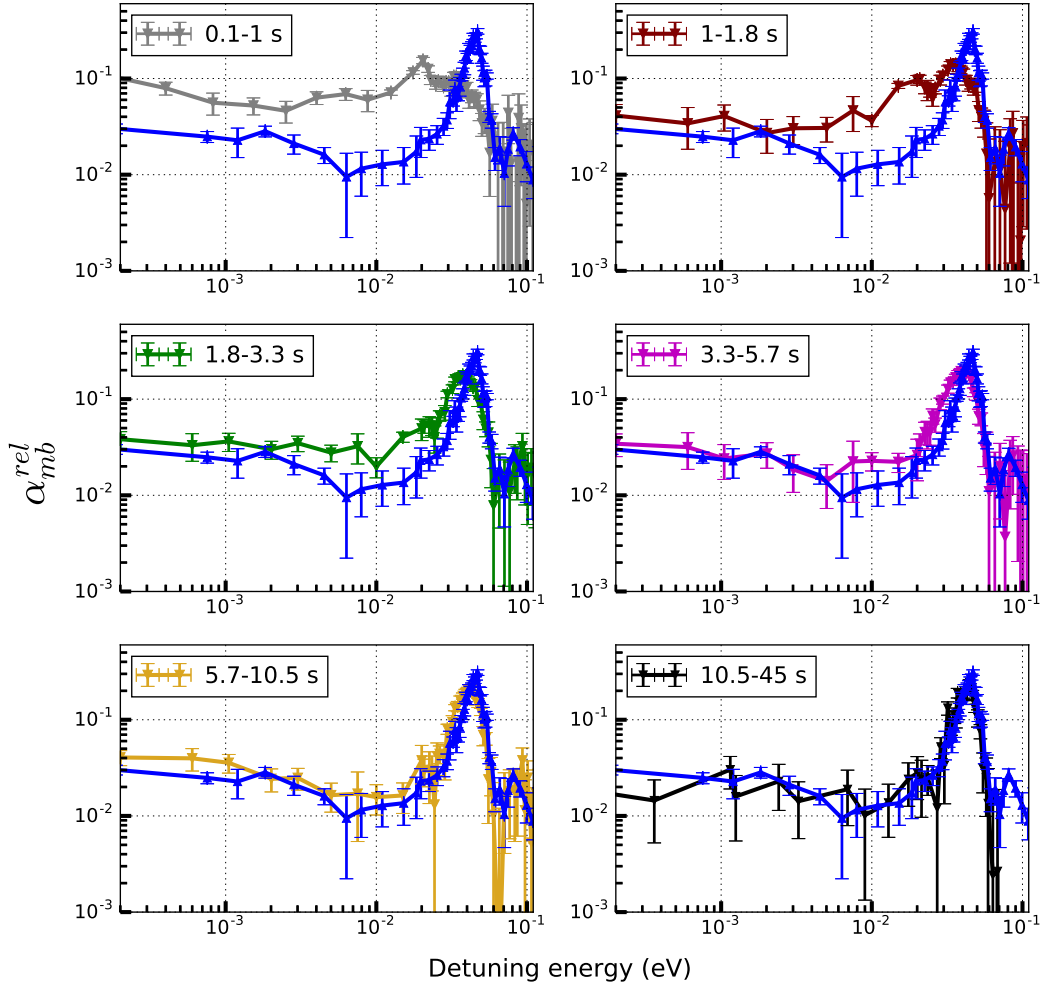
Figure 5.8: Time dependent relative rate coefficient at 6 storage time slices at $I_e = 52\mu$A. The common blue curve is the relative rate of long storage time (see fig. 5.6). All relative rates are scaled by 0.53 to match the long storage measurement.

5.3.3 Drift tube operation

In the previous section, experiments were performed with grounded drift tubes in the interaction section (see fig. 5.1). However, electron cooler is also designed to perform phase space cooling and collision experiments with drift tube lifted to a finite potential and decelerate the electron beam to velocity matched condition and to well a defined collision energy (see sec. 4.4).
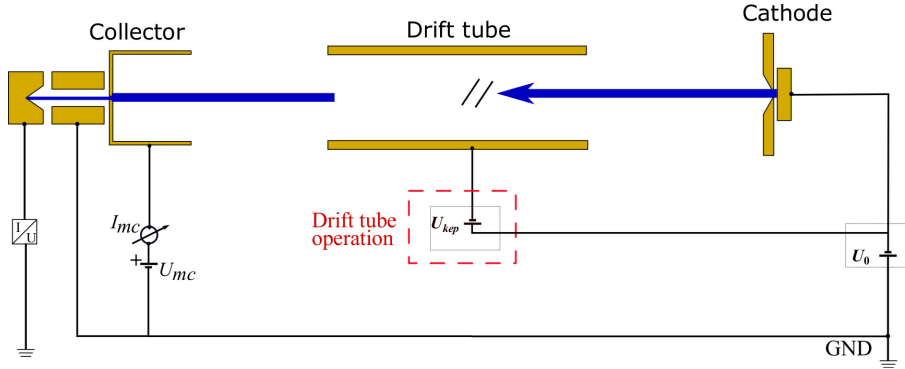
Figure 5.9: Electronic circuit used in drift tube operation. U_{kep} directly controls the drift tube potential and cathode stays at static and higher volatge U_{cath} controlled by U_0. The electron current I_e is measured in the main cup of the collector as I_{mc}.

In this section, a comparative study of standard operation and drift tube operation of the electron cooler is presented at ion beam energy $E_i \approx 125$ keV. The corresponding velocity matched energy, $E_c = 13.67$ eV is again calculated from the revolution frequency of stored HeH$^+$ ions which is $f_0 = 62.451$ kHz (see sec. 5.1). Measurements were again performed at long storage time 10.5-50 s with measurement scheme, duration of steps, and electron density similar to the long storage time measurement at 250 keV ion beam energy (see sec. 5.3.1). In drift tube operation, cathode potential U_{cath} controlled with U_0 is always set to a higher static potential than cooling potential (see eqn. 4.10). The drift tube potential is defined with U_{kep} which is added to U_0. The USB-DAQ controlled U_{ctrl} is used to control U_{kep} to change electron beam energy in the interaction section. The electron energy in the center of the interaction region is defined as,

$$E_e(D) = -eU_{cath} + W_c - (e(-U_{cath} - U_{kep}) + W_a) - eU_{sc} \tag{5.10}$$

where sum of work function difference and space charge of the beam is defined as $\triangle$. Therefore, electron energy in drift tube mode is given by $E_e(D) = eU_{kep} + \triangle$

= e(-10×U_{ctrl}) + △. And electron beam energy in standard operation is given by $E_e(standard) = E_c$ - 10×U_{ctrl} (see sec. 5.3.1). The relative rate coefficient defined previously is also used here to calculate electron induced signal (see sec. 5.3.1).
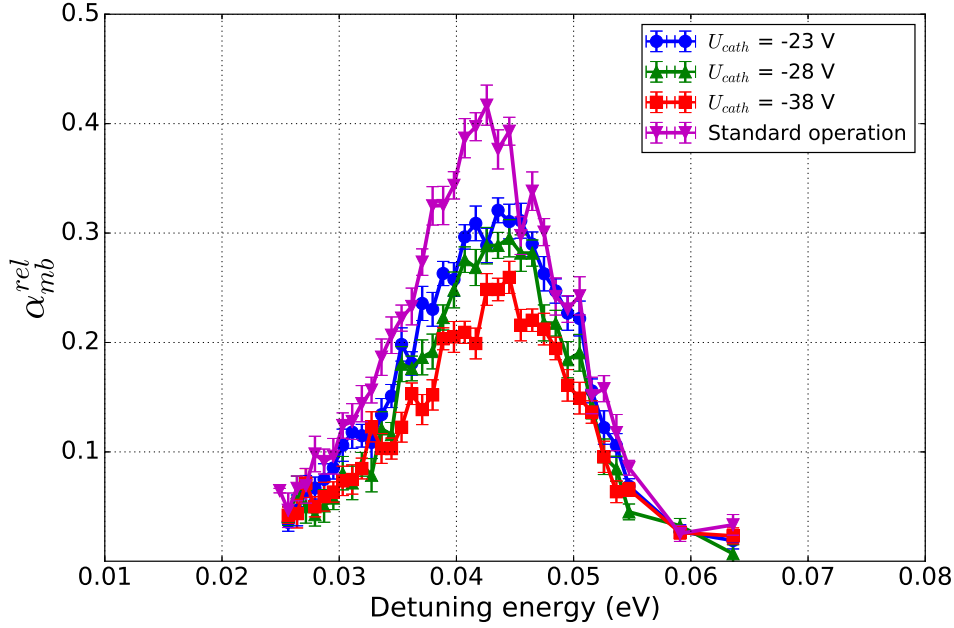
Figure 5.10: Comparision of merged beams relative rate spectra of standard operation and drift tube operation at $E_c = 13.67$ eV with $I_e = 18.4$ μA. For drift tube mode $U_{cath} = -23$ V, -28 V and -38 V, respectively were used.

As illustrated in sec.4.6 at given detuning energy the peak amplitude of rate coefficient of a delta-function cross section in drift tube operation is lower than corresponding standard operation. HeH$^+$ relative DR spectrum has sharpest peak near $E_d = 44$ meV in the $25-65$ meV region (see fig.5.6). Therefore, we also scanned the drift tubes potential within this energy range to study the effect of electron beam deceleration on peak position and amplitude of the peak. Fig.5.10 shows the overlaid relative merged beams rate coefficient for drift tube operation and standard operation. In drift tube operation $U_{cath} = -23$ V, -28 V and -38 V were used and the position of peak remains nearly at same position as in the standard operation.
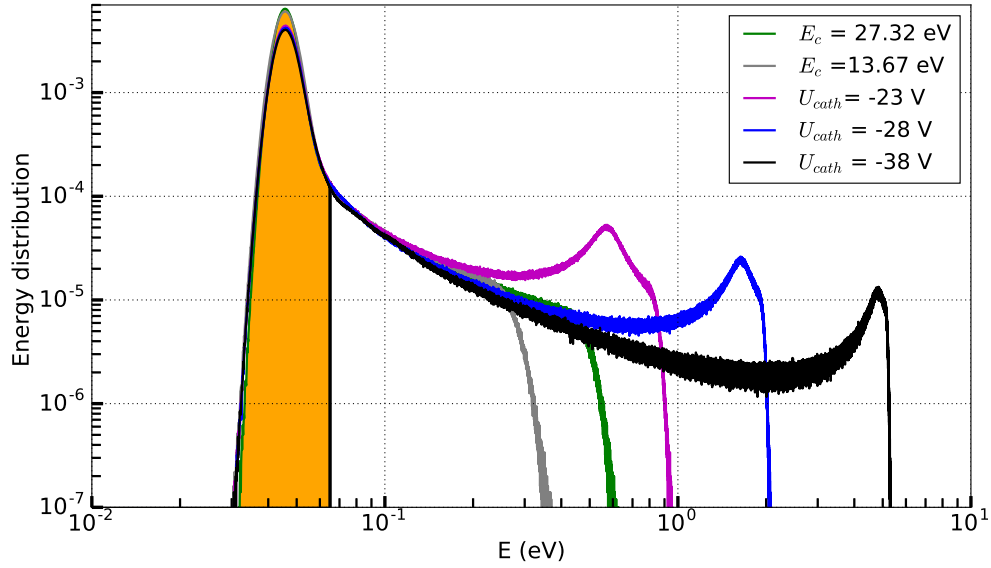
Figure 5.11: Comparision of energy distribution in standard operation and drift tube operation at $E_d = 44$ meV for $E_c = 13.67$ eV. The total interaction length l_{int} is 1127 mm. In drift tube operation $U_{cath} = -23$ V, -28 V and -38 V, respectively were used. The thermal energy spread of the electron beam are $k_B T_\perp = 2$ meV and $k_B T_\parallel = 125$ μeV and 100 μeV at $E_c = 13.67$ eV and 27.32 eV (see eqn. 3.7), respectively. The orange shaded region is the 30-65 meV range used in the energy distribution integration. The integrated values are 0.9, 0.68, 0.65 and 0.62 in standard operation and in drift tube operation at $U_{cath} = -23, -28, -38$ V, respectively. The energy distribution of $E_c = 27.32$ eV is also shown and it will be used in sec. 5.4.

In addition, $l_{eff}(E_d)$ defined in sec. 3.5.2 and shown in sec.4.6, the straight part of the overlap geometry of total length l_{int}, is different in standard and drift tube operations (see fig.4.24). It is possible to scale the drift tube operation relative rate to the standard operation. Therefore, the ratio of l_{eff} in standard and drift tube operation, $(l_{eff}(\text{standard})/l_{eff}(\text{drift tube}))$ is used to calculate scaling factor from the energy distribution function in standard operation and in drift tube operation at $E_c = 13.67$ eV. Fig. 5.11 shows the typical lowering of amplitude of energy distribution at $E_d = 44$ meV. The calculated scaling factor are 1.33, 1.38 and 1.44 for $U_{cath} = -23$ V, -28 V and -38 V, respectively. Fig. 5.12 shows scaled relative

rates in drift tube operation show reasonable agreement with the standard operation within the uncertainty limit. Therefore, it demonstrates that the additional effect of the deceleration of electron beam in drift tube operation in an experiment can be corrected and, hence, similar results as in the standard operation can be obtained. It will be very useful especially in case when electron density is limited in standard operation (see sec.4.4).
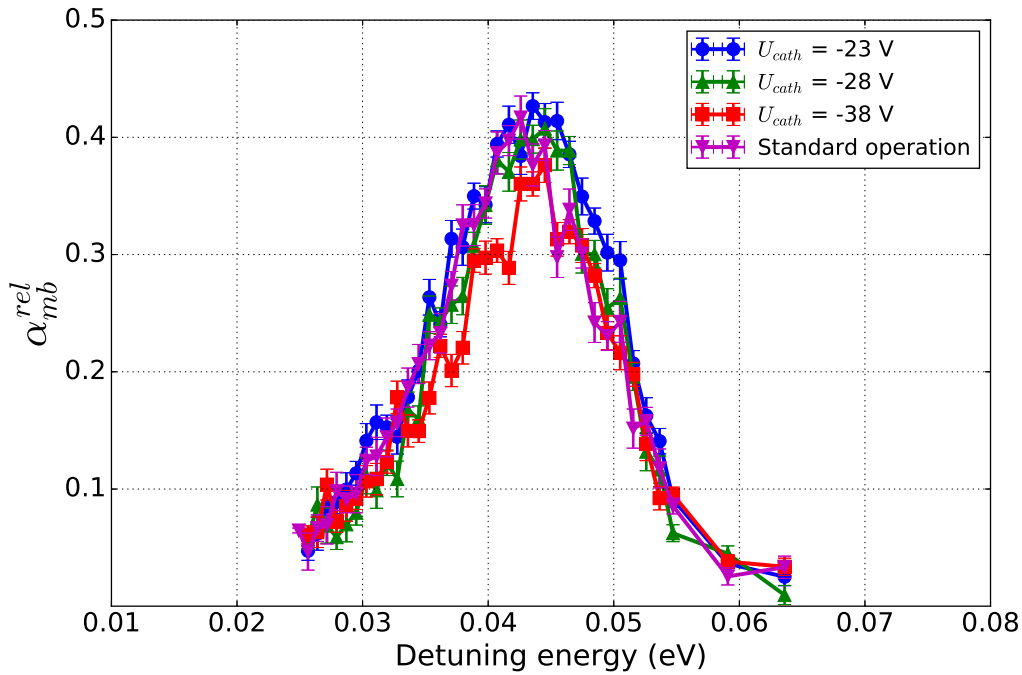
Figure 5.12: Scaled relative rate spectra of standard operation and drift tube operation at $E_i = 125$ keV and $E_c = 13.67$ eV with $I_e = 18.4$ μA. For drift tube mode $U_{cath} = -23$ V, -28 V and -38 V, respectively were used.

Moreover, the present relative rate at $E_i = 125$ keV should be compared with the 250 keV relative rate. The peak amplitude in both cases are diferent (higher at $E_i = 125$ keV) and also, the peak position at $E_i = 250$ keV is at slightly higher detuning energy. This will be further studied in near future in more systematic manner.

5.4 Absolute rate coefficient measurement

In previous DR measurements at TSR storage ring, the ion beam lifetime method was used to determine absolute rate coefficient based on the work of Pedersen et al.[15]. In this method the ion beam decay at fixed electron energy is measured with electron beam being on and off within one injection. Assuming an exponential decay in both cases it is possible to extract the absolute rate coefficient from the inverse difference of two decay constants. However, we observed that the electron beam off condition during ion beam storage could not be realized for any given ion injection in the CSR. This is likely due to the incoherent tune shift of the CSR [75]. Therefore, unfortunately we could not rely on the ion beam lifetime method for absolute rate coefficient determination.

Absolute rate coefficient at 18 eV

Another independent method of absolute rate coefficient determination depends on knowing the individual terms in eqn. 5.5. The DR rate coefficient in the high-energy region of the spectrum is independent of rotational relaxation due to the direct DR mechanism (see sec. 2.3). This leads to count rates independent of the storage time. Therefore, we choose to calculate α_{mb} at $E_d = 18$ eV for absolute scaling purpose. The electron induced count rate at $E_d = 18$ eV is,

$$R_m(18 \text{ eV}) - R_{ref} = (43.2 \pm 3.8) \text{ s}^{-1} \tag{5.11}$$

The number of ions, N_i is generally calculated from the current pick-up measurment of ion beam in RF-bunched configuration at the time of injection. However, we are interested in N_i during the measurement period of 10.5-50 s and current pick-up cannot be used for several second due to fast decaying signal. Therefore, current pick-up signal at short storage time (up to 0.1 s) and NICE detector measuring R_{ref} signal at later time were combined together. When the measured ion number was scaled from initial to later time using the measured count rates, $N_i = (1.2 \pm 0.2) \times 10^6$ was obtained [76]. The estimated error of ~ 17 % is from the calibration of current pick-up and statistical uncertainty of the count rate.

The calculated NICE detector counting efficiency from imaging of the neutral fragments was $p = 0.617 \pm 0.009$ [74]. The probability of getting at least one neutral fragment in the case of DR is given by

$$\eta_e = p^2 + 2p(1 - p) = 0.853 \pm 0.007 \tag{5.12}$$

where p^2 is the probability of both H and He fragments hitting and creating counting pulses on the detector. In addition, $p(1-p)$ corresponds to H fragment hitting and He missing and $(1-p)p$ is H fragment missing and He hitting the detector.

The electron density at $E_d = 18$ eV is calculated from the relation, $n_e(18 \text{ eV}) = n_e(E_c)\ \sqrt{E_c/E_e}$ (see eqn. 5.8). The electron current during measurement is $I_e = (26 \pm 1)\ \mu$A and the density at cooling is $n_e = (6.4 \pm 0.4) \times 10^5$ cm^{-3}. Thus, the scaled electron density at $E_d = 18$ eV is,

$$n_e(18 \text{ eV}) = (3.5 \pm 0.2) \times 10^5 \text{cm}^{-3}. \tag{5.13}$$

The interaction length l_{int} is calculated using eqn. 4.4 for the electron beam of radius 5.1 mm. The determined value is (1.127 ± 0.003) m (see eqn. 4.4) and the CSR circumference, $C_0 = (35.12 \pm 0.05)$ m. The uncertainty in interaction length is due to the propagated error from the estimated cathode radius.

Based on the above calculated individual terms, the absolute rate coefficient at $E_d = 18$ eV is,

$$\alpha_{mb}^{abs}(18 \text{ eV}) = (3.76 \pm 0.74) \times 10^{-9} \text{ cm}^3\text{s}^{-1} \tag{5.14}$$

Absolute rate coefficient

We then obtain a scaling factor, f_{abs} defined as the ratio of absolute and relative rate coefficient at 18 eV (see fig. 5.6).

$$f_{abs} = \frac{\alpha_{mb}^{abs}(18 \text{ eV})}{\alpha_{mb}^{rel}(18 \text{ eV})} = 6.05 \times 10^{-8} \tag{5.15}$$

The relative rate coefficients $\alpha_{mb}^{rel}(E_d)$ (see eqn. 5.6) can be scaled by f_{abs} to obtain the absolute rate coefficient also this has an uncertainty. Furthermore, as already shown in fig. 5.6 in the collision energy range of 1-10 eV some negative relative rates due to finite electron induced rates at $E_d = 1$ eV have been observed. Therefore, we need to add the absolute rate coefficient of 1 eV as correction term. Previously measured absolute rate e.g. from CRYRING measurement [37] could not be used directly due to the fact that in the CRYRING electron cooler overlap geometry is different. Therefore, deconvolution procedure developed earlier by Novotny et al. [72] has been employed to calculate cross section based on known overlap geometry of the CRYRING electron cooler and thermal energy spread etc. The obtained cross section is then convolved with the collision velocity and energy distribution and at

1eV rate coefficient is $\alpha_{mb}^{corr}(1 \text{ eV}) = 1.3 \times 10^{-10} \text{ cm}^3\text{s}^{-1}$ [76]. Hence, absolute merged beams rate coefficient for the whole collision energy range after correction is,

$$\alpha_{mb}^{abs}(E_d) = f_{abs}\alpha_{mb}^{rel}(E_d) + \alpha_{mb}^{corr}(1 \text{ eV}) \tag{5.16}$$

Rescaled rate coefficient

Moreover, it has been already illustrated that the rate coefficient of a narrow-width cross section is lowered due to elevated collision energy over a significant part of a the full overlap geometry of length l_{int} (see sec. 4.6). Consequently, the straight region l_{eff} is shorter and experimentally obtained rate coefficient is proportional to the l_{eff}. Also, the cross section peak position changes the l_{eff} which in turn changes the rate coefficient (see fig. 4.24). Therefore, the experimentally obtained rate coefficient α_{mb}^{abs} should in principle be rescaled as,

$$\alpha_m(E_d) = \frac{l_{int}}{l_{eff}(E_d)}\alpha_{mb}^{abs}(E_d). \tag{5.17}$$

The HeH$^+$ energy spectrum has two prominent peaks at ~ 44 meV and ~ 0.23 eV, respectively. Since the two peak positions are very close and decrease in α_{mb}^{abs} is higher at 44 meV than 0.23 eV peak and therefore, we should consider one rescaling factor for the energy range up to 1 eV. Moreover, 18 eV peak is nearly 10 eV broad, and the l_{eff} is also very nearly same as l_{int} in this energy region, therefore we will not rescale after 1 eV. We decide here to rescale the rate coefficient by a factor of $l_{int}/l_{eff}(44meV) = 1.15$
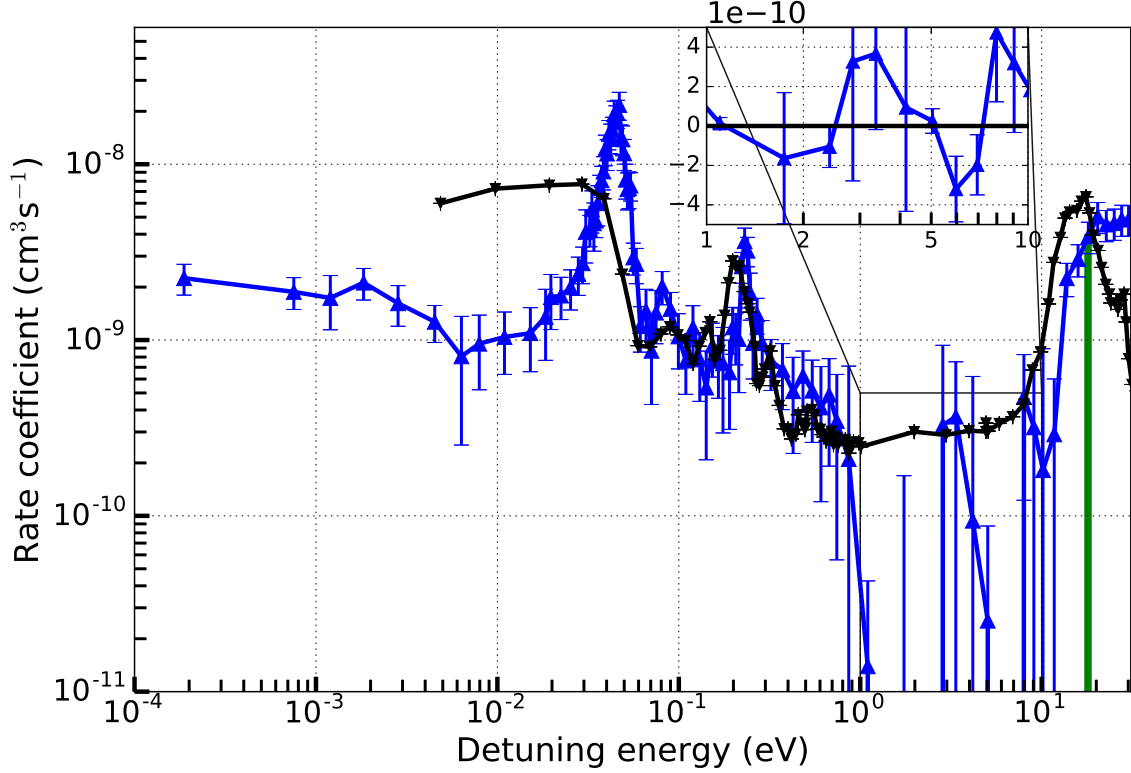
Figure 5.13: Rescaled absolute merged beams rate coefficeint of HeH$^+$ ion in 10.5-50 s. The data has 1σ statistical uncertainty and the absolute scaling uncertainty is $\pm 20\%$. At the start of this time window rotational state $J = 0$ is more than 50 % populated (see fig. 2.7) and increases further while $J = 1$ state vanishes. Up to 1.8 eV the spectrum represents DR rate coefficient for $J = 0$ state and after 1.8 eV it consists of DR (direct DR) and DE rate coefficients (see text below). Inset shows the rate coefficient in 1-10 eV after correction still has some negative values. Green vertical line is at $E_d = 18$ eV. The black spectrum is the 300 K absolute DR rate coefficient [37]. The features of the spectrum are discussed in the text below.

5.5 Discussion of the rate coefficient

The observed features of the rescaled rate coefficient shown in fig. 5.13 are following:

5.5.1 Low energy region

In the low energy region, DR is due to the indirect mechanism (see sec. 2.3) where initial ro-vibrational state of the ion plays a role as can be seen from difference in spectrum of the present measurement and 300 K measurement [37] shown in fig. 5.13. From radiative cooling model, time averaged population of $J=0$ state between 10.5-50 s is $\sim 86\%$ (see fig. 5.7). The CRYRING measurement represents the thermal equilibrated rotational state averaged DR rate coefficient at 300 K. Hence, the enhanced DR rate in the first few meV energy range in the CRYRING measurement is due to the contributions from several J-states with only 15 % relative population in $J = 0$ state. In 0.1-1 eV energy range the DR rate coefficient is nearly in aggreement with the room temperature mesurement. The discrepancy in amplitude is mainly due to the different $J = 0$ level populations. In our measurement the peak near 44 meV is the feature of $J = 0$ rotational state. It has also been predicted in the theoretical calculation and attributed to the neutral vibrationally excited Rydberg states converging to the vibrational levels of the HeH$^+$ ion [41, 77]. Fig. 5.14 shows the overlaid curves of simulated rate coefficient obtained after convolution of theoretical cross section and relative velocity with the energy distribution function in the standard operation (see eqn. 4.20) [41]. The simulated rate coeffcient is scaled to match the amplitude of the experimental rate coefficient. It looks similar to the experimentally measured rate coefficient near 44 meV peak but however, rate coefficient amplitude below 3 meV does not match.

Moreover, the rate in 1-10 eV is of the order of 10^{-2} of the maximum observed DR rate. As expected, at the given uncertainty of the count rates, still some negative measurement results remain in the range of 1-10 eV, as shown in fig. 5.13.
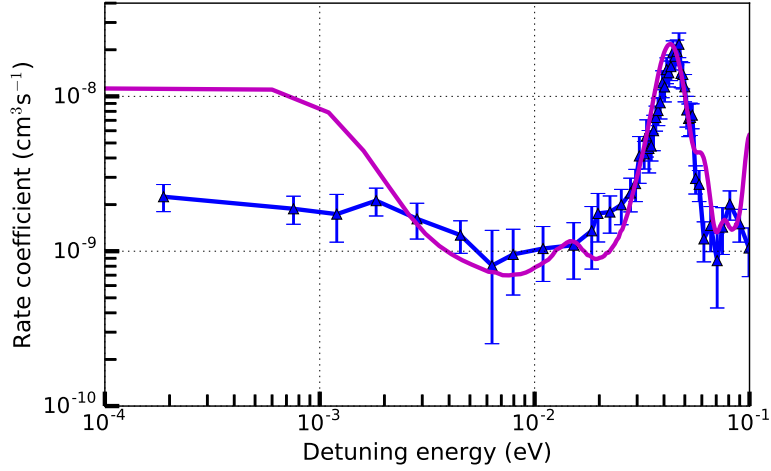
Figure 5.14: Illustration of simulated rate coefficient for $J = 0$ rotational state at $E_c = 27.32$ eV with $k_B T_\parallel = 100$ μeV and $k_B T_\perp = 2$ meV.

5.5.2 Storage time dependence

We will also explore the origin of 44 meV peak with storage time dependent relative rate coefficient already introduced in sec. 5.3.2. The corresponding absolute time dependent rate coefficient is also calculated using eqn.5.16 and eqn. 5.17 and shown in fig. 5.15. In the first time slice of 0.1-1 s, the DR rate is dominantly averaged over rotational states $J = 2$, 1 and 3 with $\sim 45\%$, $\sim 30\%$ and $\sim 15\%$ relative populations, respectively and therefore, the peak at 44 meV does not exist. Moreover, the rate coefficient nearly matches to the CRYRING measurement at 300 K (shown in black). In 1-1.8 s $J = 1$ and 2 states are dominant and a broad and energy shifted peak appears. The rate coefficient in 0.1-10 meV range decreases with increasing time slices. The amplitude and shape of the 44 meV peak increases and becomes narrower with increasing relative population in $J = 0$ states. Therefore, the above time dependent spectra together with the rotational cooling model proves the origin of peak and lower rate coefficient below 44 meV.
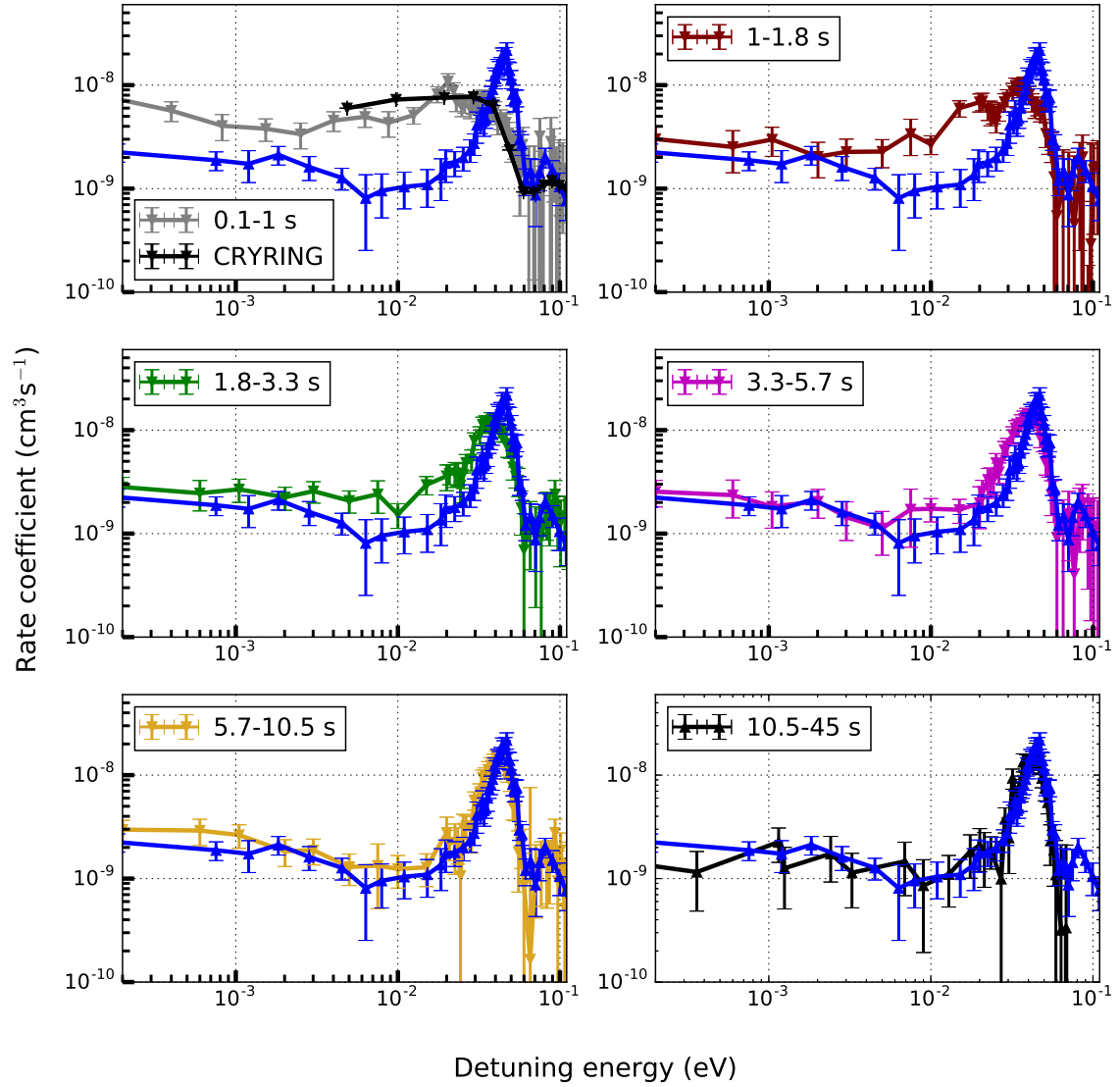
Figure 5.15: Comparision of the rotationally relaxed DR rate coefficient to the time dependent rotationally excited DR rate in time slices of 0.1-1, 1-1.8 s, 1.8-3.3 s, 3.3-5.7 s, 5.7-10.5 s and 10.5-45 s, respectively where $J = 3, 2$ and 1 are also populated (see fig. 5.7).

5.5.3 Influence of DE

In fig. 5.13 spectrum also consists of DE signal after 1.8 eV due to the fact that the MCP-based detector could not distinguish in case of a single fragment originating from DR or DE and also, multiplicities could not be resolved due to very short time of flight difference of 6-8 ns. Therefore, in 10-30 eV region DR peak could not be observed and a broad increasing in amplitude shoulder including DR and DE events is observed. Moreover, DR cross section after 18 eV peak has decreasing amplitude while DE cross section for H and He$^+$ channel has rising amplitude after 18 eV and therefore, it is has main contribution to the observed shape [37].

5.6 Summary

In the present experiment electron cooler has been used as target to study dissociative recombination of HeH$^+$ ions with electrons. The absolute rate coefficient of the ro-vibrationally relaxed HeH$^+$ ion has been measured in a cryogenic environment. Also, the drift tubes in the interaction region has been successfully used during the experiment. The method of scaling between standard operation and drift tube operations has also been shown.

6 Conclusion and Outlook

In this work the low energy CSR electron cooler as target for electron-ion collision experiments is modelled and related experiments are performed. The electron cooler is designed to operate in standard and drift tube configurations. In standard configuration, the cathode potential drives the electron beam acceleration and defines average relative velocitiy between electron and ion merged beams. In another configuration the difference between the cathode potential and the drift tubes in the interaction region defines the electron beam energy, both in the laboratory frame and as relative collision energy with respect to the ions. This later mode is especially important in electron cooling and collision experiments at collision energies below 10 eV. The numerically calculated overlap of the phase space cooled ion beam and the magnetically expanded electron beam shows that the electron beam is bent in the merging regions which in turn gives rise to collision energies elevated up to eV range as a function of position along the ion beam axis.

The modelled collision energy distributions in both configurations at given detuning energy show higher energy spread for the drift tube configuration. The energy distribution broadening by the overlap geometry and the drift tube potential has been studied with simulated rate coefficient based on delta function cross section at several detuning energies. The influence in both configurations is observed to be highest in the low energy region and to be changing with detuning energy. Also, it is proportional to the effective straight region of the full overlap geometry. Therefore, a method has been developed to correct the obtained rate coefficient based on the theoretical energy-integrated rate coefficient. In electron-ion collision experiments, especially in DR, narrow-width peaks occur at low collision energies. Thus, the method employed in the model provides a framework to correct experimentally obtained rate coefficient for the beam overlap limits of known geometries of magnetically expanded electron beam and known detuning energy.

In the second part dissociative recombination of ro-vibrationally cold HeH^+ ions at 250 keV is investigated in the collision energy range of 0.2 meV-30 eV. The absolute rate coefficient is rescaled at 44 meV peak with the method given in the model.

With the time dependent DR rate coefficients the radiative cooling model, it is shown that the contribution from higher rotational states decreases with storage time. Moreover, the time dependent scaled rate coefficient in short time scale when higher rotational states are present is nearly equivalent to the previously measured room temperature absolute rate coefficient.

Furthermore, a drift tube configuration has also been realized for the first time for the collision experiments at 125 keV ion beam energy. The electron energy scanning was performed at three different cathode voltages and the obtained relative rate coefficients were also scaled based on the method developed earlier.

Outlook

The CSR electron cooler has been successfully operated in standard and drift tube configurations in the first cold DR measurement on HeH^+ ions. This opens opportunities to study the electron-ion collision experiments at new time scales and thus enable measurements of ro-vibrationally resolved DR spectra. However, one of the most important near future goal is to study drift tube operation in more systematic manner to understand and address the remaining small differences discrepancies observed between 125 keV and 250 keV HeH^+ measurements.

In principle, infrared active hydride ions are the natural candidates for future experimental studies. For all types of ions, the electron induced rotational excitation and de-excitation is another important reaction in the interstellar medium. In future storage ring experiments, it can also be studied for two isotopes e.g. H_2^+ (not IR active) and HD^+.

List of Figures

List of Tables

101

Bibliography

[1] A. G. G. M. Tielens, "The molecular universe", in: *Rev. Mod. Phys.* **85** (3 2013), pp. 1021–1081, DOI: `10.1103/RevModPhys.85.1021`.

[2] T. Hartquist and D. A. Williams, *The chemically controlled cosmos*, Cambridge University Press, 2008.

[3] K. P. Kirby, "Ionic processes in astrophysics", in: *Physica Scripta* **1995**. (1995), p. 59.

[4] I. W. Smith, C. S. Cockell, and S. Leach, *Astrochemistry and astrobiology*, Springer Science & Business Media, 2012.

[5] E. Herbst and E. F. Van Dishoeck, "Complex organic interstellar molecules", in: *Annual Review of Astronomy and Astrophysics* **47** (2009), pp. 427–480.

[6] H. S. Müller, F. Schlöder, J. Stutzki, and G. Winnewisser, "The Cologne Database for Molecular Spectroscopy, CDMS: a useful tool for astronomers and spectroscopists", in: *Journal of Molecular Structure* **742**. (2005), MOLECULAR SPECTROSCOPY AND STRUCTURE, pp. 215–227, DOI: `https://doi.org/10.1016/j.molstruc.2005.01.027`.

[7] A. Florescu-Mitchell and J. Mitchell, "Dissociative recombination", in: *Physics Reports* **430**. (2006), pp. 277–374, DOI: `https://doi.org/10.1016/j.physrep.2006.04.002`.

[8] M. Larsson and A. E. Orel, *Dissociative Recombination of Molecular Ions*, Cambridge Molecular Science, Cambridge University Press, 2008, DOI: `10.1017/CBO9780511535406`.

[9] R. W. and D. A., "The formation and destruction of HeH$^+$ in astrophysical plasmas", in: *Astrophys. J.* **255** (1982), p. 489.

[10] Bovino, S., Tacconi, M., Gianturco, F. A., and Galli, D., "Ion chemistry in the early universe - Revisiting the role of HeH+ with new quantum calculations", in: *A&A* **529** (2011), A140, DOI: `10.1051/0004-6361/201116740`.

[11] D. Galli and F. Palla, "The dawn of chemistry", in: *Annual Review of Astronomy and Astrophysics* **51** (2013), pp. 163–206.

[12] S. Lepp, P. Stancil, and A. Dalgarno, "Atomic and molecular processes in the early Universe", in: *Journal of Physics B: Atomic, Molecular and Optical Physics* **35**. (2002), R57.

[13] R. Güsten, H. Wiesemeyer, D. Neufeld, K. M. Menten, U. U. Graf, K. Jacobs, B. Klein, O. Ricken, C. Risacher, and J. Stutzki, "Astrophysical detection of the helium hydride ion HeH+", in: *Nature* **568**. (2019), p. 357.

[14] Z. Amitay, D. Zajfman, P. Forck, U. Hechtfischer, B. Seidel, M. Grieser, D. Habs, R. Repnow, D. Schwalm and A. Wolf, "Dissociative recombination of CH^+: Cross section and final states", in: *Phys. Rev. A* **54** (1996), p. 4032.

[15] H. B. Pedersen, H. Buhr, S. Altevogt, V. Andrianarijaona, H. Kreckel, L. Lammich, N. de Ruette, E. M. Staicu-Casagrande, D. Schwalm, D. Strasser, X. Urbain, D. Zajfman, and A. Wolf, "Dissociative recombination and low-energy inelastic electron collisions of the helium dimer ion", in: *Phys. Rev. A* **72** (1 2005), p. 012712, DOI: 10.1103/PhysRevA.72.012712.

[16] J. Semaniak, S. Rosén, G. Sundström, C. Strömholm, S. Datz, H. Danared, M. af Ugglas, M. Larsson, W. J. van der Zande, Z. Amitay, U. Hechtfischer, M. Grieser, R. Repnow, M. Schmidt, D. Schwalm, R. Wester, A. Wolf, and D. Zajfman, "Product-state distributions in the dissociative recombination of $^3HeD^+$ and $^4HeH^+$", in: *Phys. Rev. A* **54** (6 1996), R4617–R4620, DOI: 10.1103/PhysRevA.54.R4617.

[17] P. Baumann, M. Blum, A. Friedrich, C. Geyer, M. Grieser, B. Holzer, E. Jaeschke, D. Krämer, C. Martin, K. Matl, R. Mayer, W. Ott, B. Povh, R. Repnow, M. Steck, E. Steffens, and W. Arnold, "The Heidelberg Heavy Ion Test Storage Ring TSR", in: *Nuclear Instruments and Methods in Physics Research Section A: Accelerators, Spectrometers, Detectors and Associated Equipment* **268**. (1988), pp. 531–537, DOI: https://doi.org/10.1016/0168-9002(88)90573-6.

[18] R. Stensgaard, "ASTRID - The Aarhus Storage Ring", in: *Physica Scripta* **T22** (1988), pp. 315–317, DOI: 10.1088/0031-8949/1988/t22/051.

[19] K. Abrahamsson, G. Andler, L. Bagge, E. Beebe, P. Carlé, H. Danared, S. Egnell, K. Ehrnstén, M. Engström, C. Herrlander, J. Hilke, J. Jeansson, A. Källberg, S. Leontein, L. Liljeby, A. Nilsson, A. Paal, K.-G. Rensfelt, U. Rosengård, A. Simonsson, A. Soltan, J. Starker, M. Ugglas, and A. Filevich, "CRYRING — a synchrotron, cooler and storage ring", in: *Nuclear Instruments and Methods in Physics Research Section B: Beam Interactions with Materials and Atoms* **79**. (1993), pp. 269–272, DOI: https://doi.org/10.1016/0168-583X(93)95341-2.

[20] G. I. Budker and A. N. Skrinskii, "Electron cooling and new possibilities in elementary particle physics", in: *Phys. Usp.* **21**. (1978), pp. 277–296, DOI: 10.1070/PU1978v021n04ABEH005537.

[21] S. P. Møller, "ELISA, and electrostatic storage ring for atomic physics", in: *Nuclear Instruments and Methods in Physics Research Section A: Accelerators, Spectrometers, Detectors and Associated Equipment* **394**. (1997), pp. 281–286, DOI: https://doi.org/10.1016/S0168-9002(97)00673-6.

[22] D. Zajfman, A. Wolf, D. Schwalm, D. A. Orlov, M. Grieser, R. von Hahn, C. P. Welsch, J. R. C. Lopez-Urrutia, C. D. Schröter, X. Urbain, and J. Ullrich, "Physics with colder molecular ions: The Heidelberg Cryogenic Storage Ring CSR", in: *Journal of Physics: Conference Series* **4** (2005), pp. 296–299, DOI: 10.1088/1742-6596/4/1/046.

[23] R. von Hahn, A. Becker, F. Berg, K. Blaum, C. Breitenfeldt, H. Fadil, F. Fellenberger, M. Froese, S. George, J. Göck, M. Grieser, F. Grussie, E. A. Guerin, O. Heber, P. Herwig, J. Karthein, C. Krantz, H. Kreckel, M. Lange, F. Laux, S. Lohmann, S. Menk, C. Meyer, P. M. Mishra, O. Novotný, A. P. O'Connor, D. A. Orlov, M. L. Rappaport, R. Repnow, S. Saurabh, S. Schippers, C. D. Schröter, D. Schwalm, L. Schweikhard, T. Sieber, A. Shornikov, K. Spruck, S. Sunil Kumar, J. Ullrich, X. Urbain, S. Vogel, P. Wilhelm, A. Wolf, and D. Zajfman, "The cryogenic storage ring CSR", in: *Review of Scientific Instruments* **87**. (2016), p. 063115, DOI: 10.1063/1.4953888.

[24] R. D. Thomas, H. T. Schmidt, G. Andler, M. Björkhage, M. Blom, L. Brännholm, E. Bäckström, H. Danared, S. Das, N. Haag, P. Halldén, F. Hellberg, A. I. S. Holm, H. A. B. Johansson, A. Källberg, G. Källersjö, M. Larsson, S. Leontein, L. Liljeby, P. Löfgren, B. Malm, S. Mannervik, M. Masuda, D. Misra, A. Orbán, A. Paál, P. Reinhed, K.-G. Rensfelt, S. Rosén, K. Schmidt, F. Seitz, A. Simonsson, J. Weimer, H. Zettergren, and H. Cederquist, "The double elec-

trostatic ion ring experiment: A unique cryogenic electrostatic storage ring for merged ion-beams studies", in: *Review of Scientific Instruments* **82**. (2011), p. 065112, DOI: `10.1063/1.3602928`.

[25] Y. Nakano, Y. Enomoto, T. Masunaga, S. Menk, P. Bertier, and T. Azuma, "Design and commissioning of the RIKEN cryogenic electrostatic ring (RICE)", in: *Review of Scientific Instruments* **88**. (2017), p. 033110, DOI: `10.1063/1.4978454`.

[26] P. D. W. Demtröder, *Molecular Physics: Theoretical Principles and Experimental Methods*, Wiley, 2007.

[27] M. Born and R. Oppenheimer, "Quantum theory of molecules.", in: *Ann. Phys.* **84**. (1927), p. 0457.

[28] J. von Neuman and E. Wigner, "Uber merkwürdige diskrete Eigenwerte. Uber das Verhalten von Eigenwerten bei adiabatischen Prozessen", in: *Physikalische Zeitschrift* **30** (1929), pp. 467–470.

[29] H. Lefebvre-Brion and R. Field, *Perturbations in the spectra of Diatomic Molecules*, Academic press, 1986.

[30] S. Novotny, H. Rubinstein, H. Buhr, O. Novotný, J. Hoffmann, M. B. Mendes, D. A. Orlov, C. Krantz, M. H. Berg, M. Froese, A. S. Jaroshevich, B. Jordon-Thaden, M. Lange, M. Lestinsky, A. Petrignani, D. Shafir, D. Zajfman, D. Schwalm, and A. Wolf, "Anisotropy and Molecular Rotation in Resonant Low-Energy Dissociative Recombination", in: *Phys. Rev. Lett.* **100** (19 2008), p. 193201, DOI: `10.1103/PhysRevLett.100.193201`.

[31] L. Carata, A. E. Orel, and A. Suzor-Weiner, "Dissociative recombination of He_2^+ molecular ions", in: *Phys. Rev. A* **59** (4 1999), pp. 2804–2812, DOI: `10.1103/PhysRevA.59.2804`.

[32] D. R. Bates, "Dissociative Recombination", in: *Phys. Rev.* **78** (4 1950), pp. 492–493, DOI: `10.1103/PhysRev.78.492`.

[33] J. N. Bardsley, "The theory of dissociative recombination", in: *Journal of Physics B: Atomic and Molecular Physics* **1**. (1968), p. 365.

[34] A. Wolf, H. Buhr, and O. Novotný, "Fast-beam fragmentation experiments on dissociative recombination", in: *Journal of Physics: Conference Series* **300**. (2011), p. 012008.

[35] B. K. Sarpal, J. Tennyson, and L. A. Morgan, "Dissociative recombination without curve crossing: study of HeH +", in: *Journal of Physics B: Atomic, Molecular and Optical Physics* **27**. (1994), p. 5943.

[36] S. L. Guberman, "Dissociative recombination without a curve crossing", in: *Phys. Rev. A* **49** (6 1994), R4277–R4280, DOI: 10.1103/PhysRevA.49.R4277.

[37] C. Strömholm, J. Semaniak, S. Rosén, H. Danared, S. Datz, W. van der Zande, and M. Larsson, "Dissociative recombination and dissociative excitation of ^{4}HeH$^+$: Absolute cross sections and mechanisms", in: *Phys. Rev. A* **54** (4 1996), pp. 3086–3094, DOI: 10.1103/PhysRevA.54.3086.

[38] T. Tanabe, I. Katayama, S. Ono, K. Chida, T. Watanabe, Y. Arakaki, Y. Haruyama, M. Saito, T. Odagiri, K. Hosono, K. Noda, T. Honma, and H. Takagi, "Dissociative recombination of HeH$^+$ isotopes with an ultra-cold electron beam from a superconducting electron cooler in a storage ring", in: *Journal of Physics B: Atomic, Molecular and Optical Physics* **31**. (1998), p. L297.

[39] S. Krohn, "Inelastic collisions and recombination between electrons and molecular ion.", PhD thesis, Ruprecht-Karls-Universität, Heidelberg, 2002.

[40] E. A. Engel, N. Doss, G. J. Harris, and J. Tennyson, "Calculated spectra for HeH+ and its effect on the opacity of cool metal-poor stars", in: *Monthly Notices of the Royal Astronomical Society* **357**. (2005), pp. 471–477, DOI: 10.1111/j.1365-2966.2005.08611.x.

[41] R. Čurík and C. H. Greene, "Inelastic low-energy collisions of electrons with HeH$^+$: Rovibrational excitation and dissociative recombination", in: *The Journal of Chemical Physics* **147**. (2017), p. 054307, DOI: 10.1063/1.4994921.

[42] M. Planck, "Ueber das Gesetz der Energieverteilung im Normalspectrum", in: *Annalen der Physik* **309**. (1901), pp. 553–563, DOI: 10.1002/andp.19013090310.

[43] P.F.Bernath, *Spectra of atoms and molecules*, Oxford University Press, 2005.

[44] Grussie, F., "Experimental studies of ion-neutral reactions under astrophysical conditions.", PhD thesis, Ruprecht-Karls-Universität, Heidelberg, 2016.

[45] Becker, A., "Imaging of Neutral Fragmentation Products from Fast Molecular Ion Beams: Paving the Way for Reaction Studies in Cryogenic Environment.", PhD thesis, Ruprecht-Karls-Universität, Heidelberg, 2016.

[46]   K. Spruck, A. Becker, F. Fellenberger, M. Grieser, R. von Hahn, V. Klinkhamer, O. Novotný, S. Schippers, S. Vogel, A. Wolf, and C. Krantz, "An efficient, movable single-particle detector for use in cryogenic ultra-high vacuum environments", in: *Review of Scientific Instruments* **86**. (2015), p. 023303, DOI: 10.1063/1.4907352.

[47]   C. Krantz, O. Novotný, A. Becker, S. George, M. Grieser, R. von Hahn, C. Meyer, S. Schippers, K. Spruck, S. Vogel, and A. Wolf, "Single-particle detection of products from atomic and molecular reactions in a cryogenic ion storage ring", in: *Nuclear Instruments and Methods in Physics Research Section A: Accelerators, Spectrometers, Detectors and Associated Equipment* **851** (2017), pp. 92–102, DOI: https://doi.org/10.1016/j.nima.2017.01.050.

[48]   Vogel, S., "Developments at an Electrostatic Cryogenic Storage Ring for Electron-Cooled keV Energy Ion Beams.", PhD thesis, Ruprecht-Karls-Universität, Heidelberg, 2016.

[49]   R. von Hahn, V. Andrianarijaona, J. R. Crespo López-Urrutia, H. Fadil, M. Grieser, C. Haberstroh, V. Mallinger, D. A. Orlov, H. Quack, M. Rappaport, C. D. Schröter, D. Schwalm, J. Ullrich, T. Weber, A. Wolf, and D. Zajfman, "Cryogenic Concept for the Low-energy Electrostatic Cryogenic Storage Ring (CSR) at MPI-K in Heidelberg", in: *AIP Conference Proceedings* **823**. (2006), pp. 1187–1193, DOI: 10.1063/1.2202536.

[50]   C. Meyer, A. Becker, K. Blaum, C. Breitenfeldt, S. George, J. Göck, M. Grieser, F. Grussie, E. A. Guerin, R. von Hahn, P. Herwig, C. Krantz, H. Kreckel, J. Lion, S. Lohmann, P. M. Mishra, O. Novotný, A. P. O'Connor, R. Repnow, S. Saurabh, D. Schwalm, L. Schweikhard, K. Spruck, S. Sunil Kumar, S. Vogel, and A. Wolf, "Radiative Rotational Lifetimes and State-Resolved Relative Detachment Cross Sections from Photodetachment Thermometry of Molecular Anions in a Cryogenic Storage Ring", in: *Phys. Rev. Lett.* **119** (2 2017), p. 023202, DOI: 10.1103/PhysRevLett.119.023202.

[51]   A. P. O'Connor, A. Becker, K. Blaum, C. Breitenfeldt, S. George, J. Göck, M. Grieser, F. Grussie, E. A. Guerin, R. von Hahn, U. Hechtfischer, P. Herwig, J. Karthein, C. Krantz, H. Kreckel, S. Lohmann, C. Meyer, P. M. Mishra, O. Novotný, R. Repnow, S. Saurabh, D. Schwalm, K. Spruck, S. Sunil Kumar, S. Vogel, and A. Wolf, "Photodissociation of an Internally Cold Beam of CH^+ Ions in a Cryogenic Storage Ring", in: *Phys. Rev. Lett.* **116** (11 2016), p. 113002, DOI: 10.1103/PhysRevLett.116.113002.

[52] S. van der Meer, "Phase space cooling", in: *Phys. Bl.* **39**. (1983), pp. 117–19.

[53] L. Spitzer, *Physics of Fully Ionized Gases*, 1962.

[54] S. Pastuszka, U. Schramm, M. Grieser, C. Broude, R. Grimm, D. Habs, J. Kenntner, H.-J. Miesner, T. Schüler, D. Schwalm, and A. Wolf, "Electron cooling and recombination experiments with an adiabatically expanded electron beam", in: *Nuclear Instruments and Methods in Physics Research Section A: Accelerators, Spectrometers, Detectors and Associated Equipment* **369**. (1996), pp. 11–22, DOI: https://doi.org/10.1016/0168-9002(95)00786-5.

[55] H. Poth, "Electron cooling: Theory, experiment, application", in: **196** (1990), pp. 135–297, DOI: 10.1016/0370-1573(90)90040-9.

[56] H. Danared, "Fast electron cooling with a magnetically expanded electron beam", in: *Nuclear Instruments and Methods in Physics Research Section A: Accelerators, Spectrometers, Detectors and Associated Equipment* **335**. (1993), pp. 397–401, DOI: https://doi.org/10.1016/0168-9002(93)91223-A.

[57] T. M. O'Neil and P. G. Hjorth, "Collisional dynamics of a strongly magnetized pure electron plasma", in: *The Physics of Fluids* **28**. (1985), pp. 3241–3252, DOI: 10.1063/1.865322.

[58] N. S. Dikansky, V. I. Kudelainen, V. A. Lebedev, I. N. Meshkov, V. V. Parkhomchuk, A. A. Sery, A. N. Skrinsky, and B. N. Sukhina, "Ultimate Possibilities of Electron Cooling", in: (Preprint 88-61 1988).

[59] Shornikov, A., "Operating a low-energy Electron Cooler at the Cryogenic Storage Ring CSR.", PhD thesis, Ruprecht-Karls-Universität, Heidelberg, 2012.

[60] R. A. Phaneuf, C. C. Havener, G. H. Dunn, and A. Müller, "Merged-beams experiments in atomic and molecular physics", in: *Reports on Progress in Physics* **62**. (1999), p. 1143.

[61] G. Kilgus, "Hochauflöosende Messungen zur dielektronischen Rekombination.", PhD thesis, Ruprecht-Karls-Universität, Heidelberg, 1990.

[62] N. J. Manson, K. Burnett, and A. Müller, "New light on electron—ion collisions from heavy–ion storage ring experiments", in: *Philosophical Transactions of the Royal Society of London A: Mathematical, Physical and Engineering Sciences* **357**. (1999), pp. 1279–1296, DOI: 10.1098/rsta.1999.0374.

[63] Cobham CTS Limited, *Opera 16*, 2013.

[64] T. Roberts, *G4beamline User's Guide 2.16*, 2013.

[65] Rimmler, M. M., "Developments at an Electrostatic Cryogenic Storage Ring for Electron-Cooled keV Energy Ion Beams.", MA thesis, Ruprecht-Karls-Universität, Heidelberg, 2017.

[66] Wilhelm, P., "in preparation.", PhD thesis, Ruprecht-Karls-Universität, Heidelberg, 2018.

[67] A. Shornikov, D. A. Orlov, C. Krantz, A. S. Jaroshevich, and A. Wolf, "Maximum intensity, transmission limited cold electron beams from GaAs photocathode in the eV and sub-eV kinetic energy range", in: *Phys. Rev. ST Accel. Beams* **17** (4 2014), p. 042802, DOI: 10.1103/PhysRevSTAB.17.042802.

[68] H. Fadil, D. Orlov, M. Grieser, and A. Wolf, "Design of a Low Energy Electron Cooler for Heidelberg CSR", in: *Proc. EPAC05* **Edinburg, Scotland** (2006), pp. 1630–1632.

[69] F. Hinterberger, *Physik der Teilchenbeschleuniger und Ionenoptik.* Springer Verlag, 2008.

[70] Lohmann, S., "Beam diagnostics and collector for the electron cooler of the cryogenic storage ring CSR", MA thesis, Ruprecht-Karls-Universität, Heidelberg, 2015.

[71] D. D. D. Manura, *SIMION (R) 8.0 User Manual.* Scientific Instrument Services, Inc. Ringoes, NJ 08551.

[72] O. Novotný, A. Becker, H. Buhr, C. Domesle, W. Geppert, M. Grieser, C. Krantz, H. Kreckel, R. Repnow, D. Schwalm, K. Spruck, J. Stützel, B. Yang, A. Wolf, and D. W. Savin, "Dissociative Recombination Measurements of HCl+ Using an Ion Storage Ring", in: *The Astrophysical Journal* **777**. (2013), p. 54.

[73] J. W. Stearns, K. H. Berkner, R. V. Pyle, B. P. Briegleb, and M. L. Warren, "Dissociation Cross Sections for 0.5- to 1-MeV HeH$^+$ Ions in H$_2$, He, N$_2$, and Ne Gases", in: *Phys. Rev. A* **4** (5 1971), pp. 1960–1964, DOI: 10.1103/PhysRevA.4.1960.

[74] D.Paul, "in private communication", in: (2018).

[75] M. Grieser, "in private communication", in: (2018).

[76] O. Novotný, "in private communication", in: (2018).

[77] D. J. Haxton and C. H. Greene, "Ab initio frame-transformation calculations of direct and indirect dissociative recombination rates of HeH$^+$ + e^-", in: *Phys. Rev. A* **79** (2 2009), p. 022701, DOI: 10.1103/PhysRevA.79.022701.

Acknowledgements